Sustainable carbon nanofibres for electrochemical energy storage devices

A thesis submitted to the School of Engineering and Faculty of Science at the University of East Anglia (UEA) in partial fulfilment of the requirements for the degree of Doctor of Philosophy.

Yifan Feng

100272488

March 2024

Abstract

The rapid development of societal economies and technology has escalated the demand for energy, leading to the overconsumption of fossil fuels. Consequently, there is an urgent need for sustainable energy sources and suitable electrochemical energy storage devices. Among these, carbon nanofibres (CNFs) are promising candidates for electrodes in supercapacitors due to their suitable mechanical strength, flexibility, large specific surface area, and the ease of surface chemistry modification. However, majority CNFs are derived from polyacrylonitrile (PAN), a petroleum-based polymer with various drawbacks, such as high cost and environmental concerns.

To address these issues, this study explores the potential of biopolymers as precursors for obtaining CNFs suitable as electrodes in electrochemical energy storage devices, particularly supercapacitors. Biopolymers as cellulose (CELL), polylactic acid (PLA), and chitosan (CTS) were investigated with this purpose, highlighting the studies performed with CTS as its use in previous literature has been very limited.

Therefore, to explore the potential of these biopolymers in the preparation of CNFs, the research methodology involved three main steps. First, biopolymer nanofibres were fabricated using electrospinning, carrying out a systematic investigation of the impact of several experimental parameters including solution rheological properties, concentration, flow rate, and needle size on the fibres morphology and diameter. Then, these nanofibres underwent a stabilisation process to increase their thermal stability, ensuring the maintenance of their fibrous morphology during carbonisation. Finally, the stabilised nanofibres were carbonised to obtain CNFs. Once the CNFs were produced, chemical activation using H_3PO_4 or $ZnCl_2$ as activating agents was performed to improve the physicochemical properties of the nanofibres, making them appropriate for use as electrodes in supercapacitors.

The research's results indicate that CELL, PLA, and CTS nanofibres were successfully fabricated through electrospinning. However, while stabilisation experiments revealed that due

to the low melting point of PLA it could not be successfully stabilised, CELL- and CTS-based CNFs were effectively produced. After the activation step, it was observed that cellulose-based CNFs lacked the mechanical strength required to be set up as self-standing electrodes. Consequently, only activated CTS-based CNFs were utilised as electrodes in supercapacitors. The activation experiments and subsequent electrochemical characterisation showed that despite the decrease in specific surface area after activation, the increased mesopore volume and improved surface chemistry enhanced the electrochemical performance of the activated CNFs. When using H_3PO_4 as activating agent, an impregnation ratio of 1:3 provided the most favourable electrochemical performance, reaching a specific capacitance of 133.67 F/g at 1A/g, retaining 98.5% of its capacitance after 2000 cycles. However, when using $ZnCl_2$, the most effective impregnation ratio was 1:4, resulting in a capacitance of 111.86 F/g, with 97.1% capacitance retention after 2000 cycles. These capacitance values doubled those calculated with non-activated CNFs as electrodes, highlighting the significant enhancement in electrochemical after the activation.

This research contributes to the development of sustainable and cost-effective carbon materials to be used as electrodes in energy storage applications. The results highlight the potential of biopolymer-based CNFs, particularly those derived from chitosan, in meeting the demands for flexible and efficient supercapacitors. The findings underscore the importance of exploring renewable resources and appropriate fabrication technologies for developing electrochemical energy devices, paving the way for further advancements in the field of energy storage.

Acknowledgements

The completion of this research work would have not been possible without the guidance and assistance of many kind people.

Firstly, I wish to express my heartfelt gratitude to my distinguished supervisors, Dr. Sonia Melendi-Espina and Dr. Zoraida González Arias, for their technical guidance throughout my doctoral studies. Their patience and continual support have made a significant contribution to the development of this thesis. I shall also cherish the invaluable advice they provided beyond my research.

Similarly, I extend my thanks to Dr. Andrew Mayes, for his initial guidance on my experiments and for allowing me to conduct preliminary electrospinning experiments in his laboratory.

Moreover, my sincere appreciation goes to Dr. Masoomeh Bazzar. Without her patient assistance and guidance, I would not have been able to successfully spin controllable nanofibres.

I am also immensely grateful to Daniel Barreda García for his vital support. His patient guidance in electrochemical testing and characterisation has been invaluable.

Lastly, my gratitude extends to my parents. Despite their physical absence, their encouragement and unconditional support have been my driving force to persevere.

List of publications and international conference presentations

Under review or preparation journal papers:

1. **Y. Feng**, M. Bazzar, M. Hernaez, D. Barreda, A. G. Mayes, Z. González, and S. Melendi-Espina, "Unveiling the potential of cellulose, chitosan and polylactic acid as precursors for the production of green carbon nanofibers with controlled morphology and diameter" *International Journal of Biological Macromolecules* 269 (2024): 132152.

International conference presentations

1. The World Conference on Carbon, "Preparation and optimisation of environmentally friendly electrospun nanofibers" Poster Presentation, London, United Kingdom, 2022

2. The World Conference on Carbon, "Electrospun carbon nanofibres from plant-based precursors as active electrode materials for electrochemical energy storage devices" Poster Presentation, London, United Kingdom, 2022

List of abbreviations

ACNFs	Activated carbon nanofibres
ACs	Activated carbons
BD	Billion dollars
CAGR	Compound annual growth rate
CNFs	Carbon nanofibres
CNTs	Carbon nanotubes
CTS	Chitosan
CV	Cyclic voltammetry
CVD	Chemical vapor deposition
DSC	Differential scanning calorimetry
EDL	Electrical double layer
EDLCs	Electrical double-layer capacitors
ESR	Equivalent series resistance
EVs	Electric vehicles
FESEM	Field emission scanning electron microscopy
FT-IR	Fourier-transform infrared spectroscopy
GCPL	Galvanostatic cycling with potential limitation
GO	Graphene oxide
IEA	International energy agency

LABs	Lead-acid batteries
LIBs	Lithium-ion batteries
MT	Million tons
MWCNTs	Multi-walled carbon nanotubes
Mtoe	Million tons of oil equivalent
Ni-Cd	Nickel-cadmium
Ni-MH	Nickel-metal hydride
OLED	Organic light-emitting diode
PAHs	Polycyclic aromatic hydrocarbons
PAN	Polyacrylonitrile
PHES	Pumped hydroelectric energy storage
PLA	Poly(lactic acid)
PVA	Polyvinyl alcohol
PVP	Polyvinylpyrrolidone
RFB	Redox flow batteries
RFID	Radio frequency identification
SCs	Supercapacitors
SDGs	Sustainable development goals
SIBs	Sodium-ion batteries
SKL	Sulphate kraft lignin

SWCNTs	Single-walled carbon nanotubes
TGA	Thermogravimetric analysis
TJ	Terajoule (equal to 10^12 joules)
TW	Terawatt (equal to 10^12 watts)
VRFBs	Vanadium redox flow batteries
XPS	X-ray photoelectron spectroscopy
rGO	Reduced graphene oxide

Table of Contents

List of Figures

List of Tables

Chapter 1

Introduction

1. Introduction

1.1 Background and motivation

Over the past 200 years, the remarkable development of human civilisation and economy has been inseparable from the intensive use of energy. Due to human activities such as transportation, education, urbanisation, and industrialisation, energy consumption has steadily increased. According to data from the International Energy Agency (IEA), the global total energy consumption was approximately 16,740 million tons of oil equivalent (Mtoe) in 2019 [1], fossil fuels (including oil, natural gas, and coal) accounting for about 81% of that. This means that approximately three-quarters of the energy demand is met through the burning of fossil fuels. The excessive use of these fuels not only leads to their severe depletion and consequent scarcity but also contributes to many other serious problems, such as environmental pollution and climate change. In addition, energy demand is also affected by geopolitical and economic factors. Some countries or regions have abundant energy resources, while others need to import energy from other countries. These facts lead to fluctuations in the energy market and changes in prices, and also triggers some international energy disputes and conflicts. Therefore, to ensure the safe supply of energy and contribute to the sustainable development of our society, many countries are actively promoting energy diversification and decarbonisation of the energy model, in order to reduce reliance on traditional fossil fuels, improve energy utilization, and, mainly, promote the introduction of renewable energy sources into the energy mix. According to the IEA, future demand for energy will continue to grow. By 2040, global energy demand will increase by 25%, with most of the growth coming from Africa and Asia [2]. At the same time, the share of renewable energy will continue to increase, and by 2040 it will account for more than 40% of global power supply [2]. Moreover, the electronic revolution, with the widespread use of different portable devices such as smartphones, laptops, and tablets, contributes to such increased demand for energy. Consequently, the use of renewable energy sources in contemporary society must consider both **large-scale energy storage** in industrial

settings and households and **medium-scale storage** for EVs. In addition, the design and development of advanced solutions for **small-scale energy storage** need to be addresses for pushing the market and performance of portable devices (Figure 1.1). Traditional energy storage systems, such as Pumped Hydroelectric Energy Storage (PHES), have been widely used to meet large-scale energy storage needs. These systems rely on pumping water to higher elevations during periods of low energy demand and releasing it to generate electricity during peak loads. While PHES is a mature and effective technology for energy management, its deployment is highly constrained by geographical requirements, limiting its adaptability and scalability in many regions [3]. Additionally, other traditional systems, like compressed air energy storage, also face challenges in terms of efficiency and infrastructure requirements. In contrast, electrochemical energy storage devices offer a more versatile and scalable solution for addressing the growing energy storage demands across various applications. These devices, including batteries and supercapacitors, are not only suitable for large-scale integration with renewable energy sources but are also highly adaptable for medium- and small-scale applications, such as EVs and portable devices. Their advantages include higher energy density, greater flexibility in deployment, and the ability to integrate with intermittent energy sources like solar and wind power. These characteristics make electrochemical systems more suitable for contemporary energy storage needs, overcoming many limitations of traditional storage methods. However, energy storage at all these scales still faces some challenges.

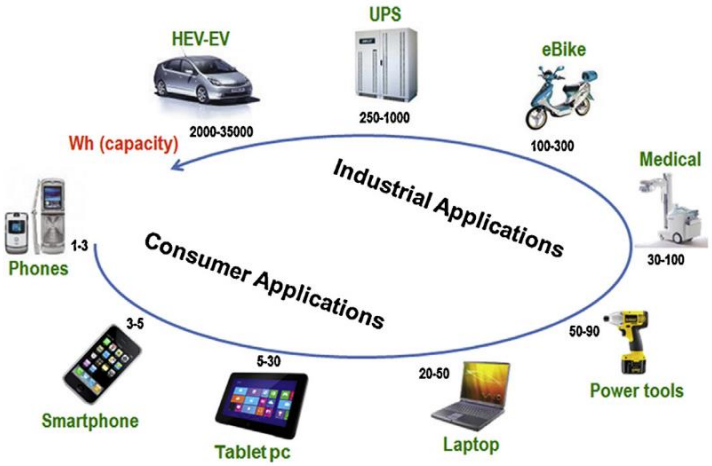

Figure 1.1. Application of energy in modern society [4]

For **large-scale energy storage**, modern electrochemistry faces significant challenges in developing devices suitable for storing large amounts of electricity and supplying it to the grid during peak demand periods. These storage systems must be safe and fabricated from cheap, widely available and sustainable materials, despite their potentially considerable size. Unlike applications in electric vehicles or portable devices, high specific energy density is not a requirement for stationary storage. However, the key point for these systems is to demonstrate an appropriate stability and a long term performance [5], [6]. For this purpose, different electrochemical energy storage devices have been previously reported in the literature, including various secondary batteries, such as lead-acid batteries (LABs), lithium-ion batteries (LIBs), and redox flow batteries (RFBs). Most of these technologies are relatively mature and have become the focus of attention in recent years, being commonly applied in large-scale applications. For instance, LABs are widely used due to their simple structure, low cost, and ease of maintenance. They are characterised for their long cycle life, approximately 1000 cycles, with efficiency values ranging between 80 - 90%. However, their energy density, within the range of 60-75 Wh/L, is significantly lower than that of LIBs [7]. Furthermore, when LABs are discharged at high power, their available capacity diminishes, leading to a significant reduction in energy density [3]. Consequently, LABs are typically employed as emergency or backup power sources within large-scale energy storage systems. LIBs appeared as potential candidates

to replace LABs, providing many advantages: (i) their efficiency can be higher than 95 %; (ii) their discharge time can reach several hours; (iii) the number of charge/discharge cycles can be more than 5000; and (iv) their response is fast [8]. Moreover, LIBs are currently the most practical high-energy-density batteries available. These energy density values vary significantly, ranging from 100 to 250 Wh/L, depending on the active electrode materials used [7], as in these batteries energy is stored within the electrodes. Hence, a primary drawback of LIBs is the degradation that the electrodes experience due to the successive charge and discharge cycles [9]. LIBs feature a variety of materials for their anodes and cathodes, including lithium cobalt oxide, lithium manganese oxide, lithium iron phosphate, and lithium titanate-based batteries, etc [10]. Despite a decrease in their prices in recent years, attributed to large-scale production, the cost of LIBs remains relatively high. Additionally, safety concerns occasionally arise with LIBs due to the potential for heat generation and combustion if overcharged, necessitating the implementation of protection mechanisms. That is why the technology of LIBs is still being under investigation. Current research is focused on the improvement of their cyclability and safety, reducing costs, and developing new materials for the positive and negative electrodes [51, 53].

In this context, redox flow batteries (RFBs) emerge as promising devices, avoiding some of the drawbacks previously mentioned. Unlike LIBs and other secondary batteries, the electrodes in RFBs do not act as energy storage elements. Instead, they provide the active sites for the development of the redox reactions of the electroactive species dissolved in the electrolyte [11]. The ability to store a substantial volume of electrolyte in separate tanks outside the battery stack, which is then pumped into the cell for reaction via peristaltic pumps, allows for their flexible configuration in terms of power (number and size of stacks) and energy density (volume and concentration of the electrolyte). This scalability significantly enhances their suitability for large-scale energy storage applications. In this regard, vanadium redox flow batteries (VRFBs) and Zinc-Bromine (Zn/Br) flow batteries stand out as two examples widely utilised in large-scale energy storage. VRFBs are mainly characterised by their superior long-term performance,

avoiding cross-contamination issues, a notable advantage even though their energy and power density values fall below those of other batteries. Remarkably, VRFBs can achieve more than 10,000 charge-discharge cycles [12]. In contrast, Zn/Br flow batteries offer higher energy density, lower costs, and other benefits over VRFBs. However, they face a significant challenge of severe self-discharge, as a consequence of the formation of complex compounds during battery operation [3].

When assessing challenges on **medium-scale energy storage**, electrical propulsion issues arise. Currently, the majority of vehicles are powered by internal combustion engines that use fossil fuels as their energy source. However, this type of vehicles has encountered various problems, such as the production of pollution and noise, CO_2 emissions (contributing to global warming), and the shortage of petroleum resources. As a result, the development of new electric vehicles (EVs) remains a strategic issue for nations worldwide. However, in the broader context of mitigating global warming, the progress in the development of EVs is still unsatisfactory. At present, to reduce the automotive industry's reliance on oil, several strategies have been proposed. Among these, hydrogen-based fuel cells are considered a viable solution for electrochemical propulsion in EVs [13]. However, this application faces a significant challenge due to the high cost of platinum-based electro-catalysts required for both hydrogen and oxygen reactions [14]. Solar batteries emerge as another alternative to traditional internal combustion engines. Solar energy, being clean and relatively easy to produce, suffers from limitations such as regionality, seasonality, and time-domain characteristics, which hamper its long-term application. Additionally, solar batteries are hindered by their low energy density, low conversion efficiency, and high cost [15]. These factors limit their use in traditional vehicles, being commonly applied in solar racing cars and short-distance electric cars. In this context, powering EVs through rechargeable batteries appears to be the most practical strategy. Nonetheless, rechargeable batteries still face several unresolved issues. A primary limitation concerns the size of the battery as EVs are required to have comparable dimensions, weight, and space to conventional vehicles powered by internal combustion engines. The weight and

volume of the battery should ideally be less than 300 kg and 200 litres, respectively [16]. Currently, LIBs stand as the most practical power source for EVs. However, even the most advanced LIBs still need further improvement to fully meet the future demands of the EV market, due to their low energy density and high cost [17]. Moreover, the safety and fast-charging capabilities of LIBs still require enhancements for broader market acceptance. Supercapacitors (SCs) have also been explored for use in EVs applications. There are three main approaches to incorporate SCs into EVs: using them as the only power source in pure electric buses, combining SCs with batteries in pure electric vehicles, and using SCs alongside other fuels in hybrid vehicles [18], [19]. Recent research and development have identified two key challenges for SCs: increase their energy density and the issue of voltage equalization. Voltage equalization is a critical challenge when supercapacitors are connected in series, as inherent differences in capacitance and leakage current can lead to uneven voltage distribution. Without intervention, some supercapacitors may become overcharged or over-discharged, which can damage the system or shorten its lifespan. Voltage equalization circuits are therefore essential to ensure balanced voltage across all units during operation. Voltage equalization presents a significant challenge when supercapacitors are connected in series, as inherent variations in capacitance and leakage current can lead to uneven voltage distribution. This imbalance may result in some supercapacitors becoming overcharged or over-discharged, potentially damaging the system or reducing its lifespan [20]. Although voltage equalization circuits have been proposed to address this issue, it remains a challenge in the context of EV applications, requiring further technological optimisation and research.

Finally, regarding the **small-scale energy storage** related to portable devices, the growing demand for electronic systems in modern society has positioned mobile power sources and portable/wearable devices as key elements in addressing technological innovation. In this context, the development of flexible electronic devices has garnered significant attention. These devices are characterised by their suitability to operate continuously under various forms of deformation, such as bending, folding, twisting, compressing, or stretching. This category

encompasses flexible display screens, wearable sensors, and implantable medical devices (Figure 1.2). In most applications, such devices necessitate the integration of flexible energy storage systems for power supply, which are required to withstand certain degrees of deformation due to external forces, without compromising their fundamental structure and power supply functionality. However, the majority of batteries/capacitors currently manufactured in the industry are rigid and lack the capability to function under previously mentioned operational conditions.

Figure 1.2. Overview of several potential applications of flexible devices [21]

Particularly, the performance of many electronic devices is constrained by the battery used for their operation. For example, the battery of a smartphone nearly constitutes one-third of its volume and weight, leading to frequent user complaints about insufficient battery life. Hence, in the development of flexible electronic devices, the corresponding flexible battery technology must also advance. Additionally, traditional energy storage devices, such as secondary batteries/capacitors, cannot be directly applied in flexible applications for several reasons [22], [23]: (1) Most materials used in traditional batteries/capacitors lack flexibility; (2) The contact degree among various constituent materials is relatively low; (3) Deformation may cause extremely irreversible microstructural changes, device performance degradation, and even

device failure during use; (4) There is a low loading of active substances; (5) There exists a risk of leakage of the liquid electrolyte; (6) Packaging materials and the working environment have rigid limitations. Therefore, to overcome these drawbacks, the manufacturing technology for flexible devices must continue to innovate in the areas of flexible electrodes, new electrolytes, and new manufacturing and packaging technologies.

As previously stated, the most extensively utilized electrochemical energy storage devices are batteries and supercapacitors (SCs). The energy storage mechanism of batteries is associated with the redox reactions (faradaic processes) of electroactive species occurring at the two electrodes (anode and cathode) that constitute the battery. Various types of batteries, such as lead-acid batteries (LABs), nickel-cadmium (Ni-Cd) batteries, nickel-metal hydride (Ni-MH) batteries, and lithium-ion batteries (LIBs), characterized by distinct energy/power density values, have been commercialized. The application of LABs is restricted due to issues related to electrolyte corrosion and excessive weight, which has limited their broader development [24]. Similarly, Ni-Cd and Ni-MH batteries exhibit low operational voltages and suffer from a significant memory effect, rendering them unsuitable for various applications [25], [26]. However, LIBs, with their smaller sizes, lighter weights, higher energy density values, and adaptability, are deemed more suitable for use in a wide range of electronic devices compared to other battery types [27]. In contrast to batteries, SCs store energy via the formation of an electrical double layer (EDL), achieved by the migration of charged ions across the electrode-electrolyte interface under an applied electric field, offering rapid charging and discharging capabilities. Despite having lower energy density values than batteries (Figure 1.3), SCs have garnered substantial attention due to their low cost, long cycling life, safety, and high power density [28]–[30]. With the development of materials that exhibit high pseudocapacitance and the advent of hybrid SCs, the energy density of SCs has significantly improved, now surpassing that of LIBs [31].

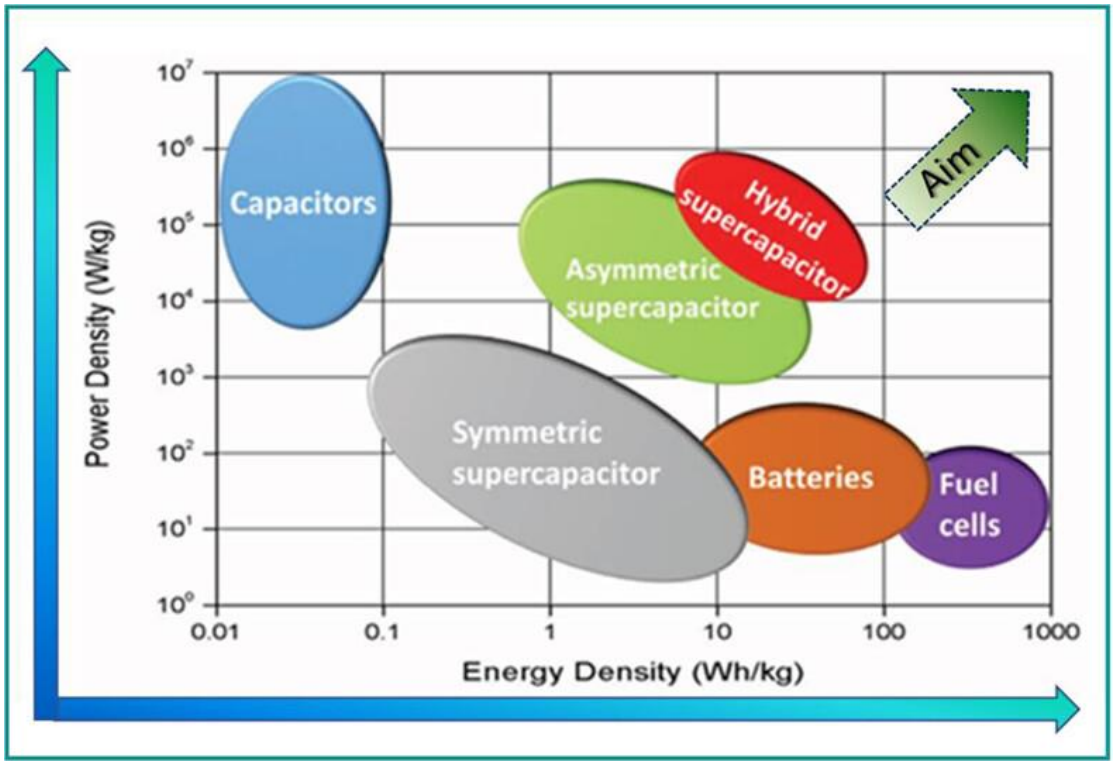

Figure 1.3. Schematic representation of different electrochemical energy storage devices in terms of power and energy density values (Ragone plot) [32]

Between the wide variety of available active materials, carbon-based materials, including carbon nanofibres (CNFs), carbon nanotubes (CNTs), activated carbons (ACs), and graphene, are extensively employed as electrode materials in batteries and SCs due to their abundance, ease of acquisition, non-toxic nature, high specific surface area, appropriate electrical conductivity, high chemical stability, and broad operational temperature range [25]. Despite these advantageous characteristics, there remain issues that need addressing, primarily concerning electrochemical activity, which significantly impacts their respective electrochemical behaviours, including energy and power density values and long-term performance. Current research on carbon materials for electrochemical energy storage applications primarily focuses on the optimisation of several properties, such as multi-pore structure, morphology control, and surface functionalisation. This focus aims to enhance the electrochemical performance and applicability of these materials in energy storage technologies.

Among the available materials, nanostructured carbon materials such as CNFs and CNTs have gained significant attention due to their exceptional properties. While CNTs are considered true one-dimensional (1D) materials owing to their nanoscale diameter and high aspect ratio, CNFs are better classified as quasi-one-dimensional structures [33] due to their larger diameters and continuous fibrous morphology. Despite these dimensional differences, both CNFs and CNTs exhibit remarkable characteristics such as high conductivity, mechanical strength, and adaptability for various applications [34]. CNFs, with their extraordinary length, flexibility, and efficient electron transport capability, are highly versatile in creating unique architectures. They can be modified with pores, functional groups, and other active materials to address specific challenges in supercapacitors design development [35]–[37]. These properties make CNFs a promising candidate for overcoming current challenges in the development of flexible supercapacitor with improved energy densities.

The cost, final properties, and subsequent electrochemical performance of CNFs are influenced by the choice of precursors and the manufacturing process. Currently, the market is predominantly occupied by polyacrylonitrile (PAN) [38]. Despite being a technology that has been in use for over 40 years, the production of CNFs from PAN continues to present several challenges [39]. For instance, PAN contains polar nitrile groups, which impede the alignment of molecular chains during the spinning process. As a result, PAN is often mixed with other monomers, such as acrylic acid, methacrylic acid, and methacrylate, during fibre spinning. However, the introduction of these monomers significantly affects the carbonisation process [40]. Additionally, the cost of PAN is subject to fluctuations in crude oil prices [38], which ultimately affects the final cost of CNFs. Coal-derived pitches, including isotropic and mesophase pitches, are other commonly used precursors. In theory, pitch-based CNFs exhibit higher stiffness values than PAN-based CNFs, with a higher Young's modulus, and better electrical and thermal properties [41]. However, due to the diversity in types of raw coal and processing technologies, the composition of pitch compounds is very complex, leading to structural variability such as the inclusion of surface defects, internal voids, and contaminants,

which can impact the performance of the final pitch-based carbon material [38]. To address these drawbacks, biopolymer-based precursors are receiving significant attention due to their cost-effectiveness, sustainability, and eco-friendliness. For example, Cai et al. used cellulose as precursor for the preparation of nitrogen-doped CNFs to be used as high-performance supercapacitor electrode materials [42]. In addition to cellulose, lignin is also used as raw material for the fabrication of carbon fibres. For example, Wang et al. used lignin/poly (ethylene oxide) blends as raw materials to prepare a nitrogen-doped and independently molten carbon fibre felt by electrospinning, which was then carbonised and annealed in the presence of urea. They also studied the electrochemical performance of the carbon fibre as the anode of LIBs [43].

The fabrication of nanofibres involves various methodologies, including both top-down and bottom-up approaches. Top-down methods typically use physical processes, such as grinding, ball milling, or cryo-crushing, to break down bulk materials into nanoscale fibres [44]. However, these methods often result in nanofibres with lower aspect ratios and compromised mechanical stability [45]. On the other hand, bottom-up approaches, including techniques such as electrospinning, drawing, and phase separation, involve the assembly of nanofibres from smaller units like molecules, ions, or nanoparticles [44]. Among these methods, electrospinning has gained significant attention due to its ability to produce ultra-fine fibres with diameters at the nanoscale, typically in the range of hundreds to tens of nanometres. Compared to traditional spinning techniques such as melt spinning, wet spinning, and dry spinning, electrospinning offers distinct advantages. For instance, melt spinning, which is widely used in the production of polymer fibres, can only achieve fibre diameters down to approximately 10 microns [46]. In contrast, electrospinning utilises a high-voltage electric field to draw charged polymer solutions or melts into nanoscale fibres. This makes electrospinning particularly suitable for applications requiring ultra-fine fibre structures. Moreover, electrospinning allows precise control over key parameters such as polymer solution concentration, applied voltage, spinning distance (needle to collector), solvent volatility, and flow rate [47], enabling researchers to tailor the diameter,

morphology, composition, and orientation of the nanofibres [48]–[50]. Additionally, advancements in electrospinning techniques, such as coaxial electrospinning, have enabled the fabrication of complex fibre structures, including core-sheath and hollow nanofibres [51]. The cost-effectiveness of electrospinning, combined with its versatility and precision, makes it a highly practical method for nanofibre production. Electrospun nanofibres find applications across a wide range of fields, including filtration, biomedicine, energy storage, thermal insulation, and aerospace [52].

In summary, the rapid development of the modern society's economy and technologies has led to an increased demand for energy, resulting in the excessive consumption of fossil fuels. Consequently, there is an urgent need for sustainable energy sources and suitable electrochemical energy storage devices. Beyond large and medium-scale energy storage, the vast development of portable devices has heightened interest in small-scale energy storage systems, such as SCs and hybrid systems, which offer the required energy and power density values among other characteristics. Specifically, the emergence of flexible and wearable electronics has further influenced the requirements for these future energy storage devices. Several carbon materials have garnered extensive attention as excellent candidates for electrodes in these electrochemical energy storage devices, with CNFs and ACNFs standing out due to their superior properties, including high mechanical strength, flexibility, large specific surface area, high aspect ratio and enriched surface chemistry. However, their commercialisation is significantly influenced by the choice of precursor, the preparation process, and ultimately, the cost. As mentioned earlier, biopolymeric materials, such as cellulose, are regarded as favourable carbon precursors due to considerations of environmental protection, sustainability, and cost. Regarding the preparation process, electrospinning emerges as a promising technology because of its low setup cost, commercialisation potential, and its capability to control diameters, morphology, and composition of nanofibres. With this in mind, this thesis aims to fabricate CNFs/ACNFs from bio-based materials through electrospinning

and stabilisation/carbonisation/activation procedures. The as obtained materials are then evaluated as potential electrodes in SCs rendering appropriate electrochemical performance.

1.2 Research aim and objectives

As previously mentioned, the research on using biopolymers as precursors to prepare CNFs/ACNFs is currently limited. This thesis aims to evaluate the suitability of different biopolymers as precursors to synthesize these materials for their subsequent application as active electrode materials in SCs. In this regard, the diameter, morphology, surface chemistry, and other characteristics of CNFs/ACNFs can significantly influence their electrochemical performance in such electrochemical energy storage devices. Furthermore, various experimental parameters and operating conditions of the process of their preparation will affect their final properties. Therefore, optimisation is required at every stage, from the preparation of precursor nanofibers to the final application of the resulting CNFs and ACNFs in SCs.

Regarding the preparation of precursors, the biopolymers selected for this study are cellulose, polylactic acid, and chitosan, based on their unique properties and potential in electrochemical applications. While cellulose and polylactic acid have been previously used for this purpose [38], [42], [53], [54], chitosan, in particular, stands out for its innovative use as a precursor, offering distinctive properties such as biocompatibility, abundant functional groups, and excellent mechanical strength, which can significantly enhance the electrochemical performance of the resulting CNFs/ACNFs in supercapacitors. This innovation is essential for addressing the current challenges in the development of supercapacitors, making the use of chitosan a focal point of this research.

In this context, to achieve the goal of using biopolymers as precursors to produce high-performance CNFs/ACNFs for their subsequent application as electrodes in SCs, this thesis sets the following objectives:

a. Preparation of precursor nanofibres with controlled morphology and diameter

Electrospinning is a simple and effective technique that allows precise control of the morphology and size of nanofibres by adjusting the composition and rheological properties of the precursor solution and different parameters of the electrospinning process. Therefore, the first objective of this research is to use this technology to prepare biopolymer derived nanofibres with suitable characteristics. To achieve this goal, extensive investigations are conducted on selected biopolymer solutions to determine suitable polymer concentrations and solvents, thus ensuring solution with appropriate rheological characteristics. Subsequently, key experimental parameters (e.g., solution concentration, flow rate, and needle size) are systematically optimised to control the morphology and size of the resulting nanofibres. Furthermore, advanced characterisation techniques, including scanning electron microscopy (SEM), were employed to analyse the morphology and diameter of the produced nanofibres. By accomplishing the previously described steps, a solid foundation is established for the subsequent production of high-performance CNFs, particularly those from CTS as novel precursor. Additionally, by acquiring a deep understanding of the correlation between the properties of the selected precursors and electrospinning parameters, valuable insights are provided for research in the field of suitable nanofibres fabrication.

b. Stabilisation of precursor nanofibres

The second part of this research aims to study the stabilisation of precursor nanofibres for their further treatments leading to CNFs. In this regard, the goal is to select appropriate stabilisation conditions (such as stabilisation temperature and duration) able to maintain the morphology of the precursor fibres, ensuring that they do not undergo severe deformations or lose their fibrillary structure in the subsequent high-temperature carbonisation step.

c. Carbonisation of stabilised nanofibers for obtaining CNFs

During carbonisation of previously stabilised nanofibres, non-carbon elements are gradually removed, resulting in the formation of nanoscaled carbon fibre structures with suitable carbon content. The main aim of this objective is to analyse the impact of different carbonisation

parameters on the properties of resulting carbon nanofibres (such as morphology, specific surface area, and surface chemistry).

Throughout the stabilisation and carbonisation steps, different characterisation techniques such as scanning electron microscopy (SEM), Fourier-transform infrared spectroscopy (FT-IR), thermogravimetric analysis (TGA), and differential scanning calorimetry (DSC) are used to analyse the morphology, thermal properties and chemical composition of the resulting nanofibres. The obtained results contribute to understand the fibre evolution mechanisms during both stages and to ensure the appropriate morphology and diameter standards.

d. CNFs activation

Activation, a crucial step for improving CNFs performance as electrodes in SCs, primarily aims to develop texture within their structure. The increase in porosity is key to facilitate the physical adsorption of ions, which is essential for the formation of the electrical double layer. Additionally, activation introduces surface functional groups and heteroatoms, further enriching the electrode's electrochemical performance. Activation step can be performed by following either physical or chemical methods, each one contributing uniquely to the enhanced performance of the carbon nanofibers in supercapacitors. Among the various possibilities for CNFs activation, the chemical route has been selected in this thesis for its specific advantages. Hence, the primary goal is to select suitable activating agents and optimise key experimental conditions to ensure the success of the activation step in order to obtain suitable ACNFs for the selected application.

A detailed characterisation of the ACNFs is performed, being the results obtained compared to that corresponding to the previously prepared CNFs. Thus, changes in fibres morphology are observed by SEM. The surface chemistry is determined by XPS. Additionally, the specific surface area is calculated from the N_2 isotherm after applying the Brunauer-Emmett-Teller (BET) methodology. All these data contribute to correlate the activation method selected with

the characteristics of the ACNFs obtained, aiming to improve their electrochemical performance as electrodes in SCs.

e. Testing the electrochemical performance of CNFs and ACNFs as electrodes in SCs

The electrochemical characterisation of synthesized CNFs and ACNFs as electrodes in aqueous SCs is performed by means of cyclic voltammetry (CV) measurements and galvanostatic cycling with potential limitation (GCPL) tests. For comparative purposes, CNFs are also evaluated. A correlation between the physicochemical properties of the different active electrode materials under evaluation and their subsequent electrochemical performance is also established. Notably, the ACNFs derived from CTS exhibit superior electrochemical performance in terms of specific capacitance, demonstrating the potential of this biopolymer as a novel and sustainable precursor for high-performance electrode materials in supercapacitors.

1.3 Thesis structure

The thesis consists of eight main chapters, which provide a detailed description of the production process of carbon nanofibres, the development of related techniques following the experimental sequence, and their application in electrochemical energy storage devices.

Chapter 1 provides an overview of the thesis's motivation and background, explaining the rationale behind selecting biopolymers as carbon precursors for carbon nanofibers and outlining the primary objectives of the study.

Chapter 2 presents a comprehensive review of the existing literature on the use of carbon nanofibers in electrochemical energy storage devices. The chapter discusses the limitations of previous studies and identifies gaps in the literature that the current research aims to address. Additionally, this chapter introduces relevant theoretical foundations and concepts necessary for understanding the experimental work presented in the following chapters.

Chapter 3 outlines the experimental methods employed throughout the study. This chapter provides a detailed description of the fabrication processes, including electrospinning,

stabilisation, carbonisation, and activation. It also covers the characterisation techniques used to evaluate the physicochemical and electrochemical properties of the carbon nanofibres and activated carbon nanofibres.

Chapter 4 provides a detailed exposition of the fabrication process of carbon nanofibre precursors through electrospinning. It covers the optimisation of various electrospinning parameters, such as solution concentration, voltage, and flow rate, to achieve desired fibre properties. The resulting fibres are thoroughly characterised using various techniques to ensure their suitability for subsequent stages.

Chapter 5 focuses on the stabilisation of precursor fibres, emphasising the optimisation of parameters such as temperature and duration. This chapter aims to enhance the carbon yield and ensure the structural integrity of the carbon nanofibres, carefully selecting optimal conditions for the successful transformation of precursor fibres into carbon nanofibres.

Chapter 6 combines the discussion on carbonisation and activation processes for carbon nanofibres. It explores the carbonisation process to improve the properties of carbon nanofibres and examines various activation agents and conditions to modify the surface chemistry and porosity of the carbon nanofibres. This chapter details the experimental procedures and optimisation steps necessary to achieve the desired properties of activated carbon nanofibres.

Chapter 7 presents the performance evaluation of different carbon nanofibres concerning their electrochemical properties. It analyses their performance as electrode materials in supercapacitor. The chapter discusses key findings and highlights the most promising carbon nanofibre compositions for practical applications.

In the final chapter, Chapter 8, the thesis offers a comprehensive summary of the entire study, discussing the main findings and their implications. It also suggests future research directions and areas that could benefit from further investigation. This chapter provides a conclusive wrap-up and serves as a guide for researchers interested in extending the research in this field.

Chapter 2

Literature review

2. Literature review

2.1 Fundamentals of electrochemical energy storage devices

As previously stated, electrochemical devices have experienced significant advancements in the last decades, appearing as indispensable energy storage systems in various sectors of modern society. Their development began in the early 19th century, with the exploration of electrochemical reactions, when it was discovered that electrical energy could be stored into chemical substances. As technology advanced, these devices found widespread applications and became integral to contemporary society. From their energy storage mechanisms, electrochemical energy storage devices can be classified into batteries (including primary or single use and secondary or rechargeable batteries), SCs, and hybrid systems.

2.1.1 Batteries

Primary batteries, such as carbon-zinc batteries or alkaline batteries, are characterised by the conversion of their internal chemical reactions into electrical energy, being this energy conversion irreversible. If recharging is attempted, these batteries may eventually explode due to the conversion of the injected charge into heat [55].

A **secondary or rechargeable battery** is a device able to convert chemical energy into electrical energy, and vice versa, through the development of the reversible redox reactions (faradaic processes) related to the electroactive species present. A battery is mainly composed of two electrodes (anode and cathode) which act as supports of the faradaic processes related to the charge/discharge of the whole device, an electrolyte where the electroactive species are dissolved, and a separator/membrane (Figure 2.1). The anode (where the oxidation reaction takes place) is the negative terminal of the whole cell and serves as an electron source. The cathode (where the reduction reaction is developed) acts as a positive terminal, and the electrolyte acts as a shared medium that enables the movement of ions between the cathode and anode thus ensuring the electroneutrality. The main function of the membrane is to separate the

two half-cells of the battery to prevent short-circuiting of the two poles. In addition, it must have the function of allowing electrolyte ions to pass through. Initially, the redox process causes negative charges to accumulate on the anode, making its potential become negative. Since the entire battery system needs remain neutral, the corresponding positive charge will accumulate in the surrounding electrolyte medium, which will create an electric field between the electrolyte and the anode opposite to the redox process. A similar mechanism occurs on the cathode, where positive charges accumulate, causing its potential to become positive. Under the condition of open-circuit, the potential between the cathode and the anode reaches the equilibrium, being the potential difference the open-circuit voltage of the battery. When discharging (Figure 2.1 (a)), the previous equilibrium state of the battery will be disturbed by the flow of charge through the external load. The redox reactions of the battery continuously replenish the charge consumed by the external load until a new equilibrium state is reached.

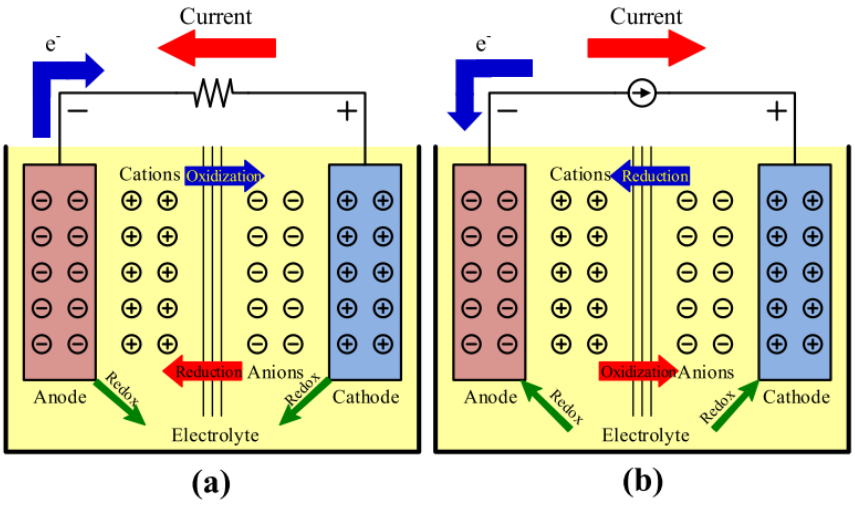

Figure 2.1. A battery single cell under (a) discharging, and (b) charging conditions [55]

The active electrode material used significantly impacts on a battery's capacity, lifespan, safety, and other attributes. A key criterion for selecting suitable active materials for being used as electrodes in batteries is that they have to provide enough specific surface area, an appropriate porous structure or active sites. These characteristics facilitate the insertion of more ions into the electrode or the appropriate development of faradaic reaction, which in turn enhances the

battery's capacity. For example, regarding lithium-ion batteries (LIBs), the high lithium content and the reversible intercalation of lithium ions into the electrode materials allow them to achieve their characteristic high capacity values [56]. Additionally, electrodes with a high lithium-ion diffusion coefficient are crucial to decreasing internal resistance and enhancing the power density of LIBs [57]. Furthermore, the electrode material should exhibit good electrolyte compatibility and thermal stability, not only for reaching and improved cycle life but also for safety considerations. Nowadays, the three primary cathode materials for LIBs are lithium manganate ($LiMn_2O_4$), lithium iron phosphate ($LiFePO_4$), and ternary lithium. $LiMn_2O_4$, in particular, is widely used owing to its superior safety characteristics, robust overcharge resistance, and affordability [58]. However, it also exhibit significant drawbacks, mainly associated to the lack of high temperature resistance, so it is not generally used in high power or high ambient temperature conditions [59]. $LiFePO_4$ batteries are distinguished by their exceptional safety and long cycle life, both properties being directly linked to their olivine structure. This specific structure accounts for the lower lithium-ion diffusion coefficient in $LiFePO_4$, contributing to its enhanced high-temperature stability and cycle performance. However, due to its chemical structure, a $LiFePO_4$ macromolecule is capable of accommodating only a single lithium ion, resulting in a lower energy density [8]. Ternary lithium batteries, on the other hand, refer to LIBs that utilise lithium intercalation transition metal oxides containing nickel, cobalt, and manganese as the cathode material. This composition merges the benefits of lithium cobalt oxide, lithium nickel oxide, and lithium manganate, ensuring a synergistic effect within the same battery cell. This synergy addresses the three critical aspects of material structure stability, reactivity, and cost-efficiency. Among the three primary cathode materials, it has the highest energy density. However, the safety of ternary lithium batteries is compromised due to their inferior thermal stability, highlighting a significant drawback in comparison to other battery technologies [60], [61].

Graphite is the most widely used anode material for LIBs due to its low electric potential and its layered stacking structure, which allows lithium ions to insert freely between layers with

less obstruction. Nonetheless, when used in electric vehicles, graphite anodes pose safety risks due to metallic Li deposition and have a limited theoretical capacity of 372 mA h/g [62]. Alternative carbon materials, such as carbon nanotubes (CNTs), graphene, and carbon nanofibres (CNFs), are thus being explored as anodes in LIBs. CNFs can provide much higher capacity than traditional graphite, because lithium ions can be inserted into the pores and defects of CNFs. The capacity of PAN-based CNFs after carbonisation at 1000°C is 450 mA h/g [63], much higher than that of graphite at 372 mA h/g. In addition, CNFs hybridised with other atoms will reach higher capacity. Zhang et al. have demonstrated that the nitrogen content can be maintained at 15.3 at. % at a low carbonisation temperature of 550°C in electrospun PAN-based CNF films. Since the defects created by nitrogen atoms provide additional reaction sites for lithium ions, a high capacity of 550 mA h/g can be generated [64].

Vanadium redox flow batteries (VRFBs) are also secondary (rechargeable) batteries. Unlike LIBs, the electroactive substances of VRFBs are dissolved in the electrolyte, where the energy is stored. This electrochemical cell consists of two half-cells, both of them having an electrode, separated by an ion exchange membrane, as shown in Figure 2.2. The discharge process in VRFBs is comparable to that of conventional batteries storing the energy in the electrodes, involving an oxidation reaction at the negative electrode and a reduction reaction at the positive one. This converts the chemical energy in the electrolyte to electrical energy. Unique to VRFBs, the electrolyte is stored externally and pumped into each half-cell, allowing the chemical energy to be stored separately from the stack. This design enables independent customization of the battery's energy capacity and power output. For example, the energy storage capacity of the battery can be increased by increasing the volume of the electrolyte, that is, by increasing the size of the storage tank, and the available power of the battery can be increased by increasing the size and number of electrochemical cells in the battery [65].

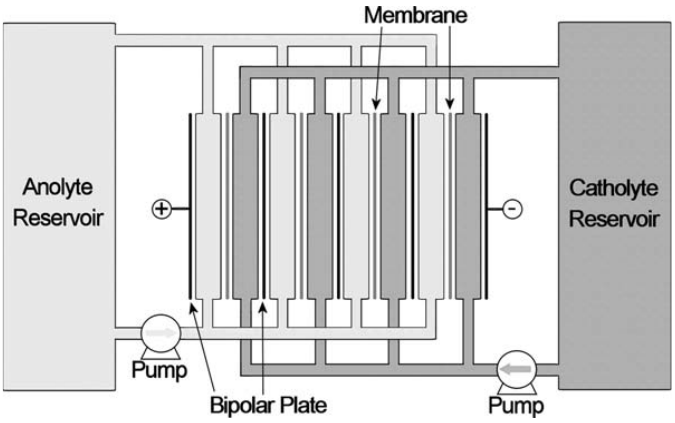

Figure 2.2. A schematic of a VRFB [65]

2.1.2 Supercapacitors (SCs)

SCs are another important type of electrochemical energy storage devices, whose origin date back to the mid-19th century, even though their real development and application have been really promoted in recent decades. Compared to batteries, they provide higher power densities and longer cycle life. In their early development, they were referred to as "Boost Caps," emphasizing their ability to provide instantaneous high power [66]. With regards to their charge storage mechanism, SCs generally exist in the form of electrical double-layer capacitors (EDLCs), pseudocapacitors, and hybrid supercapacitors [66]. **EDLCs** represent one of the most prevalent types of supercapacitors, comprised of two electrodes, a separator, and an electrolyte. As depicted in Figure 2.3, EDLCs store charge physically through the formation of the double layer at the electrode/electrolyte interface, when a voltage (or potential difference) is applied between the electrodes, leading to electrostatic charge accumulation. To achieve high capacitance in EDLCs, the focus is on using electrode materials that have both high specific surface area and good electrical conductivity [67]. The charging and discharging mechanism in EDLCs is markedly reversible, contributing significantly to their notably extended cyclability [68]. Nonetheless, they are significantly limited due to their lower energy density values. Carbon-based materials have garnered widespread utilisation in EDLCs, mainly due to their advantages of remarkable specific surface area, high electrical conductivity, and chemical stability.

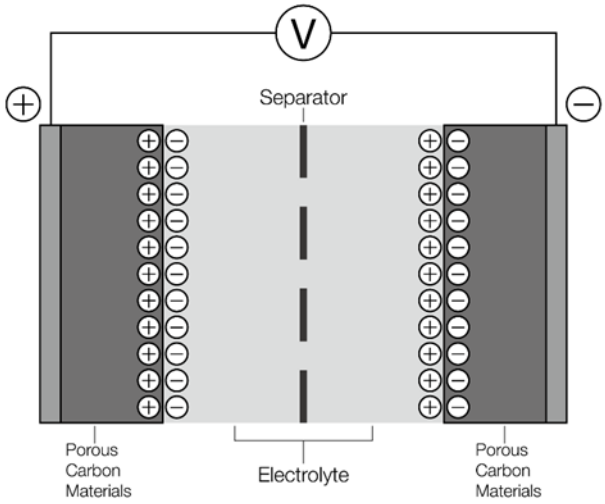

Figure 2.3. Charge storage mechanism of EDLCs

The concept of pseudocapacitance was first defined by B. E. Conway in his work, "Electrochemical Supercapacitors: Scientific Fundamentals and Technological Applications", where it is described as capacitance generated on the electrode surface through fast and reversible redox reactions [69]. Contrary to EDLCs, **pseudocapacitors** are fundamentally rooted in Faradaic processes. Traditional pseudocapacitive materials, such as oxides/hydroxides of metals like RuO_2, MnO_2, Co_3O_4, NiO, $Ni(OH)_2$, Fe_2O_3, and V_2O_5, have been extensively explored in SCs for their multiple oxidation states and rapid charge-discharge capabilities [70]. However, the notably low power densities and poor cyclic performance of these materials significantly hinder their viability for SCs applications. Furthermore, the limited electron transfer rates—attributable to the inherently low electrical conductivity of metal oxides/hydroxides—serve as a significant barrier to their adoption in applications requiring high power density SCs. Additionally, the poor cyclic stability, which can be attributed to morphological deterioration caused by particle expansion and agglomeration during the charge-discharge cycles, further limits their effectiveness. To mitigate these drawbacks, the development and synthesis of electrodes with high porosity and conductivity, along with the full utilisation of various redox couples, are seen as promising strategies to enhance energy and power densities [71]. Precise design and chemical modification of components to develop

porous nanostructures can alleviate the stress caused by electrode expansion and particle agglomeration, providing more sites for ion adsorption and/or redox active sites for charge transfer reactions [72]. Moreover, combining metal oxides/hydroxides with conductive materials, such as CNFs, CNTs, and graphene, not only accelerates reaction kinetics by shortening the diffusion path and facilitating rapid transport of electrolyte ions but also enhances the synergistic effects between pseudocapacitance and EDLC [70]. For instance, Qi et al. demonstrated the synergistic effects of combining conductive EDLC material (CNFs) with non-conductive pseudocapacitive material (MnO_2), achieving high specific energy and power [73]. Furthermore, functional groups of heteroatoms in carbon, such as oxygen and nitrogen, also contribute to pseudocapacitance [74], [75]. Qiu et al. showed that in aqueous electrolytes, oxygen-containing functional groups, especially carboxyl and carbonyl groups, not only enhance the diffusion of electrolyte within the electrode but also improve capacitance through the introduction of pseudocapacitance. However, an excessive amount of oxygen functional groups can block pores, leading to poor electrochemical performance [75].

2.1.3 Hybrid systems

Hybrid energy storage systems, which usually combine two energy storage technologies, offer a solution that achieves improved performance by combining appropriate features of different devices [76]. For example, enhancing the power density and charging speed of batteries, as well as increasing the energy density of SCs. Hybrid energy storage systems typically involve pairing electrodes with distinct storage mechanisms, like a capacitive electrode (storing energy through the double layer formation) and a battery-type electrode (storing energy by the development of faradaic reactions). This hybrid device concept was initially introduced by Amatucci's group. It involved the integration of a positive activated carbon-based capacitor electrode with a negative $Li_4Ti_5O_{12}$ faradaic electrode in an organic electrolyte [77]. Moreover, Khomenko et al. utilised a pre-lithiated graphite as the negative electrode and activated carbon for the positive electrode, aiming to enhance the working voltage [78]. Brousse et al. tested

with a hybrid capacitor in an aqueous solution, using MnO_2 and activated carbon as the positive and negative electrodes respectively [79].

2.2 Carbon materials as electrodes in supercapacitors

Supercapacitors (SCs), with their high-power density, fast charge-discharge capability and remarkable cycling stability, show a significant potential in meeting some of the contemporary energy demands. However, as previously mentioned, the main drawback of SCs is their low energy density. The key point to enhance the performance of SCs and broadening their application scope lies in the development and integration of innovative active electrode materials. These materials play a crucial role in improving the electrochemical performance of SCs, particularly by increasing their energy storage capacity. Moreover, in recent years, the emergence of portable and, mainly, flexible electronic devices have also increased interest in the development of advanced electrodes materials, such as carbon nanotubes (CNTs) or carbon nanofibres (CNFs).

As previously mentioned, electrodes are key components influencing the electrochemical performance of SCs. To meet the requirements of high energy and power density values, active electrodes in SCs need to exhibit several characteristics such as high specific surface area/pore size distribution, excellent electrical conductivity, suitable surface chemistry and appropriate mechanical/chemical properties. Carbon materials are ideal candidates for this application being widely available, environmentally friendly, and offering the possibility of achieving all these requirements at a reasonable cost. Currently, various types of carbon materials, including activated carbons, CNTs, graphene derivatives, and CNFs, are being used in SCs.

2.2.1 Activated carbons (ACs)

ACs are the most commonly used electrode materials in SCs due to their excellent properties as high specific surface area, good electrical conductivity, rich surface chemistry, ease of preparation and chemical stability. Moreover, ACs can be prepared from various precursors, including by-products from the carbochemical/petrochemical industries and biomass residues,

using physical or chemical activation methods [80], both factors greatly influencing the characteristics and subsequent electrochemical performance of ACs. As described before, the design and development of ACs with tailored pore size distribution, surface chemistry, and morphology is key for the improvement of SCs performance, so that the efforts of most of researchers in the field have been focused on optimising their synthesis methods [80].

From both cost and environmental perspectives, the utilisation of biomass wastes as raw materials for ACs is a focal point of current research. Transforming these precursors into ACs for being used as electrodes in SCs addresses waste management issues while simultaneously generating revenue for supply chains [81]. Within the variety of biomass resources, plant-based biomass emerges as a promising candidate as it exhibits a high degree of graphitisation, controllable defects, low oxygen content, and high nitrogen content, all these factors contributing to an enhanced conductivity and yield. Conversely, fruit-based biomass, primarily composed of crude protein and lipids, inherently contains nitrogen, phosphorus, and other heteroatoms. Notably, fruit peels yield more ACs compared to fruit pulp, although the AC yield from fruit-based biomass is generally lower than that from plant-based resources [82]. Beyond plants and fruits, biomass resources derived from animals, microorganisms, and humans also show potential use due to their natural abundance and chemical stability. Additionally, other biomass precursors such as office and industrial wastes, seeds, flowers, and nut-based wastes are becoming increasingly recognized for ACs preparation. Their hierarchical porous structure, high specific surface area, and heteroatom doping make them suitable materials for ACs production [83], [84].

To facilitate the development of fast charging capabilities and enhanced energy density in these energy storage devices, it is crucial to ensure rapid charge kinetics or swift movement of charge carriers across the electrode surface. In this regard, the activation of carbon derived from bio-waste presents a promising avenue for creating fine porosity, including micropores and mesopores, along with heteroatom doping. Furthermore, physical or chemical activation techniques can induce fractal granularity and porosity [85]. For example, Lee et al. reported a

coconut shell-derived activated carbon as an electrode in SCs. This AC showed a high specific surface area of 1567 m^2/g, with a balanced distribution of micropores and mesopores. The sample demonstrated superior electrochemical performance, reaching 449 F/g at 1 A/g in 6 M $LiNO_3$ aqueous solution [86]. Saha et al. prepared lignin-based ACs for SC electrodes using different activation methods. They discovered that the lignin-based ACs, activated physically with CO_2, achieved a specific capacitance of 102.3 F/g in 6 M KOH solution with a surface area of 624 m^2/g. Conversely, ACs prepared with KOH chemical activation exhibited a higher surface area of 1148 m^2/g, yet their specific capacitance was lower at 91.7 F/g [87].

Table 2.1 summarizes previously reported results on the synthesis of ACs for SCs. This includes the types of raw precursors used, activation methods followed, specific surface areas developed on the ACs synthesized, experimental parameters used for their electrochemical characterization, and the capacitances measured.

Table 2.1. Textural and electrochemical properties of previously reported ACs as electrodes in SCs

Biomass-based precursor	**Activation method**	**Surface area (m^2/g)**	**Capacitance (F/g)**	**Electrolyte**	**Applied current density**	**Ref.**
Chicken eggshell	KOH	221	297	1 M KOH	0.2 A/g	[88]
Rice	$ZnCl_2$	2106	398	6 M KOH	0.2 A/g	[89]
Seaweeds	Thermal	1307	264	1 M H_2SO_4	0.2 A/g	[90]
Lignin	CO_2	624	102.3	6 M KOH	2 mV/s	[87]
Lignin	KOH	1148	91.7	6 M KOH	2 mV/s	[87]
Sucrose	NH_4NO_3	518	277	1 M H_2OS_4	0.5 mA	[91]
Watermelon	KOH	2936–3420	150.6	6 M KOH	0.2 A/g	[92]
Coconut shell	KOH	1567	449	6 M $LiNO_3$	1 A/g	[86]

2.2.2 Carbon nanotubes (CNTs)

CNTs are another potential active electrode material for supercapacitors (SCs) due to their high surface area, but mainly to their excellent electrical conductivity, and mechanical strength [93]. The structure of CNTs is formed by rolling one or multiple layers of graphene into a cylindrical shape (refer to Figure 2.4), where graphene is a two-dimensional material consisting of carbon

atoms arranged in a honeycomb lattice through sp^2 hybridization. The diameter of single-walled carbon nanotubes (SWCNTs) typically falls within a few nanometers, while multi-walled carbon nanotubes (MWCNTs) consist of several concentrically nested single-walled tubes, with diameters reaching up to several tens of nanometers. Moreover, the structure of CNTs' ends significantly influences their properties; for instance, closed ends may restrict access to charge carriers or other molecules, while open ends provide more active sites for chemical activity. The internal space of carbon nanotubes, which can be utilized for catalyst loading, is especially crucial in applications within energy storage and biomedical fields [94].

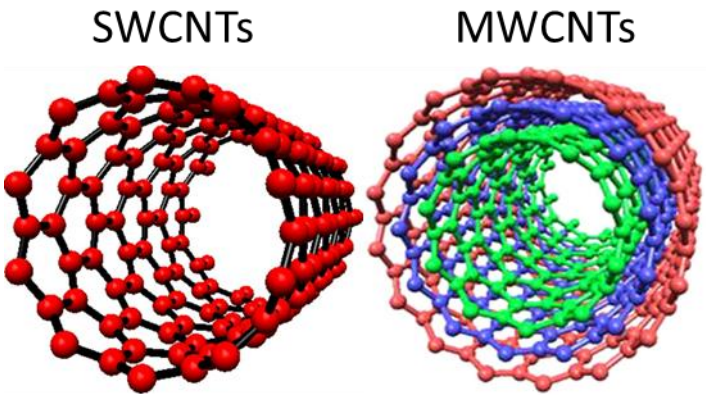

Figure 2.4. Surface and Internal view of SWCNTs and MWCNTs [94]

In 1997, Niu et al. first proposed the application of CNTs as electrodes in SCs. MWCNTs were functionalized in nitric acid, introducing functional groups onto their surface [95]. These functionalized MWCNTs exhibited a specific surface area of 430 m^2/g, a gravimetric capacitance of 102 F/g, and an energy density of 0.5 Wh/kg at 1 Hz in a single-cell device using 38 wt% sulfuric acid as electrolyte. Despite the removal of 90% of catalyst, the remaining catalyst within the MWCNTs (primarily inside the tubes) clearly impacted the SC performance. The presence of functional groups and residual catalyst induced pseudocapacitance. Thus, the operation of that CNTs-based SC involved both Faradaic and non-Faradaic processes. The redox response observed on the CV recorded on SWCNTs-based electrodes also confirmed the pseudocapacitive contribution due to functional groups and impurities [96].

As previously mentioned, in EDLCs, the amount of electrical charge accumulated due to electrostatic attraction depends on the surface area of the electrode/electrolyte interface accessible to the charge carriers. A higher surface area of the electrode material could lead to increased capacitance, provided that the charge carriers can fully access this area. However, a higher surface area does not always equate to increased capacitance, as the capacitance is also influenced by the pore size, distribution, and conductivity of the material. Higher capacitance can be achieved by optimizing all related factors. For instance, vertically aligned CNTs with a diameter of about 25 nm and a specific area of 69.5 m^2/g demonstrated a specific capacitance of 14.1 F/g and exhibited excellent rate capability. These characteristics were superior to those of entangled CNTs, attributed to their larger pore size, more regular pore structure, and increased conductive pathways [97].

Frackowiak et al. investigated the impact of the structure and diameter of CNTs, as well as their microtexture and elemental composition on capacitance [98]. They discovered that capacitance increases with an increase in specific surface area. The lowest value was observed in CNTs with closed tips and graphitized carbon layers, where the volume of mesopores available for ion diffusion and the active surface area for the formation of the electric double layer are extremely limited. Nanotubes with numerous edge planes were proved to be most efficient for charge collection. Moreover, larger diameter and rigid CNTs exhibited only moderate performance. This may be attributed to the diameter of their central channels being too large compared to the size of solvated ions [95]. While, Ahn et al. discovered that CNTs with a smaller diameter (33 nm) exhibited greater capacitance than those with a larger diameter (200 nm), owing to the increased surface area of the smaller diameter-based CNTs [99].

The capacitance of CNT-based SCs can be enhanced through chemical activation, functionalization, as well as heat and surface treatment [100]. Following strong oxidation in HNO_3, a significant increase in the specific capacitance was observed due to the enhancement of functional groups on the CNT surface [98]. Enhanced capacitance values were reached post-activation: in some cases, the capacitance almost increased 7-fold, which, for example, was

attributed to the highly developed microporosity of pure MWCNTs through chemical KOH activation [101]. The activated material retained its nanotubular morphology with numerous defects on the outer walls, leading to an increased micropore volume while maintaining notable mesoporosity. The introduction of different functional groups also impacts the electrochemical performance of CNTs. The incorporation of surface carboxyl groups resulted in a 3.2-fold increase in capacitance due to the enhanced hydrophilicity of MWCNTs in aqueous electrolytes. Conversely, the introduction of alkyl groups led to a significant reduction in capacitance. Furthermore, specific capacitance can also be improved through fluorine functionalization and heat treatment [102]. Fluorination of SWCNT walls transformed non-polar SWCNTs into polar ones by forming dipole layers on the walls, enhancing solubility in deionized water. Fluorinated samples exhibited lower capacitance than untreated raw samples before heat treatment due to an increase in micropore area and a decrease in average pore diameter. However, post-heat treatment, the specific capacitance of fluorinated samples surpassed that of raw samples due to additional redox reactions prompted by residual oxygen gases on the electrode surface. The reduction in equivalent series resistance (ERS) is attributed to improved conductivity facilitated by the carrier induced by functionalization [103]. Pyrrole treated-functionalized SWCNTs exhibited high values of capacitance (350 F/g), power density (4.8 kW/kg), and energy density (3.3 kJ/kg) [104]. High capacitance was also achieved through plasma surface treatment with NH_3, enhancing the total surface area and wettability of MWCNTs [105].

2.2.3 Graphene and related materials

Graphene is a two-dimensional material composed of a single layer of carbon atoms closely arranged in a honeycomb-like hexagonal pattern [106], which exhibits outstanding properties. Firstly, it is an excellent conductor with an ultra-high electron mobility, meaning that electrons can move through its structure very rapidly. Furthermore, even though it's only one atom thick, it is known to be the strongest material, possessing a Young's modulus that exceeds steel by over 100 times [106]. Additionally, it is also characterised by its exceptional thermal conductivity and transparency. In graphene production, two primary approaches are used: top-

down and bottom-up methods. The top-down methods involve exfoliating or breaking down larger graphite structures into graphene sheets. This can be achieved through mechanical or chemical processes, like sonication in liquid media or chemical of graphite. On the other hand, the bottom-up methodologies involve synthesizing graphene from smaller molecules or atoms. This is typically done through chemical vapor deposition (CVD) on metal substrates, where hydrocarbon gases are decomposed to form graphene layers directly on the substrate [107]. The production of graphene via CVD usually have high-quality but in small amounts and with a high cost [108].

In supercapacitors (SCs), graphene is considered the ideal electrode material, from a theoretical point of view, due to its high conductivity and specific surface area, which can increase the contact area with the electrolyte, thereby enhancing its energy storage capacity. However, the application of graphene in SCs still presents some challenges. Graphene sheets tend to restack in liquid mediums, significantly decreasing their accessible surface area. Moreover, the large-scale, high-quality production of graphene remains a challenge and might lead to higher costs in commercial applications. Due to these challenges, researchers have started using graphene-related materials as graphene oxide (GO) or reduced graphene oxide (rGO) as alternatives. GO is a single layer of graphite oxide and by definition a graphene sheet functionalised by various oxygenated functional groups, the most prevalent being epoxy, hydroxyl, carboxylic, and carbonyl groups [109]. It offers distinct advantages such as a high surface area and the presence of these functional groups, enhancing its compatibility and interaction with other materials. GO can be directly synthesized from graphite powder, improving the sustainability of this material. The reduction of GO through various chemical, thermal, mechanical, and green processes to remove oxygen-containing functional groups results in rGO [110]. The high concentration of oxygen functional groups in GO disrupts the extended conjugation between the hexagonal rings. This disruption leads to a reduction in π-electron conjugation in GO, rendering the material non-conductive [111]. The chemical structures of GO and rGO are illustrated in Figure 2.5.

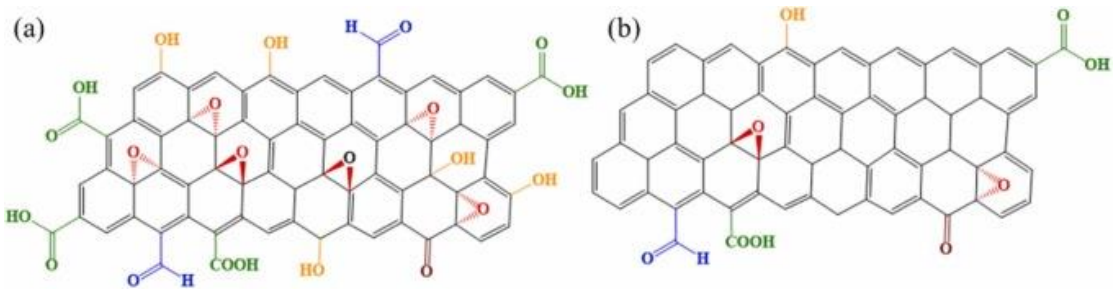

Figure 2.5. Chemical structures of (a) GO and (b) rGO [112]

By integrating GO/rGO with different materials, researchers aim to capitalize on their unique properties while addressing graphene's limitations [109]. Rajagopalan et al. developed an electrode for SCs based on GO. Their process involved reacting KOH with graphene oxide, followed by chemical reduction using hydrazine. This technique yielded rGO electrodes exhibiting a significantly enhanced specific capacitance of 253 F/g in a 2 M H_2SO_4 solution, notably superior to rGO that had not undergone reaction with KOH [113]. Sun et al. introduced a method for the simple transformation of GO into rGO under ambient conditions using flame-induced reduction. This rGO was then evaluated as an electrode material for SCs, testing its electrochemical performance. The rGO prepared through this method exhibited a specific surface area of 274.9 m^2/g and demonstrated a high specific capacitance of 212 F/g in a 2 M KOH solution. They attributed the excellent capacitive performance in the KOH aqueous solution to the high surface area and the presence of residual oxygen-containing groups in the rGO [114].

2.2.4 Carbon nanofibres (CNFs)

CNFs are characterized by their large aspect ratio, exceptional electrical conductivity, thermal/mechanical properties, and flexibility. Moreover, various structures can be formed through textile and papermaking processes, thus leading to CNFs and derived fabrics which can be used as ideal binder-free, self-supporting, strong, and flexible electrodes. This has led to their extensive application in advanced electrochemical energy storage devices, particularly in supercapacitors (SCs).

Due to their small diameter, ranging from tens to hundreds of nanometers, CNFs typically exhibit a high specific surface area. However, pure CNFs synthesized directly from polymers through electrospinning or other technique often face challenges in providing superior performance in SCs. This is primarily due to the absence of an appropriate porous structure in the CNFs; hence, it becomes essential to engineer the porous structure within CNFs. One popular method for creating nanoscale pores in CNFs involves physical or chemical activation. Kim et al. obtained polyacrylonitrile (PAN)-based CNFs with a high specific surface area of 1230 m^2/g by using 30 vol.% steam treatment at 700°C, which achieved a capacitance of 173 F/g when the CNFs mat was used as an electrode for SCs [115]. Zinc is an effective etching agent for carbon atoms. Kim et al. obtained a surface area of 550 m^2/g by activating CNFs using 5 wt.% $ZnCl_2$. When applied to SCs, a high capacity of 140 F/g was achieved [116]. Besides activation techniques, another method to enhance the surface area of CNFs involves eliminating sacrificial components from the electrospinning mixtures. Tran et al. obtained a surface area of 1614 m^2/g in electrospun porous CNFs through the selective removal of Nafion. When used as electrodes in SCs, they exhibit a high specific capacitance (210 F/g) [117].

Heteroatom doping appears as a fascinating approach to enhance the electrochemical performance of CNFs. It not only introduces nanoscale pores that benefit the double layer formation but also aids in pseudocapacitance through the attachment of functional groups. Kim et al. developed Silicon-doped CNFs using tetraethoxysilane (TEOS) as silicon precursor. They discovered that the incorporation of Si significantly improved the formation of pores in CNFs. The resulting CNFs exhibited an exceptionally large specific surface area of 1386.91 m^2/g, with a substantial proportion of this surface area (38%) being attributable to mesopores, thus achieving a high specific capacitance of 91.95 F/g in an organic electrolyte (1.5 M tetraethylammonium tetrafluoroborate solution in acetonitrile) [118]. The addition of B_2O_3 to electrospinning solutions was another approach to prepare PAN-based CNFs, as the gases emitted during the reaction of B_2O_3 and C during carbonisation, contributed to the development of porosity onto the CNFs. Additionally, the [O]BN functional groups were active in KOH

aqueous electrolytes, improving the pseudocapacitance [119]. Yan et al. studied the electrochemical performance of N/P co-doped CNFs in SCs. They pointed out that the co-doped material provided more reversible redox reactions, resulting in an outstanding capacity of 203 F/g after 8000 cycles [120].

Combining various forms of carbon materials with CNFs has also demonstrated superior electrochemical characteristics. Graphene stands out as one of the most noteworthy materials in this context. Initially, the inherent mesh-like structure of CNFs makes them an ideal substrate for graphene sheets. Moreover, graphene has high electrical conductivity, which can significantly enhance the composite's overall conductivity. Additionally, the superior thermal conductivity of graphene further facilitates more efficient heat dissipation during charge-discharge cycles, thereby elevating the stability and safety of the device. Although both materials are relatively costly, their performance benefits make them cost-effective in the long run, while also being environmentally friendly. Zhou et al. have mixed graphene nanosheets with PAN electrospinning solutions to fabricate precursor nanofibres, which are subsequently carbonised to create a composite material of graphene/CNFs for SCs electrodes. They discerned that the incorporation of 1 wt.% of graphene nanosheets into the solution could more than double the capacitance of the electrodes whilst substantially diminishing their internal resistance [121]. Kim et al. described the fabrication of an innovative hierarchical porous CNF/graphene composite, doped with MnO_2, and crafted into a web-like structure through electrospinning techniques. The infusion of graphene into these MnO_2/HPCN/G webs not only amplifies the specific capacitance but also improved the composite's performance under high-rate electrochemical conditions [122]. Zhang et al. fabricated composite films, comprised of graphene and CNFs, exhibiting good electrical conductivity, mechanical robustness, and electromagnetic shielding capabilities. These films were achieved by annealing GO-aPAN films at elevated temperatures, also demonstrating a remarkable tensile strength of 10.4 MPa at a 5% strain. This unique structure endowed the films with exceptional elastomeric behaviour and robust folding stability, evidenced by their outstanding resistance to degradation even after

1,000 folding cycles. Such films hold promising potential for applications in flexible electronic devices [123].

2.3 Precursors for the production of CNFs

2.3.1 Traditional precursors

The selection of a suitable precursor is a key point in the preparation process of carbon nanofibres (CNFs), as it greatly impacts on both, their final cost and mechanical/electrochemical properties.

Polyacrylonitrile (PAN), a synthetic polymer with a linear formula of $(C_3H_3N)_n$, stands out as one of the most traditional and widely used precursors [124]. Major advantages of PAN include its high carbon yield (approximately 50% [125]) which makes it economically attractive. Moreover, CNFs derived from PAN often exhibit superior oriented and graphitic structures, leading to outstanding mechanical and electrical properties [126].

The transformation from PAN to CNFs involves several crucial steps. Stabilisation is the initial stage, entailing the oxidative treatment of PAN fibres in air to promote cross-linking and prevent fibre melting in subsequent steps [127]. This is followed by carbonisation, where stabilised fibres are subjected to thermal treatment in an inert atmosphere, releasing various gases and forming a carbon structure [128]. For applications demanding higher crystallinity, PAN-based CNFs can be further heated for graphitisation [128]. However, while PAN offers numerous advantages in CNFs preparation, it also comes with certain challenges. Primarily, it necessitates a meticulous stabilisation process to avoid fibre melting [126]. Furthermore, toxic gases might be released during the processing [129]. Also, being a petroleum-based polymer, its cost can fluctuate with international oil prices, and its environmental friendliness remains a concern.

Apart from PAN, pitches are also traditional precursors for the production of CNFs, due to their availability, high carbon yield (approximately 60%) and low cost. Even though pitches derived

from the carbochemical or petrochemical industries are the most important ones considering their production volume, their specifications (in terms or viscosity, softening point, and C yield) are not suitable for CNFs production. In this context, synthetic pitches, obtained by polymerisation of polycyclic aromatic hydrocarbons (PAHs) as naphthalene, phenanthrene, anthracene appear as interesting alternatives for CNFs production. Their primary advantage lies on their ability to yield CNFs with a high degree of graphitisation, thus achieving appropriate thermal and electrical conductivities [130]. However, the use of pitches as precursors is not without challenges. Firstly, their spinning process is relatively intricate [131]. Secondly, independently of their origin, for a pitch to be a suitable precursor for CNFs preparation, it has to fulfil some basic requirements (softening point, absence of solid particles, etc). Regarding the spinning procedure, pitches must first be dissolved in appropriate solvents under specific conditions to form stable solutions, followed by spinning either through wet or dry spinning techniques under precise temperature control to ensure fibre uniformity and quality. Post-spinning, pitches-derived fibres require stretching and further treatments to enhance their orientation and mechanical properties [131].

Among the numerous precursors utilized for the synthesis of CNFs, polyvinyl alcohol (PVA) has increased in interest in recent years. PVA is a water-soluble synthetic polymer with stable chemical properties which makes it a promising candidate for CNFs fabrication [132]. To optimize its spinning process, thus attaining high-quality fibres with desired properties and performance, PVA is often blended with other carbon sources or catalysts, such as PAN [133], lignin [134], and acetylene black [132]. Subsequently, it undergoes specific thermal treatment steps, such as carbonisation and activation, to form the desired nanofiber structures [135]. Compared to other traditional precursors, like PAN or pitches, PVA's main advantages lie on its low toxicity, reduced cost, and readily accessible nature. This positions PVA as an environmentally friendly and cost-effective choice for CNFs fabrication. However, it still faces certain challenges. These include optimizing several fabrication parameters, such as temperature, time of processing, and the ratio of PVA to other components, to yield CNFs with

the required properties [135]. Additionally, PVA's water solubility might compromise its stability in certain applications, so that further exploration on this topic is required.

The fabrication of CNFs heavily relies on the choice of precursors. Each precursor presents particular advantages, from the high carbon yield and superior graphitic structures of PAN-derived CNFs, the impressive graphitisation potential of pitch-based CNFs, to the environmental and economic benefits of PVA. However, these precursors are not without challenges, from intricate processing requirements to concerns about cost fluctuations and environmental impact. It is evident that while these traditional precursors have paved the way for significant advancements in CNFs fabrication, there remains room for exploration. As the world continues to move towards sustainable and green solutions, there is an increasing need to identify alternative biopolymers that can serve as precursors. Such alternatives could potentially overcome the limitations of traditional precursors, offering improved performance, cost-effectiveness, and environmental friendliness.

2.3.2 Bio-polymeric precursors

As previously mentioned, carbon fibres derived from traditional precursors exhibit several advantages in terms of mechanical strength, modulus, degree of graphitisation, etc. However, the high cost and environmental concerns associated with their manufacturing process are stimulating research into alternative bio-based precursors and environmentally friendly processing routes. In recent years, the primary alternatives for bio-based precursors have been lignin and cellulose, both of which are abundant and renewable sources.

2.3.2.1 Lignin-based precursors

Lignin is a complex organic polymer widely found in plant cell walls and is one of the most abundant renewable organic resources on earth [136]. Chemically, lignin is primarily composed of phenolic monomers such as p-hydroxyphenylpropanol, phenol formaldehyde, and phenone, which are connected through various types of chemical bonds, including ether and carbon-

carbon bonds. The complexity of the resulting structure confers lignin a high degree of stability and resistance to biodegradation.

Lignin can be isolated using different delignification processes such as the Kraft process (using sodium hydroxide and sodium sulphide) and the Organosolv process (using organic solvents) [137]. The different extraction methods employed result in varying purity levels and lignin fraction sizes, which affect their subsequent fibre-spinning performance and thus the properties of the carbon fibres [137].

In the last years, numerous studies have focused on the conversion of lignin into carbon nanofibres (CNFs). Dallmeyer et al. reported the fabrication of kraft lignin-based CNFs through electrospinning and thermally induced inter-fibre bonding. Owing to the inverse relationship between the external surface area of cylindrical fibres and their diameter ($4\pi DL/\pi D2L = 4/D$), the diameter of CNFs is nearly two orders of magnitude smaller than that of activated carbon fibres. Consequently, even in the absence of any internal porosity, CNFs exhibits a considerably large surface area [138].

Furthermore, CNFs prepared by combining lignin with other polymers or particles offer certain advantages. According to Teng et al., the electrical conductivity of CNFs was increased from 2.3 to 3.0 S/cm when 6 wt% of MWCNTs were incorporated into electrospun sulphate kraft lignin fibres [139]. Wang et al. reported that melt-spun carbon fibre mats, obtained by incorporating a certain proportion of low-melting-point polymer additives with Organosolv lignin, exhibited favourable electrochemical performance as an anode material in lithium-ion batteries (LIBs). The specific capacity reaches as high as 445 mA h g^{-1}, which is comparable to carbon fibre mats derived from PAN [140]. PAN is also used to blend with lignin to improve the performance of CNFs in SCs. Lei et al. reported on the development of CNFs based on PAN/Lignin for use in flexible SCs. The CNFs exhibited a specific capacitance of 134.3 F/g at a current density of 1 A/g in a solid-state SCs [141].

2.3.2.2 Cellulose-based precursors

Cellulose is a complex polysaccharide primarily composed of glucose unit, which are interconnected via β-1,4-glycosidic bonds, conferring it a high degree of stability and tensile strength. However, when utilised for the fabrication of carbon fibres, cellulose suffers from a low carbon yield, ranging from 10 to 30%. This results in a significant reduction on their mechanical strength when following thermal treatment. Compared to PAN-based CNFs, cellulose-based ones exhibit lower mechanical strength and modulus. Nonetheless, due to its eco-friendly nature and abundant availability in the natural environment, cellulose continues to garner considerable attention from researchers.

Cellulose nanofibers are mainly fabricated through the electrospinning technique utilising various cellulose derivatives, as researchers have found some difficulties to produce them directly because of its poor solubility in most common solvents. In research conducted by Deng and colleagues, cellulose nanofibres were synthesised by electrospinning of cellulose acetate, which was subsequently deacetylated using a sodium hydroxide solution in ethanol [142]. Kuzmenko et al. reported that partial regeneration of cellulose, achieved through a mixture of ammonium hydroxide and ammonium chloride, led to a 20% increase in carbon yield in the resulting cellulose nanofibres [143]. Byrne et al. employed an ionic liquid as cosolvent and successfully prepared fibres of PAN/cellulose acetate and PAN/raw cotton through electrospinning [144]. However, the long-term effects and environmental implications of ionic liquids remain somewhat uncertain.

CNFs derived from electrospun cellulose nanofibres have attracted considerable attention in electrochemical and separation applications. One particularly promising application consists on their use as anode materials for sodium-ion batteries (SIBs). Luo et al. have demonstrated the impressive electrochemical attributes of cellulose-derived CNFs, including a high reversible capacity, robust rate capability, and excellent long-term stability [145]. Moreover, they show good electrochemical performance in SCs. For example, Cai et al. employed electrospinning techniques to produce cellulose acetate nanofibers and, by adjusting its degree of deacetylation,

fabricated inter-bonded CNFs. These fibres demonstrated a high specific capacitance of approximately 241.4 F/g at a current density of 1 A/g with commendable cycling stability on this application [146].

2.4.2.3 Poly(lactic acid)

In addition to lignin and cellulose, Poly(lactic acid) (PLA) also show potential as precursors for CNFs [147]. PLA is a biodegradable polymer composed of lactate molecules linked by ester bonds. Lactic acid can be sourced from renewable resources like corn and sugarcane, making PLA an eco-friendly alternative to conventional plastics. PLA finds extensive applications in fields such as medicine [148], packaging [149], and textiles [150]. However, PLA exhibits thermal instability, and undergoes rapid molecular weight loss upon thermal treatment at processing temperatures [151]. Consequently, it is typically employed as a sacrificial phase for preparing PAN-based porous carbon nanofibres [152]. Studies utilising PLA alone as a precursor for CNFs are quite limited, with the primary challenge being its low thermal stability [153]. Therefore, it is essential to improve the stabilisation process of PLA to enhance its thermal stability.

2.4.2.4 Chitosan (CTS)

CTS is a natural polysaccharide derived from chitin, which is found in the exoskeleton of shellfish such as crabs, shrimp, and other crustaceans, as well as in the cell walls of fungi. Chemically, chitosan is composed of repeating units of glucosamine (2-amino-2-deoxy-β-D-glucose) and N-acetylglucosamine (N-acetyl-2-amino-2-deoxy-β-D-glucose). The structure of chitosan is similar to that of cellulose, with the primary difference being the presence of amino groups on the glucosamine units, which makes chitosan cationic (positively charged) in acidic to neutral solutions. CTS exhibits excellent biocompatibility and degradability, holding significant promise in the biomedical sector. Developed and potential applications of CTS encompass wound dressings [154], bone repair materials [155], artificial dialysis membranes [156], drug delivery systems [157], and agriculture [158]. However, there are challenges in

preparing chitosan nanofibres through electrospinning, due to the presence of numerous amino groups in its structure. This results in a polycationic nature, which in turn increases the surface tension of the precursor solution [159]. Therefore, CTS is typically blended with other polymers to facilitate its spinning process and subsequent application in SCs. For instance, Ken et al. mixed CTS with polyvinylpyrrolidone (PVP) to fabricate composite fibres, which were treated with a $KNO_3/NH_4H_2PO_4$ solution and subsequently carbonised to produce N,P co-doped carbon nanofibres for their use as supercapacitor electrodes. Due to the contribution of pseudocapacitance, the resulting electrodes exhibited a capacitance of 358.7 F/g at a current density of 1 A/g [160]. In fact, most studies on the use of chitosan for energy storage materials involve its conversion into activated carbon. Sultan et al. used CTS as the precursor and employed a $ZnCl_2$ chemical activation method to prepare activated carbon for supercapacitor electrodes [161]. To enhance their electrochemical performance, CTS-based porous carbons are typically combined with metal oxides, graphene, or polyaniline [162]. The electrochemical performance of various reported chitosan-based composite electrodes are presented in Table 2.2.

Table 2.2. Chitosan-based electrode in supercapacitors

Electrode material	**Surface area (m^2/g)**	**Capacitance (F/g)**	**Electrolyte**	**Applied current density**	**Ref.**
KOH activated chitosan-based carbon	1129.6	316	6 M KOH	0.2 A/g	[163]
Chitosan-ZnO/polyaniline ternary nanocomposite	116.25	541.03	1 M H_2SO_4	175 mA/g	[164]
Chitosan/GO composite	-	320	6 M KOH	1 A/g	[165]
Chitosan/rGO composite	-	274	1 M H_2SO_4	0.5 A/g	[166]
Chitosan/polyaniline hybrid electrode	-	83.34	1 M H_2SO_4	0.1 A/g	[167]
Chitosan-derived hierarchical porous carbon	3532	455	6 M KOH	-	[168]

2.5 Synthesis of carbon nanofibres

2.5.1 Traditional production techniques

The history of fibre spinning techniques spans a significant period, with continuous efforts made since ancient times to develop superior methods for producing high-quality fibres. From natural to synthetic fibres, each spinning technique reflects the technological advancements and societal needs of its era. Today, fibres are used in a wide range of applications, from clothing to advanced technological materials. Therefore, understanding traditional fibre spinning methods is crucial in the fields of textiles and material science. Among these traditional fibre spinning techniques, methods such as melt spinning [169], wet spinning [170], and dry spinning [171] have been extensively reported and studied.

The melt-spinning method originated in the late 19th century. With the emergence of synthetic polymers, this technique garnered widespread application. Its operational principle involves heating the polymer above its melting point, extruding it through a spinneret, and solidifying during the cooling process (Figure 2.6). This method presents some advantages like continuity and high yield of the resulting fibres, making it suitable for materials like polyester, nylon, and polypropylene. Traditional melt-spun fibre diameters are influenced by various parameters. Firstly, using as precursors polymers with high molecular weight and melt viscosity result in larger fibre diameters. Secondly, the initial fibre diameter increases with the spinneret aperture. Additionally, if applying high draw ratios and spinning speeds or fast cooling rates the fibre diameter can be reduced [172]. Typically, fibres produced through melt spinning have diameters between 10 and 50 μm. Therefore, this method is limited for fabricating nanoscale fibres [171].

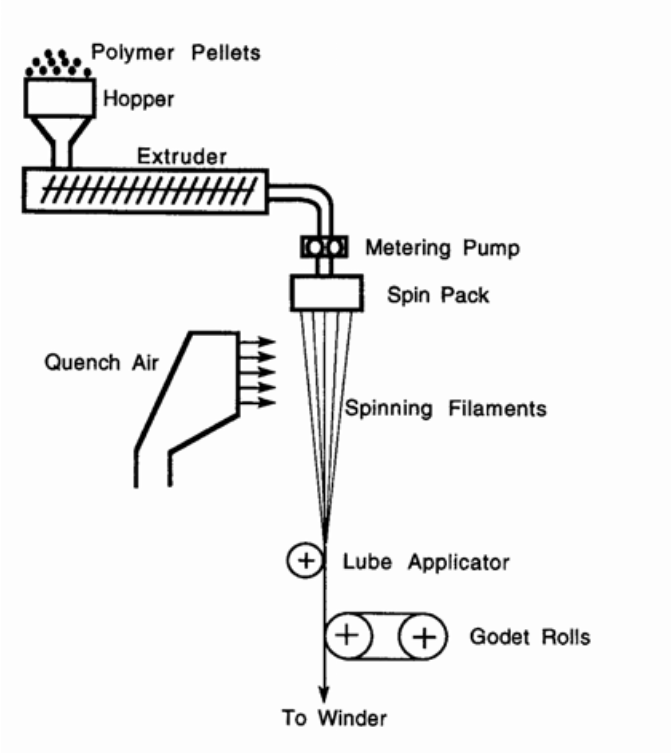

Figure 2.6. Schematic description of the melt spinning process [173]

Wet spinning technique was introduced in the early 20th century. In this method, instead heating the polymer it is first dissolved in an appropriate solvent, then extruded through a spinneret, and rapidly solidified in a coagulation bath, as illustrated in Figure 2.7. This process is advantageous for producing fibres from polymers that are not easily meltable or have a high melting point, like acrylic, viscose, and spandex. In traditional wet spinning processes, fibre diameter is influenced by various parameters. Generally, high polymers solution concentrations result in larger fibre diameters while high spinning speeds result in smaller diameters as in the previous technique. Moreover, larger spinneret apertures produce higher initial fibre diameters, while higher draw ratios yield smaller values. Additionally, the composition and temperature of the coagulation bath, which is a key difference with melt spinning process, also impact on fibre diameters, with fast coagulation typically resulting in lower value. Finally, faster solvent evaporation rates also lead to smaller fibre diameters [172]. Typically, fibres produced by wet spinning range from a few micrometres to tens of micrometres in diameter, thus also presenting challenges in producing nanoscale fibres [171].

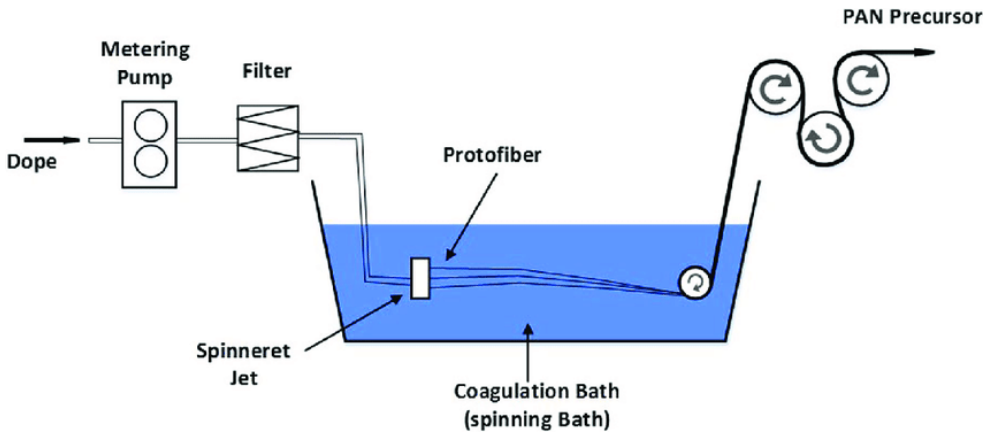

Figure 2.7. Schematic description of the wet spinning process [174]

In contrast to wet spinning, dry spinning does not employ a coagulation bath. Instead, the polymer solution evaporates naturally in air, forming the fibre. This method is distinguished by its simplicity and cost-effectiveness. However, precise control over evaporation rate and ambient conditions is paramount when fabricating nanoscale fibres [171].

Despite the distinct advantages of these traditional fibres fabrication techniques, they still exhibit significant limitations in producing nanoscale fibres. In consequence, to meet the demands of current technological and nanotechnology advancements, novel spinning techniques such as electrospinning are being extensively investigated. Electrospinning offers notable advantages, highlighting its suitability to produce nanoscale fibres, low equipment cost, simplicity of the process, and the potential for large-scale production. These benefits stand out electrospinning as crucial technique in modern fibre spinning technology.

2.5.2 Electrospinning

2.5.2.1 Origins and development

The electrospinning technology can be traced back to the 1930s. In 1934, Formhals first filed a patent related to electrospinning, describing a method of producing fibers by expelling a liquid polymer through a nozzle using high voltage [175]. Initially, the primary application of this technology was the production of textiles and filter papers.

However, it wasn't until the 1980s and 1990s, with the advent of nanotechnology, that the true potential of electrospinning was realized. Nanofibers, owing to their high surface area-to-volume ratio and unique physicochemical properties, garnered significant attention from researchers. This led to the widespread application of electrospinning in various domains [176]. For example, electrospun nanofibres found extensive application in filtration systems, sensors, energy storage devices, and as scaffolds for cells.

Entering the 21st century, with advancements in novel materials and bioactive molecules, electrospinning technology has further evolved. Nowadays researchers, by varying the type of polymer, electrospinning parameters, and adopting different post-processing techniques, can fabricate nanofibers with specific functionalities. These nanofibers have been demonstrated to have broad applications in drug delivery, tissue engineering, and wound healing [177].

In more recent years, electrospinning has experienced novel advancements as the research into the development of multi-component nanofibers [178]. By introducing two or more materials into a single fibre, nanofibers with multifunctional properties can be fabricated. Moreover, researchers are now able to fabricate three-dimensional structures using electrospinning, which opens new horizons for tissue engineering and biomedicine [179]. Intelligent nanofibers and bioactive nanofibers have also become recent research hotspots. These fibres can respond to external stimuli or can be embedded with bioactive molecules to attend specific applications [180], [181].

2.5.2.2 Principles of electrospinning

Electrospinning, in which a polymer solution is spun to obtain a fibre under a strong electric field, is an advanced fibre fabrication technique extensively utilized in the fields of nanotechnology and materials science. The main advantage of this technology lies in its remarkable flexibility and controllability, enabling the generation of nanofibers with a great variety of sizes and shapes [176]. Specifically, a standard electrospinning setup primarily comprises four key components as illustrated in Figure 2.8: a high-voltage power supply, a

syringe fitted with a pump, a needle connected to the syringe, and a grounded collector [182]. At the beginning of the electrospinning process, a specific polymer solution or melt is precisely injected into the syringe. Subsequently, a high voltage, typically ranging from 5 to 30 kV, is applied through the needle connected to the syringe, creating a strong electric field between the needle and the collector. When the electric field reaches a critical intensity, repulsive electrostatic forces overcome the surface tension of the liquid, leading to the rapid ejection of the polymer solution from the tip of the formed 'Taylor Cone" [183]. This initially ejected polymer solution undergoes a series of complex physical transformations in the subsequent μs to ms, including droplet elongation, solvent evaporation, and fibre solidification, ultimately being deposited onto the grounded collector in the form of nanoscale fibres [184]. These resultant nanofibers possess a multitude of potential applications, encompassing but not limited to biomedicine, environmental engineering, and high-performance composites. By optimising various parameters during the electrospinning process such as applied voltage, solution flow rate, needle-to-collector distance, ambient temperature and humidity, researchers and engineers can finely tune the dimensions, shapes, and properties of the final fibres. Therefore, electrospinning is not only a highly flexible and controllable technique for nanofiber fabrication but also holds the promise for further broadening its applicability across diverse fields of research through a deeper understanding of its fundamental principles and operational parameters.

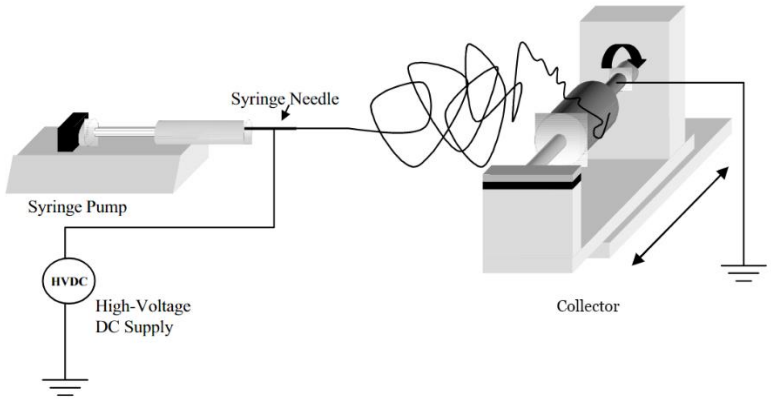

Figure 2.8. Schematic description of the electrospinning setup [185]

2.5.2.3 Optimisation and control of electrospinning parameters

As aforementioned, electrospinning is a widely utilized technique for the fabrication of nanofibres, with application in different research areas as material sciences, biomedical research, and energy storage. The optimisation and control of this technique involve a various of factors that not only influence the formation of nanofibres but also their final properties (such as morphology, diameter, and alignment) and subsequent performance.

1. Properties of polymers: the molecular structure and weight of polymers used as precursors play a pivotal role in the electrospinning process. Generally, suitable polymers should exhibit a linear molecular structure and appropriate solubility in selected solvents. Regarding the molecular weight, it needs to reach a certain threshold for electrospinning to occur. An increase in molecular weight can lead to a larger diameter of the electrospun nanofibers and also can significantly decrease the minimum spinnable concentration of the polymer solution [186].

2. Properties of solvents: a suitable solvent is crucial for the electrospinning process. A high volatilization rate of the solvent easily leads to the nozzle clogging thus impeding the success of the electrospinning process. On the other hand, a low volatilization rate of the solvent results in the adhesion of the nanofibers on the collector, or even can cause the nanofibers to re-dissolve. Moreover, the properties of the solvent affect the surface tension, viscosity, and conductivity of

the polymer solution, subsequently largely influencing the morphology of the electrospun nanofibres [187].

3. Applied Voltage: when the electrospinning device is fixed (i.e., the distance from the nozzle to the collector remains constant), the intensity of the electric field is directly proportional to the applied voltage. The charge density of the jet surface increases with the intensity of the electric field, resulting in an accelerated jet. The combination of these factors makes the jet (and the corresponding nanofibre) experience greater tensile stress and strain, resulting in a smaller diameter of the final nanofibre. However, a high applied voltage could also cause the insufficient volatilization of solvent due to the short time for jet travel from nozzle to collector [188]. Therefore, appropriate electric field strength and voltage settings are crucial for optimizing the diameter of nanofibres.

4. Flow rate: controlled by a syringe pump throughout the process, a high flow rate may lead to insufficient stretching of the nanofiber, thereby increasing its diameter. On the contrary, a low flow rate can lead to an interruption in the electrospinning process [189].

5. Distance from needle tip to collector: generally, this parameter mainly affects the strength of the electric field and, consequently, the volatility of the solvent. If the distance is too short to allow adequate solvent evaporation, the resulting nanofibers are likely to adhere to one another. On the contrary, a longer distance will result in lower electric field intensities, negatively affecting the electro-spinnability of the initial solution [190].

6. Ambient parameters (temperature and humidity): both of these experimental parameters affect the final fibre morphology due to their influence on the volatilization rate of the solvent. Additionally, an increase in temperature has been reported to significantly reduce fibre diameter, which can be attributed to the decrease in solution viscosity [191]. Moreover, multiple studies have also shown that high humidity is beneficial for the discharge of electrospun nanofibres [192].

In summary, the optimisation and control of electrospinning parameters is a complex, multifactorial issue involving various aspects such as polymer material, solvent, applied voltage, flow rate, needle tip to collector distance, and ambient parameters. These factors not only influence the appropriate formation of nanofibers but also determine their final characteristics and performance in selected application. Therefore, to obtain high-quality electrospun nanofibers, it is imperative to consider these factors comprehensively and undertake appropriate optimization and control measurements.

2.5.2.4 Rheological requirements for electrospinning

In the process of electrospinning, the rheological properties of polymer solutions play a crucial role as they directly influence the morphology and quality of the fibres. This section aims to review the impact of polymer solution conditions on electrospinning from a rheological perspective.

Early studies have shown that the concentration of the polymer solution has a significant impact on the morphology of the fibres. A higher concentration leads to an increase in fibre diameter and may impede successful spinning, whereas a lower concentration results in the formation of "bead-on-string" structures [193], [194]. This phenomenon can be explained by the degree of entanglement in polymer chains. Depending on the state of chain entanglements, the polymer solution can be classified in four different concentration regimes [195]: (1) dilute, (2) semi-dilute unentangled, (3) semi-dilute entangled and (4) concentrated (the first three solution regimes are illustrated in Figure 2.9). In dilute solutions, polymer chains are separated by solvent molecules, resulting in chains not entangled with each other. As a consequence, this type of polymer solution is not spinnable and only droplets will be formed through electrospinning [196]. When the concentration increased, polymer chains start to overlap with each other. The concentration between dilute and semi-dilute unentangled is known as the critical chain overlap concentration (C^*). Physically, the concentration inside the a single macromolecular chain is equal to the solution concentration at C^* [196]. Nevertheless, the fibres can still not be formed at this state of polymer solution due to absence of sufficient entangled

chains. Researchers suggest that a minimum concentration, known as the entanglement concentration C_e, is required for electrospinning uniform fibres. This concentration marks the transition between the semi-dilute unentangled and semi-dilute entangled regimes.

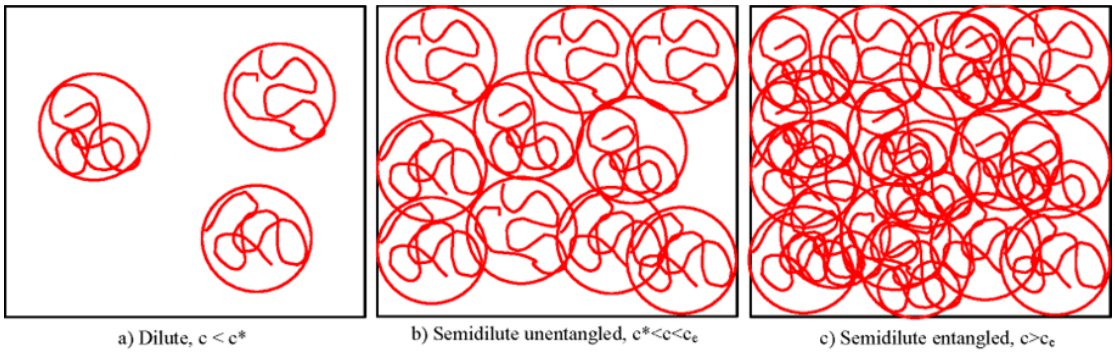

Figure 2.9. Physical representation of the three solution regimes [196]

Furthermore, the polymer solution is subjected to a certain shear force during the electrospinning process. Hence, only the viscosity value (or concentration value) is not enough to predict whether the polymer solution is spinnable or not. Therefore, a precise rheological study of polymer solution is necessary in order to understand the mechanism of fibres formation. A rheological study is used to determine the bulk viscosity (η), storage (G')/loss (G'') modulus, and complex viscosity (η^*). For example, the η is determined through rotational tests and calculated according to following equation:

$$\eta = \frac{\tau_c}{\gamma}$$

where τ_c is the shear stress and γ is the shear rate of polymer solution.

Oscillatory tests are used to determine G', G'', and η^*. G' and G'' is calculated according to following equation:

$$G' = \left(\frac{\tau_a}{\gamma_a}\right) * \cos\delta$$

$$G'' = \left(\frac{\tau_a}{\gamma_a}\right) * \sin\delta$$

where τ_a is the shear stress and γ_a is the deformation, δ is the phase shift angle (See Figure 2.10).

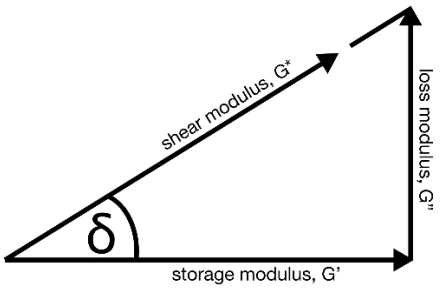

Figure 2.10. Vectorial representation of modulus

The complex shear modulus (G^*) can be determined using the values of G' and G'' based on the following formula:

$$(G^*)^2 = (G')^2 + (G'')^2$$

and the complex viscosity (η^*) can be calculated using equation below:

$$\eta^* = \frac{G^*}{\omega}$$

the frequency used in oscillatory tests is from 0.1/s to 100/s. The value of G' and G'' should collect at a very low frequency due to the most significant difference of the two value at low frequency [197].

Jian H, et.al. studied the influence of fluid elasticity on electrospinning by using Boger fluids [198]. They point out that chain entanglement is not necessary for uniform fibres formation. While fluid elasticity is an essential property to control electrospun fibres morphology. Fluid elasticity is characterized through the fluid relaxation time: if this parameter is high enough (which is in agreement with a high degree of fluid elasticity), the Rayleigh instability (which is the reason to break up jet into droplets) can be suppressed to produce fibres. However, for a successful electrospinning, the loss or viscose modulus (G'') should be larger than storage or elastic modulus (G') [199]. Specifically, G' represents the ability of materials to store energy and G'' represents the materials' ability to dissipate such energy, which is used to change

materials' structure. The polymer structure in solution will be changed into fibre morphology only when G'' is larger than G', or the jet will break up and shrink into the droplet.

From a rheological perspective, there are three properties required for polymer solutions to form uniform fibres through electrospinning: (1) Viscosity: polymer concentration should be high enough to obtain at least semi-dilute entangled solution, which is characterized by viscosity; (2) G'' of the polymer solution should be larger than G' and (3) G' cannot be too low to suppress the Rayleigh instability.

2.6 Stabilisation of carbon nanofibres

2.6.1 Principles and mechanisms of stabilisation

Biopolymers usually contain a high amount of heteroatoms in their inner structure, such as O, H, and N, thus negatively impacting on their carbon content (44.4 wt% for cellulose, 50 wt% for PLA, and 44.7 wt% for chitosan) [38], [200]. Aiming to prepare CNFs, carbonisation is an essential step leading to the removal of such atoms other than C. However, aiming to maintain the fibre morphology, stabilisation is frequently an important step to be considered before carbonisation.

As previously mentioned, the main function of stabilisation is to ensure the dimensional stability of the carbonisation process and retain the preferred axial orientation induced by the fibre during the electrospinning process [201]. With this purpose, polymer-based nanofibres are subjected to thermal treatment (200-350 ºC) in an oxidative atmosphere, such as air or oxygen, to decompose and rearrange the polymer. While the physicochemical processes involved in stabilisation are complex, two possible mechanisms are considered [202]. Firstly, oxidation reactions serve as one of the primary reactions during stabilisation, introducing different oxygen functional groups (carbonyls, ethers and carboxylic groups) into the aliphatic chains. The mechanism for oxidation involves the adsorption and dissociation of oxygen molecules, initiating oxidative reactions on the surface of the nanofibres. The rate and extent of these oxidation reactions are influenced by factors such as oxygen concentration, temperature, and

time. Secondly, cross-linking and aromatization reactions also occur, resulting in the enhancement of the mechanical and thermal stability of the nanofibers, thereby improving their overall performance and applicability.

2.6.2 Optimisation of stabilisation parameters

The parameters involved in the stabilisation step are often determined by the thermal properties of the (bio)polymer selected as precursor. Different precursors present diverse thermal characteristics. Thus, to identify the optimal parameters for stabilisation, the thermal stability of precursors is generally investigated by using, for example, a thermogravimetric analysis (TGA) instrument. As a result, a suitable stabilisation procedure can be determined after recording the weight loss and heat flow at various temperatures. Controllable parameters during stabilisation typically include heating rate, stabilisation temperature, and isothermal time.

In terms of the heating rate, a low value—usually ranging from 0.5 to 3°C/min—is preferable. Such low values are crucial in controlling the stabilisation reaction rates, including cross-linking, dehydrogenation, and cyclization processes, which are highly sensitive to temperature variations. Thus, it is ensured that these reactions are properly developed, thereby enhancing the final performance of carbon nanofibres (CNFs) [203]. Moreover, the stabilisation stage is a pivotal step before carbonisation, as a lower heating rate aids to increase the subsequent carbonisation yield and facilitates the formation of a more organized microstructure. This includes optimized crystal structures and fewer defects, essential for improving the carbon content, mechanical properties, and electrical conductivity of the final product. Rapid heating may result in excessive temperature gradients within the material, leading to internal stresses, microcracks, or uneven structures, adversely affecting the mechanical properties of resulting CNFs [204].

The stabilisation temperature is usually determined by the thermal properties of the precursor. Taking PAN-based precursors as an example, the stabilisation temperature commonly falls between 200-300°C. Within this temperature range, polyacrylonitrile (PAN) macromolecules

undergo a transformation from a linear polymer to a rigid, thermally stable ladder structure. This transformation is typically corroborated by nuclear magnetic resonance (NMR) and X-ray photoelectron spectroscopy (XPS) data [205], [206]. Both PAN homopolymers and copolymers have been extensively studied to understand their behaviour during the stabilisation process [207].

Another example is cellulose. Hydroxyl groups in the structure of cellulose readily form intra- and intermolecular hydrogen bonds, leading to various ordered crystalline arrangements. Hence, the selection of the stabilisation temperature for cellulose is crucial; high temperatures may result in excessive carbon loss, while low temperatures could lead to inadequate stabilisation of the cellulose, thereby affecting the fibre morphology during carbonisation. Nolene et al. investigated cellulose-lignin-based hybrid filaments for carbon fibre production. They indicated that temperatures closer to the precursor's degradation temperature could shorten stabilisation times, but usually at the cost of mechanical performance [208]. Thus, to prevent excessive decomposition of the precursor during stabilisation, temperatures below its degradation point or where its degradation rate is lower are often chosen for stabilisation. Once the stabilisation temperature is set, the degree of stabilisation can be controlled by adjusting the isothermal time.

2.7 Carbonisation of carbon nanofibres

Carbonisation is a critical step in the fabrication of carbon nanofibres (CNFs), typically performed in a high-temperature range, from 500 to 2000 °C [209], [210]. During this process, the heteroatoms of the polymeric precursors, such us O, H, N, etc, are removed by heat treatment under an inert atmosphere and converted into carbon materials.

The carbonisation temperature significantly influences the properties of resulting CNFs. For instance, Tao et al. investigated the impact of different carbonisation temperatures (1000, 1500, and 2000 °C) on the electrochemical performance of lignin-based CNFs in lithium-ion batteries (LIBs). They found that CNFs prepared at 1000℃ exhibited the best electrochemical

performance, showing a high specific capacity of 271.7 mA h g^{-1} at 30 mA g^{-1}. Conversely, CNFs carbonised at higher temperatures displayed a lower specific surface area and graphite-like layers, which are less conducive to lithium ion storage, leading to reduce the electrochemical performance [211]. While Lee et al. carried out a study on carbonising PAN-based CNFs at different carbonisation temperatures range between 800-950°C, followed by physical activation with H_2O, to fabricate electrodes for SCs and assessed their electrochemical performance. They found that CNFs carbonised at the higher T, possessed a greater specific surface area, which correlated with a higher specific capacitance [212]. In a study by Thamer et al., electrospun CNFs underwent surface modifications through the carbonisation process resulting in an enhanced efficiency towards adsorption of lead ions (Pb^{2+}) from aqueous solutions. This study also corroborated that main properties of CNFs, such as specific surface area, porosity, and diameter, can be controlled during the carbonisation process [213].

The carbonisation heating rate also influence the properties of CNFs. Min-A Kim et al. examined the impact of different carbonisation heating rates (range from 0.5 to 10 °C/min) on PAN-based carbon fibres. They observed that varying heating rates did not significantly alter the microstructure of CNFs, but markedly influenced their mechanical properties. showing those produced at lower heating rates an enhanced tensile strength [214]. Kuo et al. designed a specific apparatus to study the effect of carbonisation heating rates (1, 100, 1000 °C/min) on PAN-based carbon fibres. They observed that materials prepared at lower carbonisation rates exhibited more graphitic structures, whereas those processed at ultra-high carbonisation rates exhibited higher porosity and larger pores [215]. Xie et al. examined the impact of carbonisation time on PAN-based carbon fibres. They discovered that an increase in carbonisation time led to an enhanced graphitisation level and improved electrical conductivity of the fibres [216].

Therefore, the carbonisation process is a key step in the fabrication of CNFs. By carefully controlling carbonisation conditions such as temperature, heating rate, and time, various properties of CNFs can be optimised, thereby broadening their range of applications.

2.8 Activation of carbon nanofibres

The objective of the activation step is not only to develop the porous structure of carbon nanofibres (CNFs) thus enhancing the specific surface area but also to modify their surface chemistry. This dual effect significantly increases both, their adsorptive capacity and electrochemical performance by improving the double layer formation or the development of surface redox reactions. Through the activation process, micro- and mesopores are generated on the surface of the CNFs, offering additional adsorption sites and thereby enabling this activated carbon nanofibres (ACNFs) to more effectively adsorb organic or inorganic substances. Additionally, activation introduces various functional groups to the carbon surface, including hydroxyl, carboxyl, and phenolic groups [217]. These functional groups improve the hydrophilic characteristics of the ACNFs, making them more versatile for different applications. Furthermore, the presence of these groups enhances the surface reactivity, facilitating more effective interactions with adsorbates and increasing the efficiency in applications such as catalysis and SCs.

In recent years, research in the field of ACNFs has been continuously evolving and deepening, with the industrial scale also being expanded progressively. However, there is currently no consensus among researchers regarding the mechanisms of activation of CNFs. The understanding of pore structure development and how to prevent its clogging is insufficient, resulting in inconsistent quality of ACNFs, which has constrained their development and applications. This section aims to review the processes and mechanisms of various activation methods, as these processes are pivotal in influencing the performance and applications of ACNFs.

2.8.1 Methods and processes of CNFs activation

Methods related to CNFs activation, as occurs with several carbon materials, primarily fall into two major categories: physical and chemical activation procedures with ongoing in-depth research also focusing on template methods.

2.8.1.1 Physical activation

Physical activation utilises steam, carbon dioxide, air, or their mixtures as activating agents, reacting at temperatures between 750 - 1000℃ for a certain period to produce ACNFs. Physical activation generally proceeds in two steps: initial carbonisation of the raw material at around 500 °C, followed by activation at higher temperatures using steam, CO_2, or other gases. At elevated temperatures, both steam and CO_2 serve as relatively mild oxidising agents. The internal carbon atoms of the material combine with the activating agents and are expelled in the form of $CO+H_2$ or CO, thereby forming a porous structure [218]. Physical activation typically requires higher temperatures and longer activation times compared to chemical activation, resulting in greater energy consumption and higher costs. Despite these drawbacks, physical activation is still widely employed in industrial production, primarily because the resultant ACNFs require minimal post-treatment steps.

Alcaniz-Monge et al. investigated the effects of CO_2 and steam activation on pitch-based ACNFs. They found that CNFs activated with CO_2 developed more micropores, without observing significant changes in fibres diameter. In contrast, steam-ACNFs showed wider pore structures, with a marked decrease in fibres diameter. CO_2 appears to react more extensively than steam in these small pores, likely due to its larger diffusion coefficient [219]. Alcaniz-Monge et al. also observed that CO_2 and steam activation had impact on the surface chemistry of ACNFs. Compared to CO_2 activation, carbon fibres activated with steam displayed a higher concentration of oxygen-containing functional groups on their surface [220].

2.8.1.2 Chemical activation

Compared to previous procedure, chemical activation produces ACNFs with higher C yields and more developed porous structures. Moreover, the time required for chemical activation is generally shorter, and the required temperatures are not as high (ranging between 500-900 ^{o}C). However, chemical activation leaves residual activating agents, which even after washing cannot be entirely removed, limiting the application of the ACNFs. Additionally, the commonly

used activating agents pose a certain corrosive effect on the equipment, demanding higher quality standards. Consequently, current research hotspots mainly focus on overcoming these challenges.

Commonly used activating agents in the chemical route involved strong acids, strong bases, or metal salts, such as KOH, H_3PO_4, $ZnCl_2$, and K_2CO_3. During chemical activation in one single step, the raw material is primarily impregnated with the activating agent, in a certain ratio, and subsequently the mixture is subjected to a thermal treatment, with temperatures between 400 – 900 ºC. The reaction product is then washed to remove the activating agent, yielding the ACNFs. For example, Mopoung et al. activated natural pineapple leaf fibre with 85% H_3PO_4 using a 1:1 weight/volume impregnation ratio at 500°C for an hour. The resulting ACNFs achieved a BET surface area of 440 m^2/g [221]. Another activation process involves two steps: initially the raw material is carbonised, and then the resulting product is mixed with the selected activating agent for further activation. For example, Maciá-Agulló et al. mixed different activating agents (NaOH and KOH) directly with PAN-based carbon fibres and activated them at 750 °C. They observed that the reaction between NaOH and carbon was more intense, resulting in a lower development of the porosity and in lower yields in comparison with using KOH. This could be due to the ease intercalation of KOH into more crystalline carbons [222]. Liu et al. prepared electrospun PAN nanofibres and then carbonised them to obtain CNFs. These CNFs were immersed in $ZnCl_2$ solutions of varying concentrations (20, 40, 60 w/v%) before drying and subsequent activation at 500 °C. They discovered that ACNFs treated with 60 w/v% $ZnCl_2$ exhibited the largest specific surface area and the fibre network became significantly hydrophilic [223]. The impregnation ratio of the activating agent to the raw material is a crucial factor affecting the properties of the ACNFs. Therefore, the desired ACNFs can be prepared by optimising the impregnation ratio and the activation temperature.

As previously mentioned, the main goals of activation step are to increase the specific surface area of the material and to enrich its surface chemistry. Recent research has identified that functional groups containing oxygen, nitrogen, and phosphorus can enhance the

electrochemical performance of CNFs. It is widely known that oxygen-containing functional groups improve electrochemical behaviour by increasing the hydrophilicity of carbon materials (ensuring a better electrode/electrolyte contact), providing additional pseudocapacitance contribution (through the development of surface redox reactions), and enhancing ion adsorption [224].

The introduction of nitrogen functional groups significantly enhances the electrochemical properties of carbon materials through several mechanisms. Firstly, nitrogen doping enhances the electronic conductivity of carbon materials due to the electronegativity difference between nitrogen and carbon atoms [225]. Secondly, nitrogen functional groups, such as pyridinic and pyrrolic nitrogen, provide additional ion adsorption sites, strengthening the interaction between the electrode material and electrolyte ions, thereby increasing capacitance [225]. Lastly, nitrogen-doped ACNFs can also contribute additional capacitance through pseudocapacitive contribution [226].

While phosphorus-containing functional groups are less prevalent in ACNFs, recent research has proved their significant role in enhancing their electrochemical performance. Hulicova-Jurcakova et al. revealed that even a small, yet quantifiable, presence of P in the carbon matrix markedly influences the electrochemical behaviour of ACNFs [227]. The formation of phosphorus–nitrogen and phosphorus–carbon bonds, along with the decrease in bridging oxygen and the number of phosphates, increases the heterogeneity of the carbon surface. Such alterations result in the development of compounds that not only elevate the overall capacitance but also substantially improve the capacitance retention ratio.

A comprehensive understanding of mechanisms of activation is crucial for tailoring the activation process to achieve specific physicochemical properties and, hence, appropriate electrochemical performance.

As mentioned earlier, the activation agents commonly used in chemical activation are typically strong bases, strong acids, and metal salts. Among the alkaline-based activating agents, KOH

stands out as the most widely used. Current research on the preparation of ACNFs using KOH activation is quite active. This is primarily because the products prepared possess advantages such as a easily controllable porous structure and a concentrated distribution of micropores. The activation reaction temperature for KOH mainly ranges between 700-900 °C. However, the activation mechanism is rather complex, and there is currently no consensus. Jiménez et al. investigated the mechanism of KOH activation in CNFs. They noted that a heat treatment of CNFs with KOH produces hydrogen, the corresponding metal carbonate, and the metal, as a result of the reaction between the carbon and the hydroxide. The decomposition of carbonate leads to the formation of K_2O and CO_2, which are then reduced by carbon to form potassium and carbon monoxide. The reaction can be represented as follows [228]:

$$6KOH + C \rightarrow 2K + 3H_2 + 2\,K_2CO_3$$

$$K_2CO_3 \rightarrow K_2O + CO_2$$

$$K_2CO_3 + \ C \rightarrow K_2O + 2\mathrm{CO}$$

$$K_2\mathrm{O} + \mathrm{C} \rightarrow 2K + \mathrm{CO}$$

$$2K \ + \ CO_2 \rightarrow K_2O + \mathrm{CO}$$

Owing to the fact that KOH is a strong base, and as previously stated, it presents a significant corrosive effect on equipment and also contributes to considerable environmental pollution. Despite these challenges, KOH activation can produce ACNFs with high specific surface areas and uniform porosity, which play a crucial role in SCs.

$ZnCl_2$ appears as a representative of metal salt activating agents. ACNFs produced through $ZnCl_2$ activation generally do not exhibit as high specific surface areas as those prepared via KOH activation. However, the activation temperature for $ZnCl_2$ is relatively lower, usually ranging between 500-750 °C.

As for the $ZnCl_2$ activation mechanism, Pua Eng Hock et al. point out that $ZnCl_2$ is embedded into the carbon matrix at temperatures above the agent's melting point, resulting in pore

formation. The reaction between carbon atoms and the dehydrating agent is promoted within the extended interlayers of carbon [229]. Yorgun et al. suggested that the dehydration effect of $ZnCl_2$ is more pronounced at temperatures below 500 °C [230]. Liu et al. activated PAN-based CNFs at 500℃ using $ZnCl_2$ and applied them for capacitive desalination. Their results showed that $ZnCl_2$ activation enhanced the wettability and specific surface area of the ACNFs [223].

However, the volatility and toxicity of $ZnCl_2$ still pose significant environmental concerns and can adversely affect the health of operators. Additionally, $ZnCl_2$ is not easily recyclable, leading to elevated costs. Consequently, researchers are currently exploring alternative methods to address these issues.

Currently, H_3PO_4 is gaining increasing attention as activating agent due to its typically lower activation temperatures, generally ranging between 400-500 °C, and its ability to produce ACNFs with a rich mesoporous structure. Moreover, the resulting products exhibit strong acidity and contain oxygen-containing functional groups, offering advantages as potential electrodes in SCs and other applications as wastewater and waste gas treatment.

Regarding the mechanism of H_3PO_4 activation, there are also different points of view within the research community. Some researchers believe that phosphoric acid disperses within the precursor and, upon activation, is washed out, leaving pores in the carbon matrix [231]. An alternative perspective argues that the catalytic degradation of the carbon precursor by H_3PO_4 leads to its depolymerisation, which is then removed in gaseous form, leaving pores behind [232]. Yaxin Li et al. particularly studied the activation mechanism of H_3PO_4. They pointed out that, between 100-400 °C, it primarily undergoes dehydration reactions [233]:

$$nH_3PO_4 \rightarrow H_{n+2}P_nO_{3n+1} + (n-1)H_2O$$

Between 400-700 °C, $H_{n+2}P_nO_{3n+1}$ undergoes dehydration to transform into P_4O_{10}. P_4O_{10} acts as an oxidising agent and reacts with carbon to form new pores, enlarging existing pores, and generating CO_2. The reaction can be represented below:

$$H_{n+2}P_nO_{3n+1} \rightarrow P_4O_{10} + H_2O$$

$$P_4O_{10} + C \rightarrow P_4O_6 + CO_2$$

Between 700-800 °C, P_4O_{10} and/or P_4O_6 may react with CH_x to form PH_3 as well as carbon-containing gases. The reaction can be represented as follows:

$$P_4O_{10}/P_4O_6 + CH_x \rightarrow PH_3 + CO_2/CO$$

Zhi et al. incorporated 1 wt% H_3PO_4 into the spinning solution of PAN. They used electrospinning to create H_3PO_4/PAN nanofibres, which were then activated to produce PAN-based ACNFs. This in situ activation approach resulted in ACNFs with a high specific surface area of 709 m²/g. When used in SCs, these ACNFs demonstrated a high specific capacitance of 156 F/g at 0.5 A/g [234].

2.9 Literature review conclusions

In the current energy scenario, electrochemical energy storage devices have gained in interest between the scientific community. This is mainly due to their potential application in different scenarios required specific energy and power density values. For example, these systems not only allow the storage of substantial energy within a compact volume but also facilitate its rapid release, a feature particularly relevant in electrochemical devices as supercapacitors (SCs). With the maturation of technology and their extensive commercial applications, electrochemical energy storage devices have witnessed large-scale production, thereby enhancing the economic viability of renewable energy sources. However, despite their marked advantages, some of these technologies also have to address important challenges. Safety concerns have been affecting certain batteries, especially lithium-ion batteries (LIBs), which are susceptible to overheating, explosions, and fires, particularly under high loads or elevated temperatures. Moreover, even though LIBs dominate many applications, their sustainability and resource constraints remain pivotal issues. Additionally, SCs also face challenges, particularly their low energy density compared to other electrochemical storage devices. To address these issues, further research is crucial, such as developing active electrode materials

with improved characteristics. This includes exploring materials like carbon nanofibres (CNFs) or activated carbon nanofibres (ACNFs), which can enhance the performance of SCs by means of carefully optimising their morphologies and physicochemical properties.

CNFs and ACNFs, owing to their unique characteristics, such as electrical conductivity and high specific surface area, have garnered considerable attention for SCs application. However, conventional CNFs fabrication methods typically rely on petroleum-based precursors, presenting environmental and sustainability challenges. To address this, researchers have proposed the use of biopolymers, like lignin and cellulose, as precursors for CNFs. These bio-based CNFs not only exhibit superior electrochemical performance but also present a more environmentally friendly and sustainable alternative compared to their petroleum-based counterparts. Additionally, other biopolymers, such as polylactic acid (PLA) and chitosan, are viewed as potential precursors for CNFs due to their eco-friendly and renewable characteristics.

Regarding CNFs fabrication, electrospinning technology has increased in interest as an alternative approach to conventional production methods. The primary advantage of electrospinning lies on its ability to precisely control the diameter, morphology, and structure of the fibres, producing precursor-based nanofibres tailored to specific performance and application requirements. Moreover, electrospinning facilitates the production of continuous, uniform, and seamless nanofibres, with high specific surface area, appropriate mechanical properties, and conductivity.

Once fabricated the precursor nanofibers undergo three pivotal steps: stabilisation, carbonisation, and activation, to be fashioned into optimal active electrode materials (CNFs, ACNFs) for electrochemical energy storage devices. Stabilisation stands as one of the crucial steps in CNFs fabrication, providing the nanofibres with required chemical and thermal stability, ensuring that their shape and size are retained during the subsequent carbonisation process. During the carbonisation process, the heteroatoms from the biopolymeric precursor are removed, and a more defined carbon structure emerges. Activation is the final step aiming to improve some of the physicochemical properties of the previously obtained CNFs for the

subsequent enhancement of their electrochemical performance. By carefully selecting the appropriate activating agents and conditions, the specific surface area, porosity and surface chemistry of ACNFs can be tuned, enhancing their electrochemical performance and making them attractive electrode material for SCs or other electrochemical energy storage devices.

Chapter 3

Experimental methods

3. Experimental methods

This chapter encompasses all experimental procedures carried out in this study, which are divided into two main stages. In the first stage, the preparation and morphological characterisation of activated carbon nanofibres (ACNFs) were performed. This process involved four key steps, as illustrated in the schematic diagram (Figure 3.1). Firstly, biopolymer nanofibres were fabricated via electrospinning, where the polymer solution was extruded through a syringe under high voltage to form nanofibre mats. These nanofibres were then stabilised in a tube furnace with airflow to enhance thermal stability. Following stabilisation, the nanofibres underwent carbonisation in a nitrogen atmosphere within a tube furnace, resulting in carbon nanofibres (CNFs). Finally, the CNFs were chemically activated using H_3PO_4 or $ZnCl_2$, followed by washing and drying, to obtain ACNFs. In the second stage, the electrochemical performance of the ACNFs was evaluated as electrodes in aqueous supercapacitors (SCs). Detailed experimental conditions and parameters for both stages are discussed in the subsequent sections.

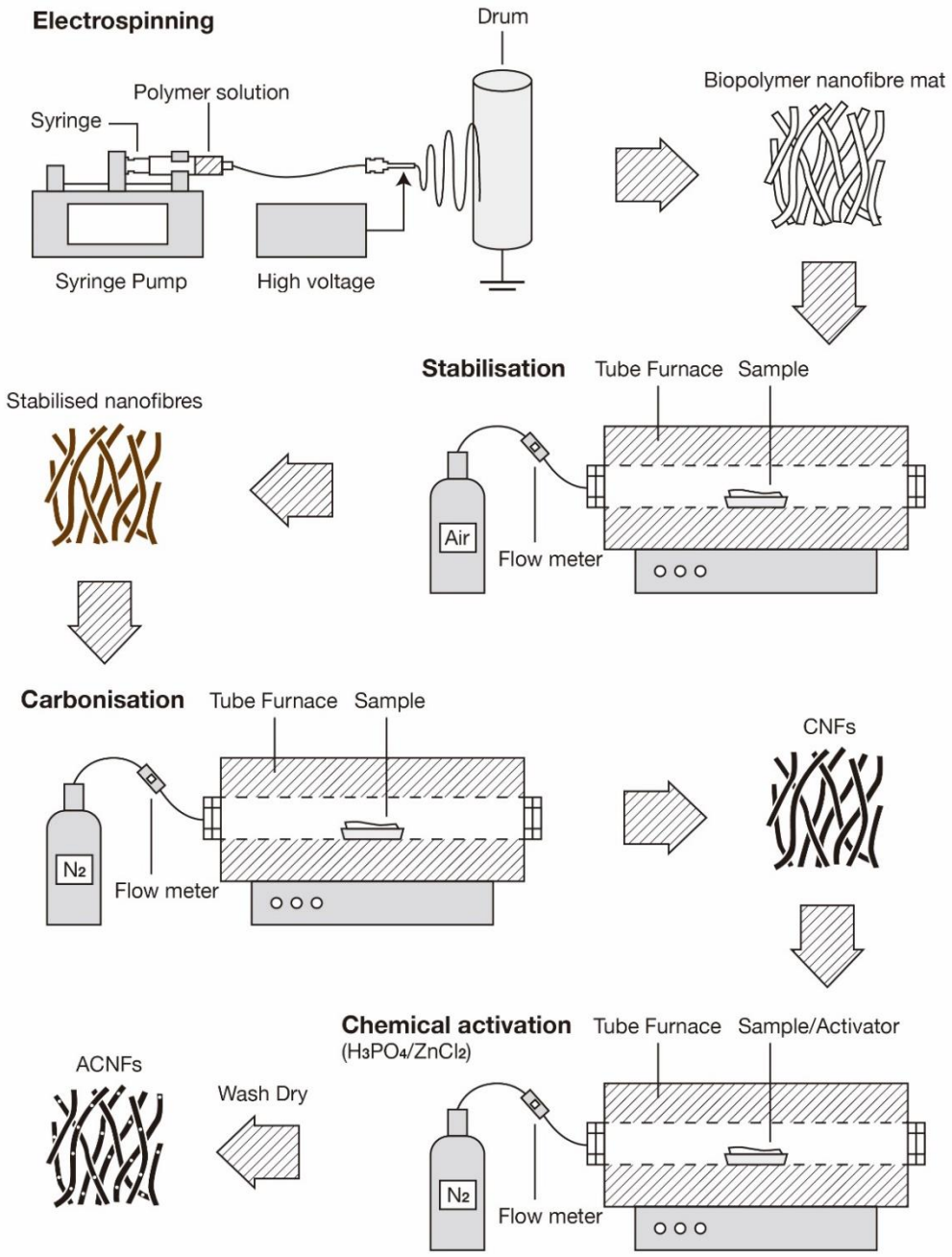

Figure 3.1. Schematic diagram of the experimental setup and processes followed: electrospinning, stabilisation, carbonisation, and activation

3.1 Preparation of biopolymeric nanofibres

3.1.1 Formulation of electrospinning solution

Three biopolymers were selected as precursors for the fabrication of carbon nanofibers: Cellulose acetate (CA), Poly(lactic acid) (PLA) and Chitosan (CTS). CA with an average molecular weight (Mn) close to 30,000 g/mol and CTS with a molecular weight (Mw) between 50,000 and 190,000 Da were sourced from Merck UK. Nature Works supplied PLA with a Mn at around 117,000 g/mol.

It is important to note that the primary reason for selecting CA for electrospinning rather than using cellulose directly is due to CA's excellent solubility in conventional solvents and ease of processing. Cellulose is a highly crystalline polymer that requires strong solvents, such as ionic liquids or specific solvent systems, to dissolve, which are typically difficult to handle and have high toxicity and cost [235]. In contrast, cellulose acetate can dissolve in more common and mild solvents such as acetic acid, acetone, or dimethylacetamide (DMAc). Additionally, nanofibres obtained by electrospinning cellulose acetate can be easily converted back to cellulose nanofibres through a simple hydrolysis process, making CA a highly versatile and practical intermediate for the preparation of cellulose-based nanofibres [236].

A range of CA solutions with varying concentrations (2, 4, 6, 8, 11, 14, 17 and 20 w/v%) were prepared in a 2:1 (v/v) blend of acetone and DMAc. The solutions were mixed at room temperature for roughly 8 hours. The binary solvent system was selected due to its suitability to provide good CA electrospinnability [237]. PLA solutions were made using the same concentrations as those for CA, but the solvent used was a 9:1 (v/v) mixture of dichloromethane (DCM) and trifluoroacetic acid (TFAA). This solvent blend was selected to improve PLA's solubility [238]. Samples were stirred at room temperature for 4 hours. CTS was dissolved in a 3:7 (v/v) mixture of DCM and TFAA. Different solutions with concentrations of 1, 2, 3, 4, 6, 8 and 10 w/v% were prepared, and they were mixed overnight at room temperature. Due to solubility challenges, the highest concentration used for CTS was 10 w/v%. The selected

polymer concentrations were chosen based on the polymers' rheological properties, which will be further explained and justified in later sections.

3.1.2 Study of the rheological behaviour of the polymer solutions

The rheology of the prepared biopolymeric solutions was assessed at 25 ºC using a TA Instruments HR-2 rheometer with a cone-plate measurement setup. The cone had a diameter of 40.0 mm, an angle of 2.0°, and a truncation gap of 60.0 μm.

Two distinct rheological evaluations were conducted: The first was a rotational test to gauge the bulk viscosity (η) of the solutions, and the second an oscillatory test to ascertain the storage (G') and loss (G'') moduli. Shear rates for the rotational test varied between 2.0 and 200 s^{-1}. For the oscillatory measurement, a 1% strain was applied, and the angular frequency (ω) ranged from 100 down to 0.1 rad s^{-1}.

3.1.3 Electrospinning set-up

The polymer-based nanofibres were fabricated at room temperature using a homemade electrospinning equipment. A syringe pump from Cole Parmer Masterflex was deployed to inject the polymeric solutions into the process at three different flow rates: 0.5, 1, and 2 mL/h. For this investigation, three types of needles with differing internal diameters (0.622, 0.933, and 1.25 mm) were utilised. The needle was linked to a high-voltage electrical supply, maintaining a steady voltage of 15 kV. The distance between the tip of the needle and the collecting surface was fixed at 15 cm. However, for the CTS solutions, the distance was reduced to 5 cm to improve the electrostatic field force and overcome the surface tension of the solution.

The electrospun nanofibres were collected on a rotating drum with a 9 cm diameter, which was clad in aluminium foil. The resultant nanofibres were subsequently collected for further characterisation.

3.1.4 Characterisation of the fabricated biopolymeric nanofibres

The structural characteristics of the electrospun nanofibres were studied by means of field emission scanning electron microscopy (FESEM, Zeiss Field Emission GeminiSEM 300) with an acceleration voltage set at 10 kV. For this purpose, nanofibres were affixed to stubs and given a gold coating with an approximate thickness of 10 nm. The diameter of the produced nanofibres was determined through image analysis software (Image-pro plus 6.0). To ensure reliability of findings, 300 measurements for each specimen were carried out. Mean diameters were taken, and the standard deviation provided.

3.2 Stabilisation of biopolymeric nanofibres

3.2.1 Stabilisation procedure

Stabilisation is an importamt step in the production of CNFs, as it enhances the thermal stability of the fibres, preventing severe shrinkage and deformation during the subsequent carbonisation process. Stabilisation typically involves subjecting polymeric nanofibres to thermal treatment in an oxidising atmosphere, such as air or oxygen. Additionally, the stabilisation step is the most time-consuming process in the production of CNFs, making its optimisation essential for significant cost reduction.

The optimised CA, PLA, and CTS polymeric nanofibres were employed as precursors for CNFs. The preparation parameters for these fibres were established based on the electrospinning results presented in chapter 4. It was decided that CA nanofibres would be made using a 17% w/v solution, with 11% w/v for PLA and 8% w/v for CTS, as these concentrations were the minimum required to obtain fibres with a smooth morphology. A flow rate of 1 mL/h was selected to balance proper solvent evaporation and significant spinning efficiency. Based on the results presented in chapter 4, higher rates are not desirable, as they might lead to the formation of ribbon-like fibres. Additionally, a medium-sized needle (0.933 mm) was chosen because smaller needles tend to cause blockages in the spinning solution, while larger needles can lead to unstable ejection of the solution, resulting in the formation of droplets [239].

PLA and CTS polymeric nanofibres required no additional processing steps and were directly stabilised. In contrast, CA fibres necessitated an initial transformation into cellulose (CELL) nanofibres before stabilisation. The conversion process for the CA nanofibres involved immersing them overnight in a 0.1 M NaOH-ethanol solution at ambient temperature. Following this, the fibres were washed thoroughly with deionised water, and the NaOH-treated CA nanofibres were subsequently dried, yielding CELL nanofibres [42].

A Lenton tube furnace, Type 3216CC, was employed for the stabilisation process. The precursor nanofibres were first exposed to air stabilisation under various conditions. A consistent heating rate of 1 °C/min was maintained, with temperatures spanning from 100 - 240 °C and isothermal durations were between 2-12 hours. The decision regarding the stabilisation temperatures was shaped by the polymer's thermal properties. The reasoning behind the particular stabilisation temperature ranges is further explained in chapter 5. In addition, the selection of stabilisation times was based on established literature where similar polymers have been reported to achieve sufficient thermal stability within this timeframe [208], [240]. The stabilisation yield was determined using the following equation, with the results presented in the section 5.2.

$$\text{Stabilisation yield (\%)} = \frac{\text{Mass of stabilised fibres (mg)}}{\text{Mass of precursor fibres (mg)}}$$

Table 3.1 offers an overview of the precursor nanofibre mats subjected to various stabilisation conditions. The following nomenclature was used: ‘S’ means stabilised fibre, followed by the precursor polymer and two numbers; the first number corresponds to the number of hours required for the isothermal treatment in the first heating step and the second one is the number of hours required for the isothermal treatment in the second heating step.

Table 3.1. The stabilisation condition of precursor nanofibres

Sample	Heating rate (°C /min)	Air flow rate (mL/min)	First heating ramp	Second heating ramp
S-CELL 1-1	1	200	Room temperature-200 °C, Isothermal time: 1 h	200 °C -240 °C, Isothermal time: 1 h
S-CELL 3-3	1	200	Room temperature-200 °C, Isothermal time: 3 h	200 °C -240 °C, Isothermal time: 3 h
S-CELL 3-6	1	200	Room temperature-200 °C, Isothermal time: 3 h	200 °C -240 °C, Isothermal time: 6 h
S-CELL 6-3	1	200	Room temperature-200 °C, Isothermal time: 6 h	200 °C -240 °C, Isothermal time: 3 h
S-PLA 1-1	1	200	Room temperature-120 °C, Isothermal time: 1 h	120 °C -140 °C, Isothermal time: 1 h
S-PLA 3-3	1	200	Room temperature-120 °C, Isothermal time: 3 h	120 °C -140 °C, Isothermal time: 3 h
S-PLA 3-6	1	200	Room temperature-120 °C, Isothermal time: 3 h	120 °C -140 °C, Isothermal time: 6 h
S-PLA 6-3	1	200	Room temperature-120 °C, Isothermal time: 6 h	120 °C -140 °C, Isothermal time: 3 h
S-CTS 1-1	1	200	Room temperature-100 °C, Isothermal time: 1 h	100 °C -230 °C, Isothermal time: 1 h
S-CTS 3-3	1	200	Room temperature-100 °C, Isothermal time: 3 h	100 °C -230 °C, Isothermal time: 3 h
S-CTS 3-6	1	200	Room temperature-100 °C, Isothermal time: 3 h	100 °C -230 °C, Isothermal time: 6 h
S-CTS 6-3	1	200	Room temperature-100 °C, Isothermal time: 6 h	100 °C -230 °C, Isothermal time: 3 h

3.2.2 Characterisation of stabilised nanofibres

FESEM was employed to examine the structural characteristics of the stabilised nanofibres. The operational parameters for FESEM, along with the procedures for sample preparation and the methodology for analysis and computation, were consistent with those detailed in section 3.1.4.

Thermal stability of the precursor nanofibres was studied using a thermal gravimetric analysis instrument (TGA, TA Q550) from ambient temperature to 500 °C at a heating gradient of 10 °C/min in an air environment. Additionally, the TGA was employed to evaluate the thermal properties of various stabilised nanofibres in a nitrogen atmosphere, from room temperature to

700 °C, at the same heating rate. Differential scanning calorimetry (DSC 2010, TA Instruments) was utilised to ascertain the melting point of PLA nanofibres.

To investigate the chemical changes during the stabilisation phase, Fourier-transform infrared spectroscopy (FT-IR, Bruker VERTEX 70) was utilised. The designated scan range for the FT-IR assessment ranged from 4000 to 650 cm^{-1}, with a consistent scan frequency of 32 times and a resolution of 1 cm^{-1}.

3.3 Carbonisation of biopolymer-based nanofibres and their activation

3.3.1 Carbonisation of stabilised polymeric nanofibres

Based on the stabilisation results presented in Chapter 5, a range of stabilised nanofibres was selected for carbonisation. The selected samples were chosen to represent different stabilisation conditions and their potential impact on the carbonisation process. For comparison purposes, non-stabilised nanofibres were also subjected to carbonisation.

All carbonisations were conducted in a Lenton tube furnace, Type 3216CC, under a nitrogen atmosphere. They began at room temperature, ramped up to 700°C at 5°C/min, and then held isothermally for one hour. The 700°C temperature was selected to maintain a relatively high carbon yield while also preventing the excessive loss of functional groups, such as oxygen and nitrogen-containing functional groups, that may have positively influenced the electrochemical performance. The carbonisation yield and the total carbon yield were calculated using the following two equations, with the results presented in section 6.1.

$$\text{Carbonisation yield } (\%) = \frac{\text{Mass of carbonised fibres (mg)}}{\text{Mass of stabilised fibres (mg)}} * 100$$

$$\text{Total carbon yield } (\%) = \text{Stabilisation yeild} * \text{Carbonisation yeild} * 100$$

In the nomenclature used, ‘C’ means ‘carbonised’, and the numbers refer to stabilisation; a lack of numbers implies that samples were directly carbonised without stabilisation.

3.3.2 Activation of carbonised nanofibres

The primary goal of the activation process was to increase the specific surface area of the CNFs and adjust their surface chemistry. H_3PO_4 and $ZnCl_2$ were selected as activating agents because they are relatively mild. This choice aimed to keep the CNFs' morphology intact while allowing for necessary changes to their surface chemistry.

H_3PO_4 was sourced from Alfa Aesar (phosphoric acid, 85% w/w aq. soln.), and $ZnCl_2$ particles were purchased from Thermo Scientific (anhydrous, 99.95%). All chemical reagents used in this study were of analytical grade and were used as received, without any further purification. As mentioned in literature review, the impregnation ratio (the weight ratio of CNFs to activating agent) plays a crucial role in the activation process. Consequently, various weight ratios were selected. Specifically, the weight ratios for both H_3PO_4 activation and $ZnCl_2$ activation were set at 1:3, and 1:4. The rationale for selecting these specific ratios was to ensure sufficient contact between the activating agents and the CNFs, thereby facilitating thorough activation.

In the H_3PO_4 activation process, the initial step involved diluting the activating solutions. This dilution was undertaken to ensure that there was sufficient volume of the activating agent solution to allow for its uniform distribution across the CNF network. Hence, an 85 w/w% H_3PO_4 solution was diluted to 10 w/v%. In addition, for $ZnCl_2$ activation, a 10 w/v% solution was prepared by dissolving $ZnCl_2$ directly into the DI water.

The CNFs mats were then immersed in the respective activating solutions. Afterwards, they were placed in an oven at 105°C overnight to remove excess water. Subsequently, the dried CNFs mats underwent thermal treatment in a tube furnace (Lenton, Type 3216CC) under a nitrogen atmosphere, at 5°C/min up to 500°C, with an isothermal holding period of one hour.

After the thermal treatment, the activated fibres were washed. The samples activated with H_3PO_4 were first neutralised with a 0.05 M NaOH solution, followed by at least five washes with hot distilled water until the pH reached neutrality. Fibres activated with $ZnCl_2$, were soaked in 1 M HCl overnight, rinsed with fresh 1 M HCl, and then washed at least five times

with hot, distilled water until the pH was neutral. The washed samples were then dried in an oven at 105 °C for subsequent experiments.

The nomenclature used for the activated fibres was as follows: 'A' indicates activation, and the subsequent part of the sample name indicates the activating agent and its proportion. For example, 'A-CELL H_3PO_4 1-3' refers to CELL-based CNFs activated with H_3PO_4 in a 1:3 weight ratio.

3.3.3 Characterisation of carbonised and activated carbon nanofibres

The structural characteristics of the nanofibers were examined using field emission scanning electron microscopy (FESEM, Zeiss Field Emission GeminiSEM 300), set at an acceleration voltage of 10 kV.

Surface area and porosity characteristics were analysed using Micromeritics ASAP 2020. The textural characterisation of the materials was conducted through the physical adsorption of N_2 at 77 K. The Brunauer-Emmett-Teller (BET) equation was applied to the N_2 adsorption isotherms to calculate the apparent BET surface area [241]. The pore volume of the materials was calculated using the Dubinin-Radushkevich equation [242].

X-ray photoelectron spectroscopy (XPS) was employed to characterise the surface chemistry of the samples. The analysis was performed using a VG-Microtech Multilab 3000 spectrometer (SPECS, Germany), which was equipped with a hemispherical electron analyzer and an MgKα X-ray source ($h\upsilon$ = 1253.6 eV). Wide spectra, covering a binding energy range of 0–1300 eV, served as a fundamental tool for identifying all the major elements present on the sample surfaces and provided the basis for calculating the elemental composition ratios. The types of bonds and functionalities within the samples were estimated by performing curve fitting to the corresponding spectra (including C1s and N1s) after executing Shirley background correction, using a Gaussian-Lorentzian peak shape with the XPS Peakfit software [243]. When curve fitting was applied to the C1s peak, five distinct peaks emerged, corresponding to graphitic C (binding energy, BE ≈ 284.4 eV), C-O epoxy/CO-H (BE ≈ 285.6 eV), C = O carbonyl

(binding energy (BE) ≈ 286.9 eV), the COOH carboxyl group (288.9 eV), and the π-π* shake-up signal typical of sp2 hybridized carbon (290.8 eV). Notably, at these binding energies, overlaps between oxygen and nitrogen functionalities were observed, particularly between C(epoxy) and C = N, and between CO and C-N [244]. The N1s peak was also subjected to curve fitting, revealing five distinct peaks. These peaks were assigned to nitrogen structures as follows: N6, indicative of pyridine-like structures, with a BE around 398.2 eV; N5, representative of pyrrolic N and amine moieties, with a BE approximately at 400.0 eV; NQ, denoting quaternary nitrogen, with a BE spanning 400.7 – 401.2 eV; and a peak occurring around 405 to 402 eV, attributed to nitrogen oxides such as Pyridine N-Oxide or inorganic nitrogen (N–X) [223], [245].

The wettability of the samples was assessed through an automatic video optical contact angle instrument (OCA-50, Data Physics Instruments, Germany). Each specimen was positioned on the stage, and a 20 μL droplet of distilled water was applied at three points on its surface. The average contact angle was subsequently calculated based on these measurements.

3.4 Electrochemical characterisation of CNFs and ACNFs as electrodes in supercapacitors

3.4.1 Fabrication of electrodes

The previously carbonised and activated CTS samples were used as active electrode materials for SCs. However, the A-CELL series, due to insufficient mechanical strength and lack of handling, could not be used as suitable freestanding electrodes and was therefore discarded for its electrochemical characterisation. The reasons for these limitations are detailed in Chapter 5.

3.4.2 Experimental setup and electrochemical techniques

All electrochemical measurements were performed using a Biologic VMP-3e Potentiostat/Galvanostat at room temperature.

The electrochemical behaviour of the different active materials under evaluation was investigated using a 'T-type' Swagelok® cell in a three-electrode configuration (Figure 3.2). The cell consisted of disk-shaped CNFs or ACNFs pieces as working electrodes (WEs), which were directly cut from the corresponding mats using a circular punch without the addition of any binders. Each WE featured a uniform diameter of 13 mm. The mass of the WEs varied depending on the specific sample, ranging from 3–5 mg. In addition, a Ag/AgCl/3.5 M and a commercial activated carbon (AC = Norit, $S_{BET} \approx 1000$ m^2/g) were used as reference (RE) and counter (CE) electrodes, respectively. The disk-shaped AC electrode (with a diameter of 13 mm) was prepared by mixing 90 wt.% of Norit and 10 wt.% of polytetrafluoroethylene (PTFE) as a binder, with the total mass of the CE amounting to approximately 15 mg. Solutions of 1.0 M H_2SO_4 were used as electrolyte, and glass fibre mats were used as separator.

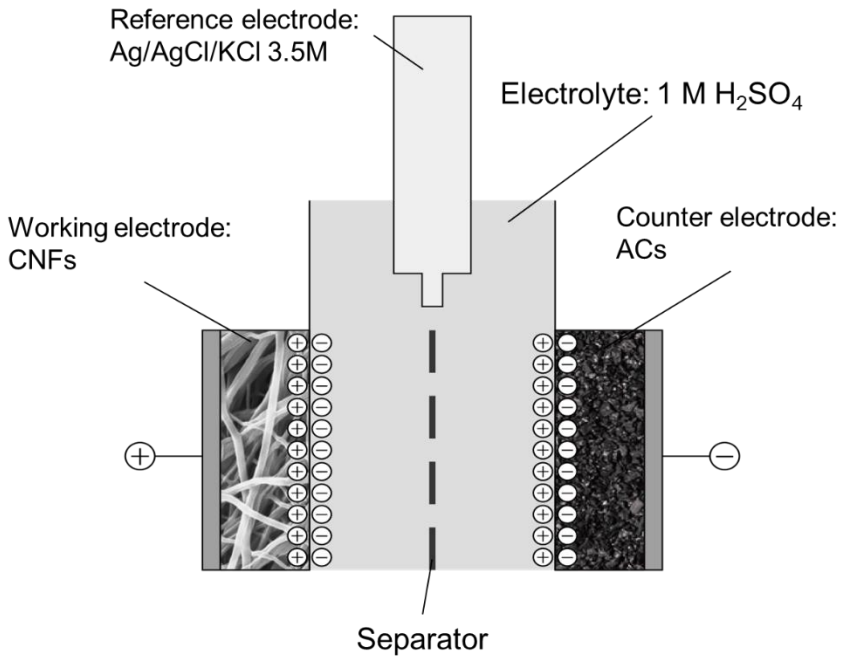

Figure 3.2. Scheme of three-electrode cell experimental setup

Initially, CV experiments were carried out at increasing scan rates (v_{scan}) of 5, 10, 20, 50, and 100 mV/s within a potential window of 0 to 0.8 V to carry out a first screening of the

electrochemical behaviour of the active materials under evaluation as electrodes in SCs. Subsequently, galvanostatic cycling with potential limitation (GCPL) measurements were performed at applied current densities of 0.4, 1, 2, 5, 10, and 20 A/g within the same potential window to analyse their charge/discharge behaviour. Additionally, the long-term stability of the materials was evaluated by galvanostatic cycling at an applied current density of 1 A/g up to 2000 cycles. The specific capacitance values of the different WEs were determined by integrating the discharge branches according to the following equation:

$$C = \frac{2 * I * \int V_{discharge} dt}{m * V_{discharge}^2}$$

In addition, another interesting electrochemical parameter, the equivalent series resistance (ESR) of the corresponding WEs, was determined from the initial ohmic drop observed at the onset of the discharge process using the equation.

$$ESR = \frac{V_{max} - V_{discharge}}{I}$$

In both equations, I represents the applied current, V_{max} is the maximum potential reached during the charge step (in this case, 0.8 V), and $V_{discharge}$ refers to the potential immediately after the IR drop during the discharge. m refers to the total mass of each WE (3–5 mg), and dt is the discharge time.

Chapter 4

Preparation of biopolymeric nanofibres: Results and discussion

4. Preparation of biopolymeric nanofibres: Results and discussion

4.1 Rheological behaviour of the biopolymeric solutions

The rheological properties of a polymer solution dictate whether the solution has the potential to form fibres by electrospinning. Therefore, the rheological results are key to determine the most suitable concentrations for subsequent electrospinning experiments.

Figure 4.1 shows the correlation between the concentration of biopolymer solutions and the respective bulk viscosity values. The viscosity readings were gathered at a minimal shear rate of 2 s^{-1}, ensuring limited system load interference. As depicted in Figure 4.1 (A), the specific viscosity for CA solutions, denoted as η^{sp}, is approximated as $\eta^{sp} \sim C^{1.5}$ for concentrations below 11 w/v%, and $\eta^{sp} \sim C^{4.8}$ for concentrations above this limit. This notable shift in the slope is attributed to the transition from semi-dilute unentangled to semi-dilute entangled regimes. The critical entanglement concentration, denoted as C_e (approximately 11 w/v% for CA), represents the concentration at which the slope alteration occurs, suggesting that electrospun CA fibres can be produced at polymer concentrations exceeding this value [196]. Consequently, subsequent electrospinning trials were conducted at CA concentrations of 11, 14, 17, and 20 w/v%.

The C_e for the PLA solutions is similarly determined and estimated to be at around 6 w/v%, as illustrated in Figure 4.1 (B). Conversely, for CTS it is found to be lower, approximately 3 w/v%, as shown in Figure 4.1 (C). These crucial values are imperative to guarantee adequate chain entanglement within the solution. Hence, the PLA solutions for the electrospinning experiments were prepared at 6, 8, 11, 14 w/v%, and for CTS the concentrations were 3, 4, 6. 8 w/v%.

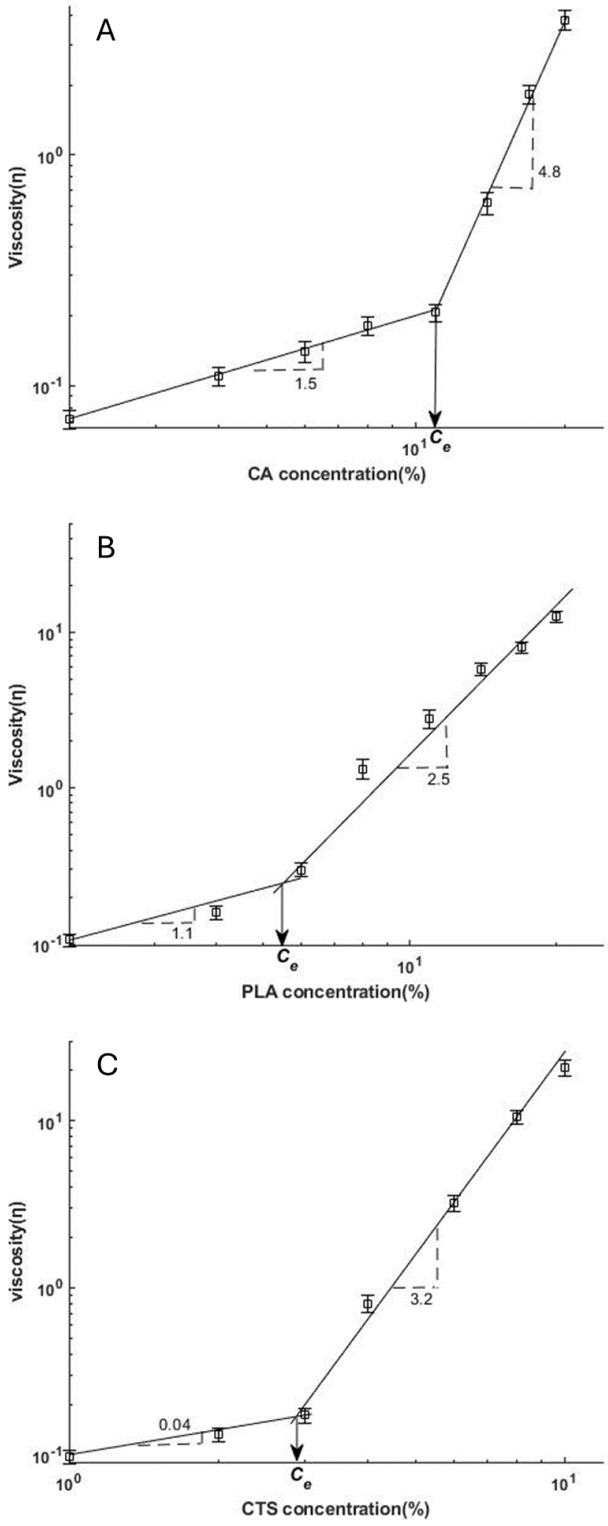

Figure 4.1 Dependence of solution viscosity on biopolymer concentration

Figure 4.2 (A) presents the results of the rotational tests conducted on the chosen biopolymer solutions. The shear-thinning effect is evident across all samples, as indicated by the decrease

in viscosity values with an increasing shear rate. Upon the application of shear force to the solution, the molecular orientation tends to align parallel to the direction of shear. This alignment causes the molecules to extend, thereby reducing their flow resistance and consequently leading to a reduction in the bulk viscosity [199]. This phenomenon demonstrates the non-Newtonian nature of the examined solutions.

During electrospinning, the solution is subjected to shear forces, requiring the bulk viscosity to reach a specific value for effective spinning. However, it is essential to note that bulk viscosity alone does not determine the success of the electrospinning process.

Figure 4.2 (B) shows the results of the oscillatory tests for the analysed polymer solutions. The storage (or elastic) modulus (G') and the loss (or viscous) modulus (G'') are pivotal in ascertaining a polymer solution's propensity for either energy retention or dispersion, respectively. For the CA and PLA solutions, it is observed that the value of G'' consistently surpasses that of G', indicating that the energy within the jet will be dissipated. This releasing of energy is critical, as it facilitates the alteration of the material structure and contributes to the shaping of the fibre [199]. High elastic force would increase the tendency of the jet to contract, preventing its initiation and elongation. Hence, elasticity has to be as low as possible but still present to allow jet initiation [199].

At lower concentrations (3 and 4 w/v%), CTS exhibits a behaviour akin to that of CA and PLA, with G'' exceeding G'. This observation is attributed to the samples remaining in a liquid state, resulting in the predominance of viscous properties. Nonetheless, with an increase in frequency, there is a more pronounced rise in G', suggesting a shift towards dominant elastic properties. This shift culminates in a crossover point between G' and G''. The inverse of frequency at the crossover point of G' and G'' yields the gelation time [246], so a three-dimensional solid network containing liquid trapped in the interstices is formed [246]. Augmenting CTS concentration from 6 to 8 w/v% is accompanied by a shifting in the crossover frequency towards lower values, which indicates an increase of the gelation time.

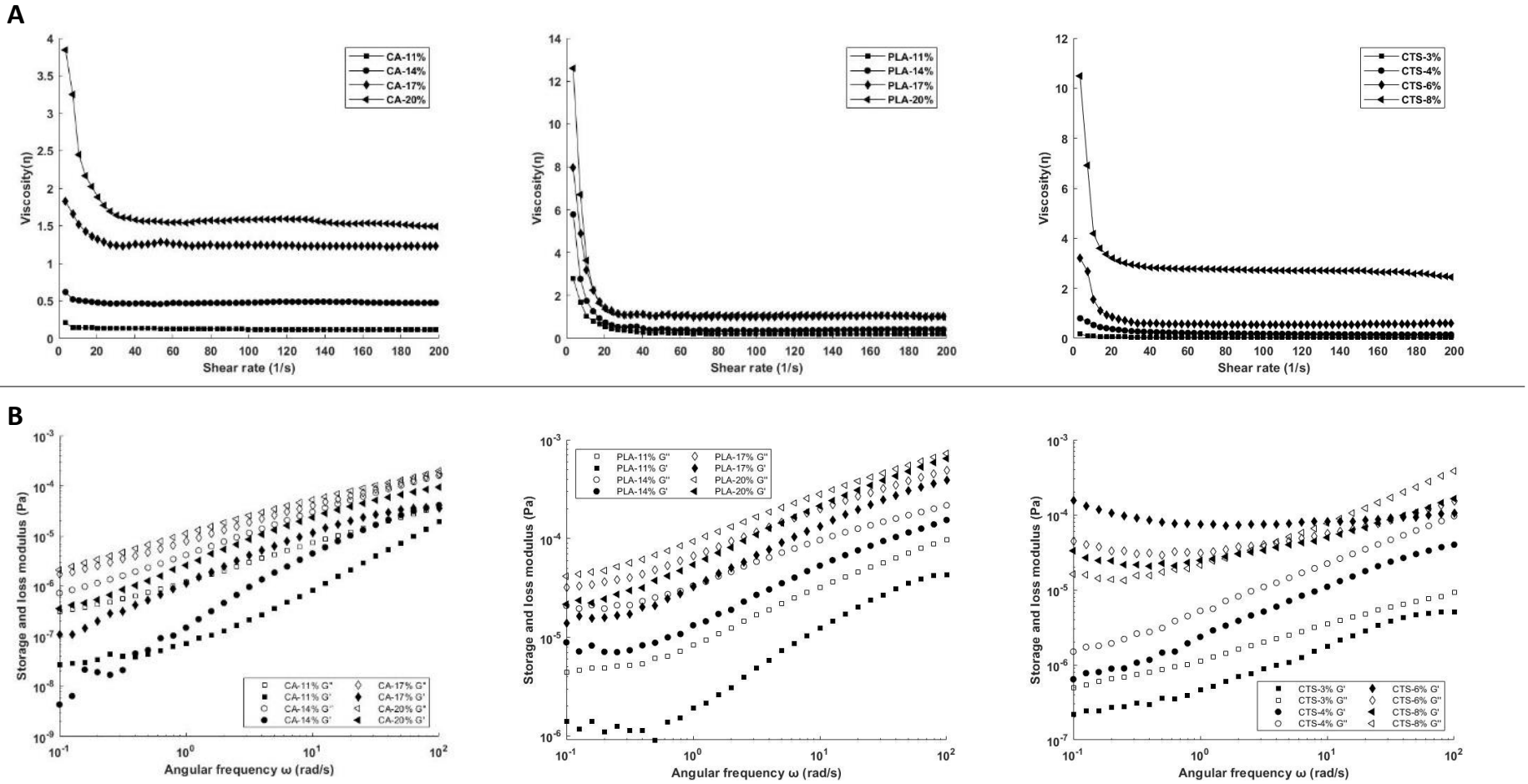

Figure 4.2 (A) Rheological results of viscosity vs shear rate; (B) Storage (G') and loss (G") modulus vs angular frequency for the three biopolymers under study

4.2 Effect of electrospinning experimental parameters on the morphology and diameter of the electrospun biopolymeric nanofibres

Following the determination of the appropriate concentration range for each polymer, the related electrospinning experiments were conducted employing the apparatus outlined in the experimental section. As previously stated, numerous variables may affect the outcome of the electrospinning attempts and the structure of the resulting nanofibres. Key variables include biopolymer concentration, flow rate, and needle dimension. Consequently, a systematic study of the effect of these experimental parameters was undertaken and is summarised in Table A.1.

4.2.1 Effect of solution's concentration

The success of the electrospinning process significantly depends on the biopolymers' concentration. At concentrations equivalent to C_e for CA (11 w/v%) and PLA (6 w/v%), large beads are formed (Figure 4.3). At its specific C_e (3 w/v%), CTS cannot be electrospun due to its very low viscosity (see Figure 4.2 (A)), resulting only in the collection of droplets. Previously acquired rheological data suggests that concentrations equal to C_e denote the shift from semi-dilute unentangled to semi-dilute entangled regimes. Nonetheless, for the selected biopolymers, such concentrations are insufficient for acquiring the desirable defect-free nanofibres.

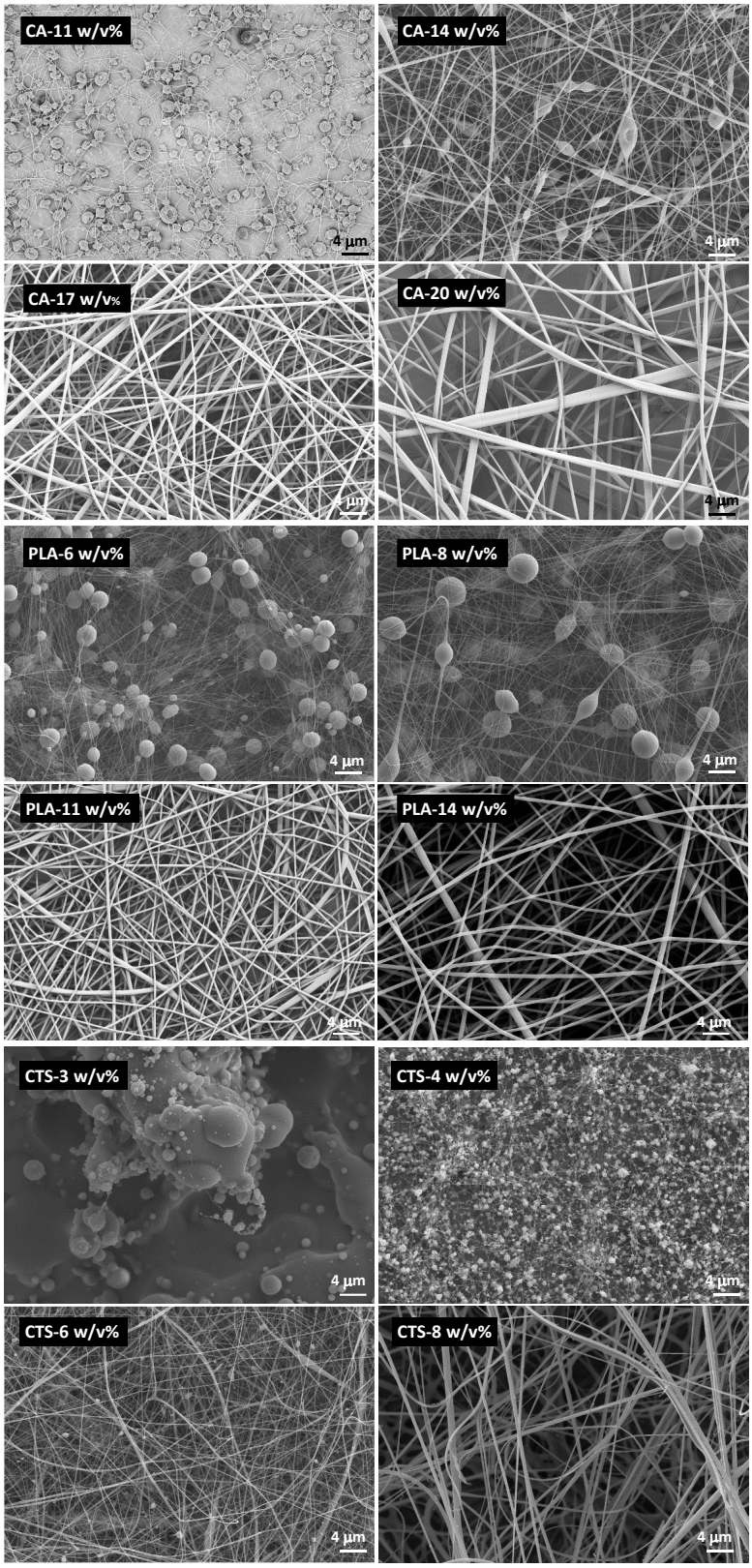

Figure 4.3 FESEM micrographs of electrospun nanofibres at different biopolymer concentrations. Flow rate 1mL/h; Needle size 0.933 mm

As the concentration of CA increases to 14 w/v%, the formation of 'beads on string' fibres is observed. This phenomenon is attributed to the insufficient chain entanglements within the solution [195].

In the case of PLA, an increase in concentration from 6 to 8 w/v% does not result in a markedly significant difference. However, it is noteworthy that at 8 w/v%, a transformation is observed in some of the beads, evolving from spherical to spindle-shaped A concentration augmentation for CTS to 4 w/v% fails to supply enough entanglement within the solution, leading predominantly to bead formation (Figure 4.3).

Based on the images presented in Figure 4.3, beadless fibres are produced at biopolymer concentrations equal to or exceeding 17, 11, and 8 w/v% for CA, PLA, and CTS, respectively. The successful electrospinning of these solutions at those concentrations is attributed to the interplay between surface tension and viscosity of the respective solutions. A raise in polymer concentration leads to an increase in viscosity, as established in the previously presented rheological characterisation, thereby enhancing chain entanglements. This results in a more pronounced viscoelastic force, effectively counteracting the Coulombic stretching force, and thus yielding nanofibres with reduced or no bead formation [247], [248].

The diameter of the resultant polymeric nanofibers is significantly influenced by the biopolymer concentration. Higher concentrations yield larger nanofibres, typically accompanied by an increased dispersion in diameter values, as presented in Figure 4.4. An increment in CA concentration from 17 to 20 w/v% results in the production of nanofibres approximately twice the diameter (for example, at a flow rate of 1 mL/h and using a 0.933 mm needle, dimensions increase from 332 nm to 647 nm), whereas for PLA the nanofibre diameters augment by a factor of roughly 1.5 (322 nm at 11 w/v% compared to 478 nm at 14 w/v% (Table A.1)). The formation of thicker fibres with more concentrated solutions can be ascribed to the enhanced cohesive forces among polymer chains and increased viscosity, leading to more entangled chains [249].

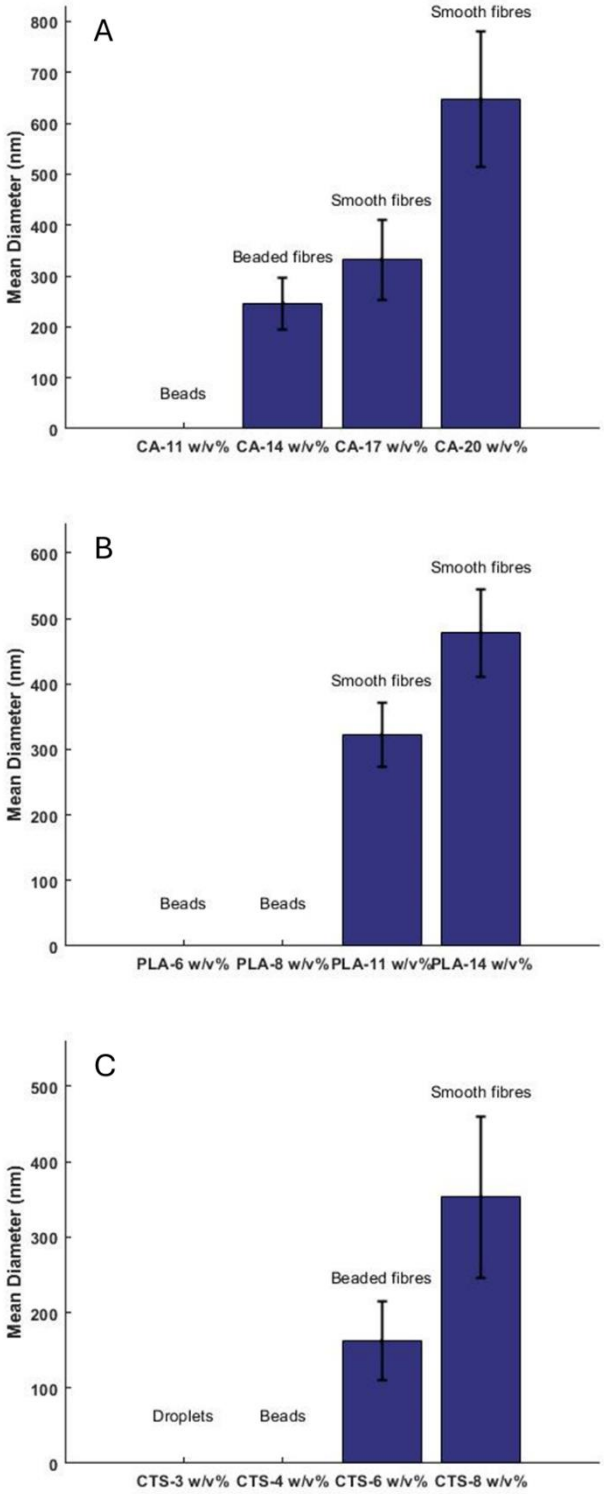

Figure 4.4 Mean diameter and morphology of electrospun nanofibres at different concentrations: (A) CA, (B) PLA, (C) CTS. Flow rate 1mL/h; Needle size 0.933 mm

Efforts were made to further increase the concentration of CTS beyond 8 w/v%, but this proved unfeasible as a gel formed at higher concentrations, hindering collection. It is noteworthy that CTS possesses limited solubility, an ionic character, and a three-dimensional network attributable to hydrogen bonding [250], therefore it is very challenging to electrospin it into fibrous structures. To address these challenges, CTS is typically combined with other synthetic polymers, such as PEO [250]. Nevertheless, pure CTS polymeric nanofibres were successfully fabricated in the current work, albeit within a rather narrow range of conditions.

4.2.2 Effect of flow rate

The flow rate influences the morphology of the polymeric nanofibres. At higher flow rates, particularly at 2 mL/h, the presence of ribbon-like structures is noted in the samples. Figure 4.5 displays micrographs of the biopolymeric nanofibres produced at three different flow rates from CA at 17% w/v, PLA at 11% w/v, and CTS at 8% w/v. These specific concentrations were selected as they are the minimum required to obtain smooth nanofibres, as detailed in section 4.2.1. A needle with a 0.933 mm diameter was employed for this comparison due to its intermediate size, ensuring a balanced comparison. However, similar trends are observed with other polymer concentrations or needle sizes. The emergence of ribbon fibres at higher flow rates is attributed to insufficient solvent evaporation and minimal stretching of the solution between the needle and the collector [251], [252]. Hence, reduced flow rates are generally preferred in electrospinning to ensure adequate solvent evaporation [253].

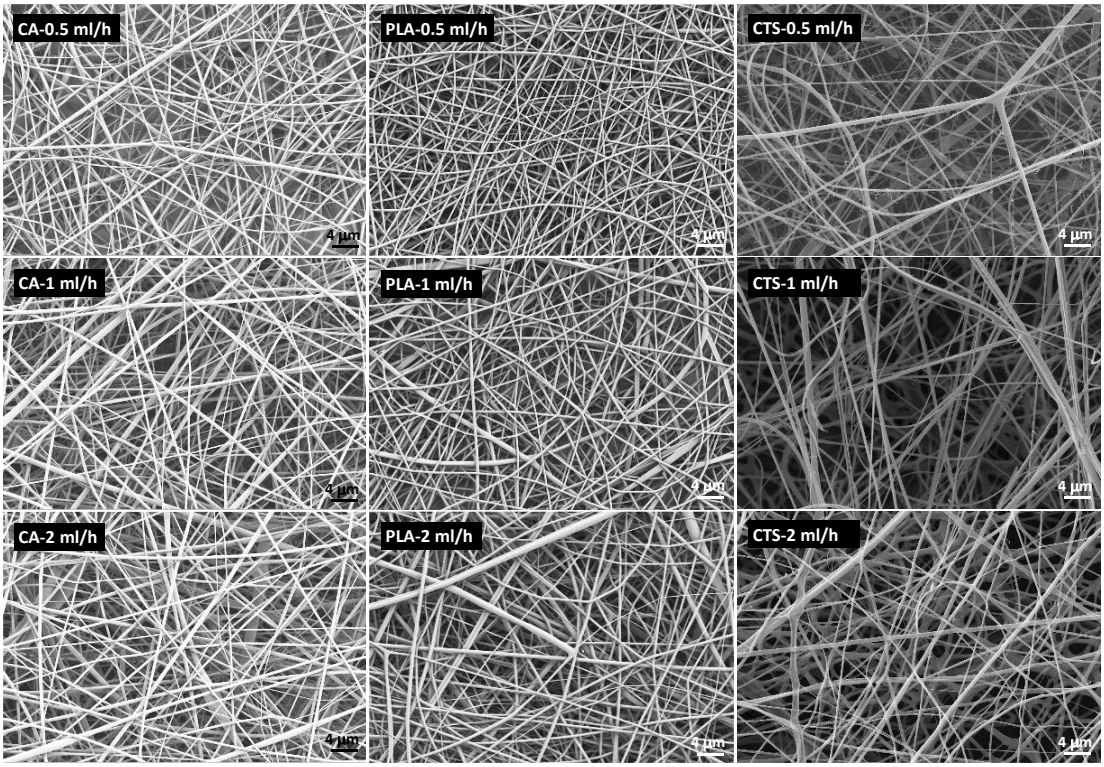

Figure 4.5 FESEM micrographs of the electrospun nanofibres at different flow rates. Needle size 0.933 mm. Concentrations: 17 w/v% CA, 11 w/v% PLA and 8 w/v% CTS

In addition to morphology, the flow rate also affects the fibre diameter. An increase in flow rate consistently results in the formation of fibres with larger diameters, irrespective of the polymer type, concentration, or needle size, as detailed in Figure 4.6. At higher flow rates, a greater quantity of polymer is extruded from the needle tip, leading to increased surface tension and consequently, fibres with greater thickness [254].

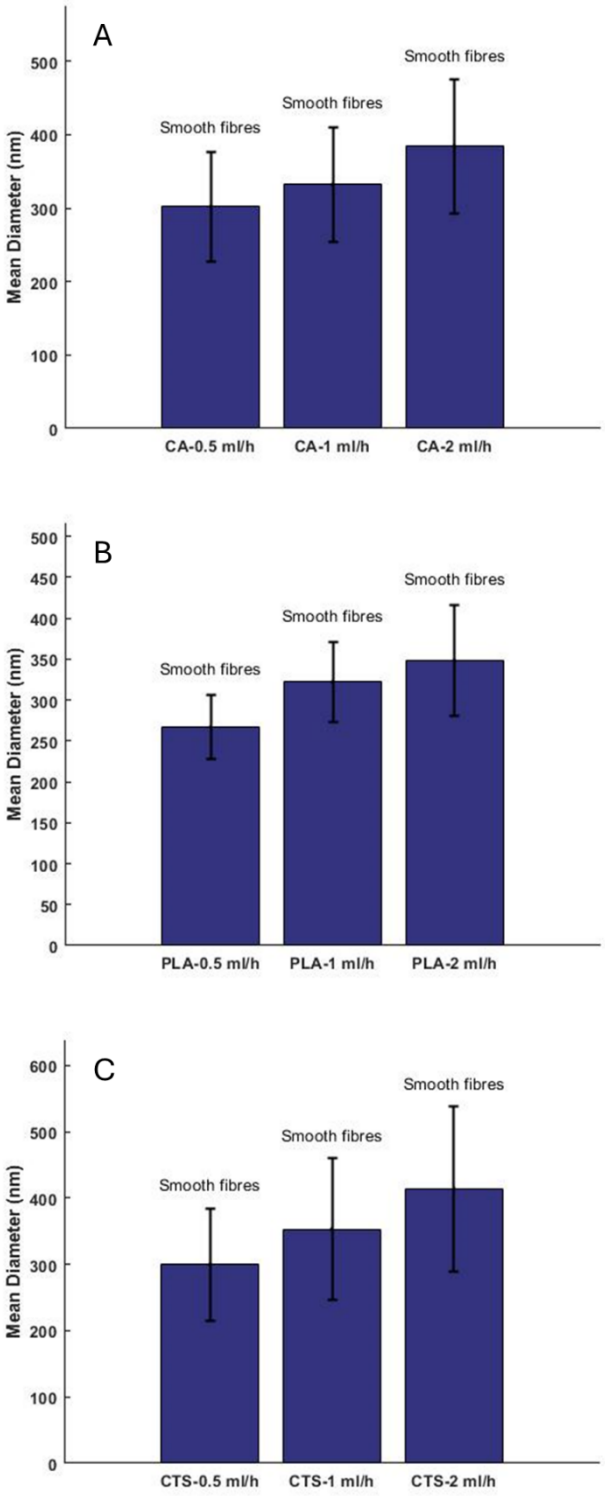

Figure 4.6 Mean diameter and morphology of electrospun nanofibres at different flow rate: (A) CA, (B) PLA, (C) CTS. Needle size 0.933 mm. Concentrations: 17 w/v% CA, 11 w/v% PLA and 8 w/v% CTS

4.2.3 Effect of needle size

Based on the data summarised in Table A.1, it appears that the needle size does not exert a significant influence on either the mean diameter or the morphology of the biopolymeric nanofibres (Figure 4.7 and Figure 4.8). For instance, CA nanofibres prepared with a 17 w/v% solution at 1 mL/h exhibit an average diameter of 321, 332, and 364 nm when employing needles with dimensions of 0.622, 0.933, and 1.25 mm respectively. A similar tendency is perceived for the other two polymers. At 1 mL/h, an 11 w/v% PLA solution yields nanofibres with mean diameters of 312, 322, and 309 nm using the three different needle sizes, and 351, 353, and 360 nm for CTS at 8 w/v%. This is in agreement with earlier reported outcomes on the electrospinning of petroleum-derived polymers, wherein no associations were identified between the needle's internal dimension and the resultant average nanofibres' diameter [255].

During the electrospinning process, the solution is expelled from the needle, creating a jet that then splits, elongates, and extends. In this procedure, jet formation holds only an indirect relation to the size of the needle. Considering that the needle size is not of critical importance, the selection of a larger needle is more practical as it reduces the likelihood of clogging and generates lower backpressure [256], particularly beneficial for high-concentration viscous polymer solutions. While larger needles can cause the solution to be ejected unevenly, leading to the creation of droplets [239].

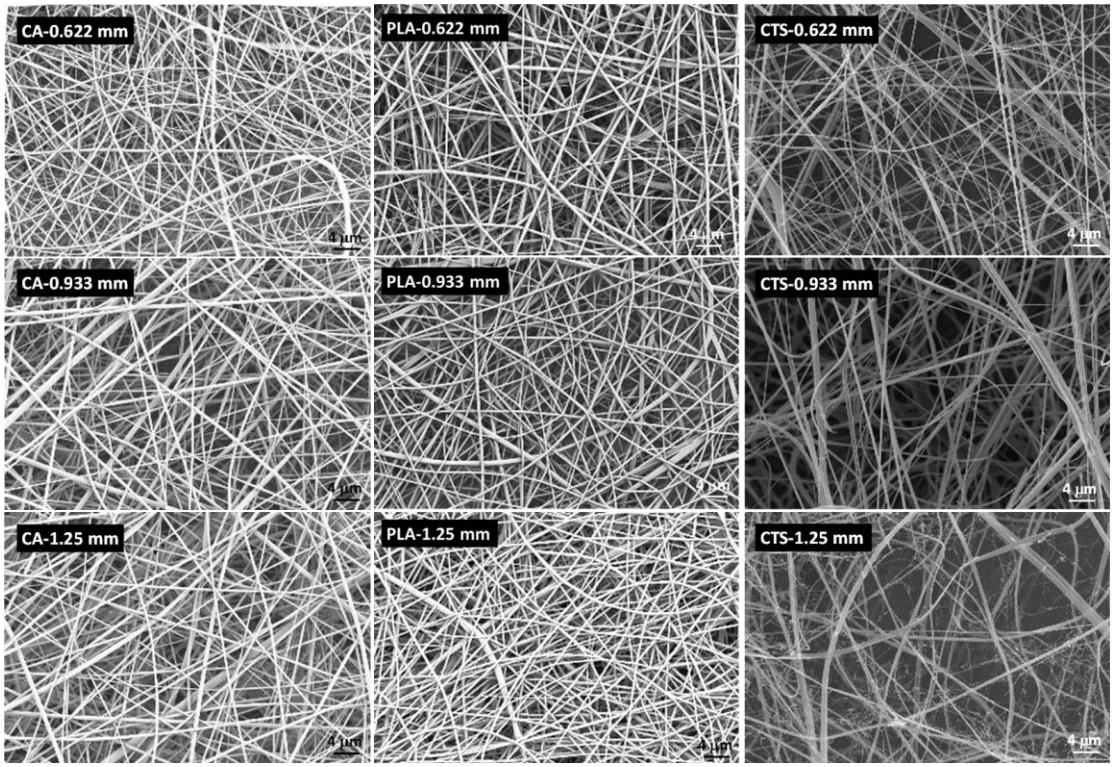

Figure 4.7 FESEM micrographs of the electrospun nanofibres at different needle size. Flow rate 1 mL/h. Concentrations: 17 w/v% CA, 11 w/v% PLA and 8 w/v% CTS

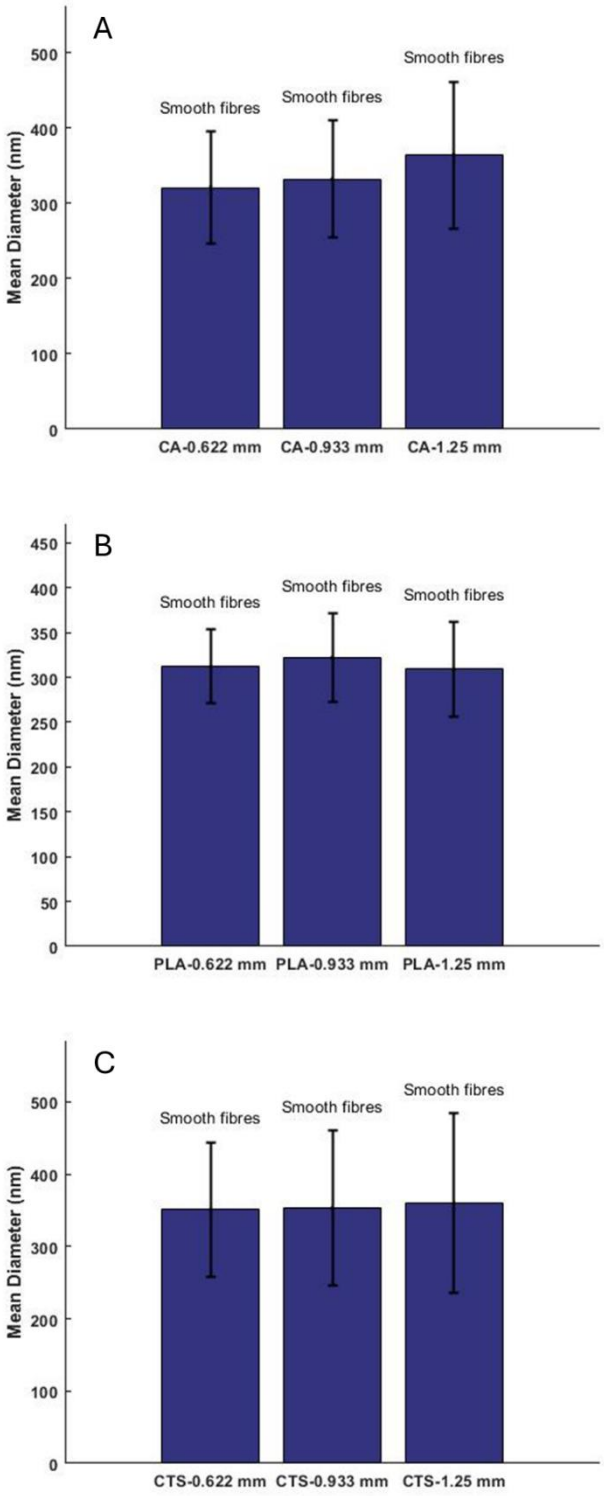

Figure 4.8 Mean diameter and morphology of electrospun nanofibres at different needle size: (A) CA, (B) PLA, (C) CTS. Flow rate 1 mL/h. Concentrations: 17 w/v% CA, 11 w/v% PLA and 8 w/v% CTS

4.3 Chapter 4 summary

Chapter 4 primarily investigated the production of precursor biopolymeric nanofibres with controlled diameter and morphology for the fabrication of CNFs. Polymeric nanofibres were successfully fabricated from CA, PLA, and CTS via electrospinning. The rheological properties of these three biopolymers were examined, along with the impact of certain experimental parameters in the electrospinning process on the morphology and size of the resulting nanofibres. For the biopolymers selected, the minimum concentrations required to achieve smooth nanofibres were established as 17 w/v% for CA, 11 w/v% for PLA, and 8 w/v% for CTS. The concentration of the polymer solutions significantly influences the diameter, with higher concentrations resulting in larger fibres. Flow rate also affects the size and morphology. An increased flow rate leads to an enlarged average diameter of fibres and, due to insufficient evaporation of the solvent, also resulted in the formation of some ribbon-like fibres. Considering production efficiency and the need for consistent fibre morphology, a flow rate of 1 mL/h was chosen. This rate ensures a good balance between fibre production efficiency and solvent evaporation. The size of the needle appeared to have a minor effect on the diameter of the fibres. Therefore, a medium-sized needle (0.933 mm) was chosen because it reduces the likelihood of clogging with smaller needles, and also avoids the unstable ejection of the solution and droplet formation associated with larger needles.

Chapter 5

Stabilisation of biopolymeric nanofibres: Results and discussion

5. Stabilisation of biopolymeric nanofibres: Results and discussion

5.1 Selection of the stabilisation temperature

To select the suitable stabilisation temperature, the thermal properties of the polymeric nanofibres were investigated by means of thermogravimetric analysis in air atmosphere.

Figure 5.1 (A) shows the TGA curve for the CELL nanofibres. From ambient conditions to 100 °C, there is a discernible weight diminution of roughly 5%, which is primarily due to the release of moisture inherent in the CELL nanofibres. During subsequent heating, further weight loss is noticed in two temperature regions. The initial interval occurs between 200 and 330 °C and corresponds to a substantial mass loss of approximately 65%. The second interval, ranging from 330 to 475 °C, is accompanied by a mass reduction of roughly 25%.

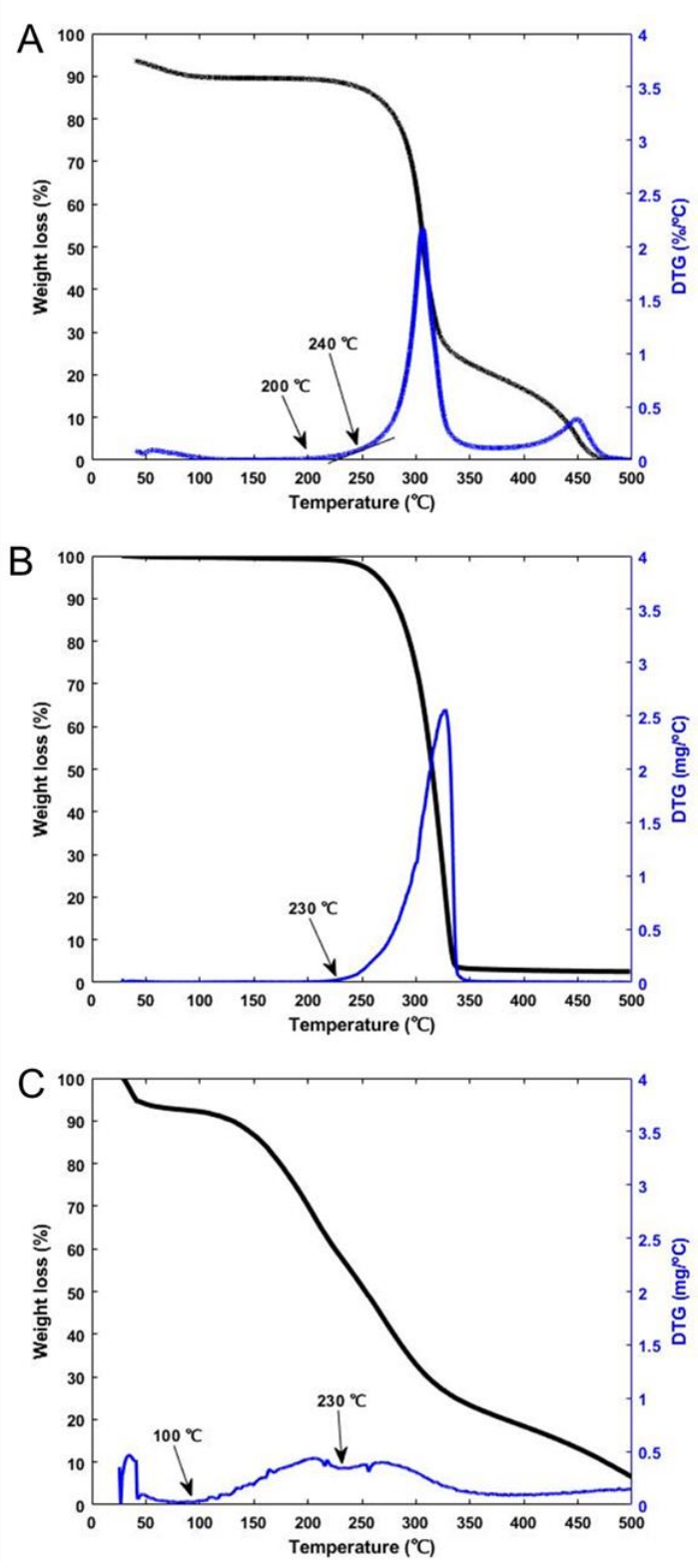

Figure 5.1 TGA and DTG curve of (A) CELL nanofibres, (B) PLA nanofibres, and (C) CTS nanofibres in air from room temperature to 500 °C at a heating rate of 10 °C /min

The derivative of TG (DTG) analysis (Figure 5.1 (A)) provides a clearer understanding of the thermal decomposition and depolymerisation processes occurring in the CELL nanofibres. As the temperature surpasses 200 °C, the DTG curve indicates the onset of thermal degradation. Above 240 °C, the decomposition rate of the CELL nanofibres increases significantly, reaching its highest point at 300 °C. The observed reduction in weight of the CELL nanofibres can be attributed to several phenomena. Initially, there is a sporadic breaking of chains in the less ordered areas of the cellulose. After these breaks, the relaxed chains go through several reactions, such as dehydration, decarboxylation, or decarbonylation from the anhydroglucose units [257]. Considering these findings, stabilisation temperatures were set at 200 °C and 240 °C. These temperatures were chosen to minimise mass loss during the stabilisation stage.

Figure 5.1 (B) shows the thermal stability of PLA nanofibres in air atmosphere. Owing to the absence of hydrophilic entities within PLA molecular chains, the TGA curve does not show a pronounced mass loss due to moisture. The majority of the weight loss occurs within the temperature range of 230 °C to 340°C, accounting for approximately 97% of the total mass reduction. Setting 230 °C as the initial stabilisation temperature for PLA nanofibres is impractical due to their relatively low melting point. The DSC curve of the PLA nanofibres (Figure 5.2) reveals a distinct endothermic peak at 140 °C, corresponding to the onset of the melting phase, and a more prominent peak at 160 °C, indicating the melting point. These thermal transitions highlight the critical temperatures where structural changes occur. Specifically, the onset temperature of 140 °C marks the beginning of thermal softening, leading to the degradation of the fibrous morphology. At 160 °C, a complete phase transition from solid to liquid occurs, making it evident that stabilisation temperatures exceeding this range would result in the destruction of the fibre structure. To preserve the fibrous morphology during stabilisation, a lower temperature of 120 °C was selected. This temperature ensures sufficient thermal energy to enable minor crosslinking of the polymer chains without inducing melting, thereby maintaining the integrity of the fibres. Subsequently, for the secondary stabilisation stage, a temperature of 140 °C was selected.

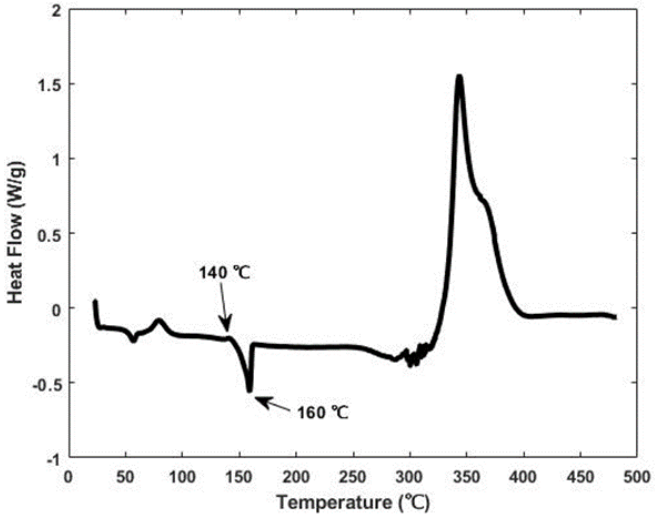

Figure 5.2 DSC curve of the PLA nanofibres in the air at the temperature range from room temperature to 500 °C at a heating rate of 10 °C /min

Figure 5.1 (C) presents the TGA analysis of CTS nanofibres in air. Below 70 °C, there is an observed weight reduction amounting for approximately 7% of the total mass of the sample, predominantly attributed to the evaporation of water molecules. The main weight reduction (67 %) occurs between 100 °C and 330 °C. As the temperature continues to rise, a steady reduction in the mass of the sample is observed, ultimately leading to its total depletion near 550 °C. Accordingly, for the first stabilisation stage a temperature of 100 °C was chosen for CTS nanofibers, since it is the point at which decomposition begins, and 230 °C for the second step, as supported by the DTG analysis (Figure 5.1 (C)).

The DTG analysis revealed that beyond 100 °C, the rate of mass loss in CTS increases sharply, peaking around 200 °C. This is likely due to the decomposition of amine units and the release of small molecules from the CTS nanofibres [258]. Following this peak, the rate of mass loss decreases, stabilising at around 230 °C. Nevertheless, at elevated temperatures, the rate of decomposition of the CTS nanofibres incrementally rises again, attributed to more intricate chemical reactions, such as the dehydration of saccharide rings, along with depolymerisation and decomposition of both acetylated and deacetylated units within the polymer [258].

Accordingly, to ensure a smooth stabilisation process and prevent damage to the fibres, 230 °C was determined as the optimal temperature for the second stabilisation stage.

5.2 Thermal properties of stabilised polymeric nanofibres

After determining the appropriate stabilisation temperatures, the polymeric nanofibres were subjected to stabilisation in a tube furnace. Various isothermal times, as described in the experimental section, were employed for this stabilisation process.

Table 5.1 summarises the stabilisation yield of the precursor nanofibers. The results indicate that increasing the isothermal time during the stabilisation process leads to lower stabilisation yields. The S-CELL 1-1 sample achieves the highest stabilisation yield at 60%, while the S-CELL 3-6 sample exhibits the lowest at 28.1%. Figure 5.3 (A) illustrates the thermal properties of the CELL nanofibres pre and post stabilisation in a nitrogen atmosphere.

Table 5.1 Stabilisation yield of CELL, PLA, and CTS nanofibres at different stabilisation conditions

Sample	Mass before stabilisation (mg)	Mass after stabilisation (mg)	Stabilisation yield (%)
S-CELL 1-1	40.2	24.1	60.0
S-CELL 3-3	30.8	14.5	47.1
S-CELL 3-6	46.2	13.0	28.1
S-CELL 6-6	33.6	9.8	29.2
S-PLA 1-1	28.6	28.4	99.3
S-PLA 3-3	30.2	29.9	99.0
S-PLA 3-6	31.5	30.7	97.4
S-PLA 6-3	27.7	27.2	98.2
S-CTS 1-1	48.6	19.1	39.3
S-CTS 3-3	45.9	15.8	34.4
S-CTS 3-6	52.5	15.4	29.3
S-CTS 6-3	44.8	13.6	30.4

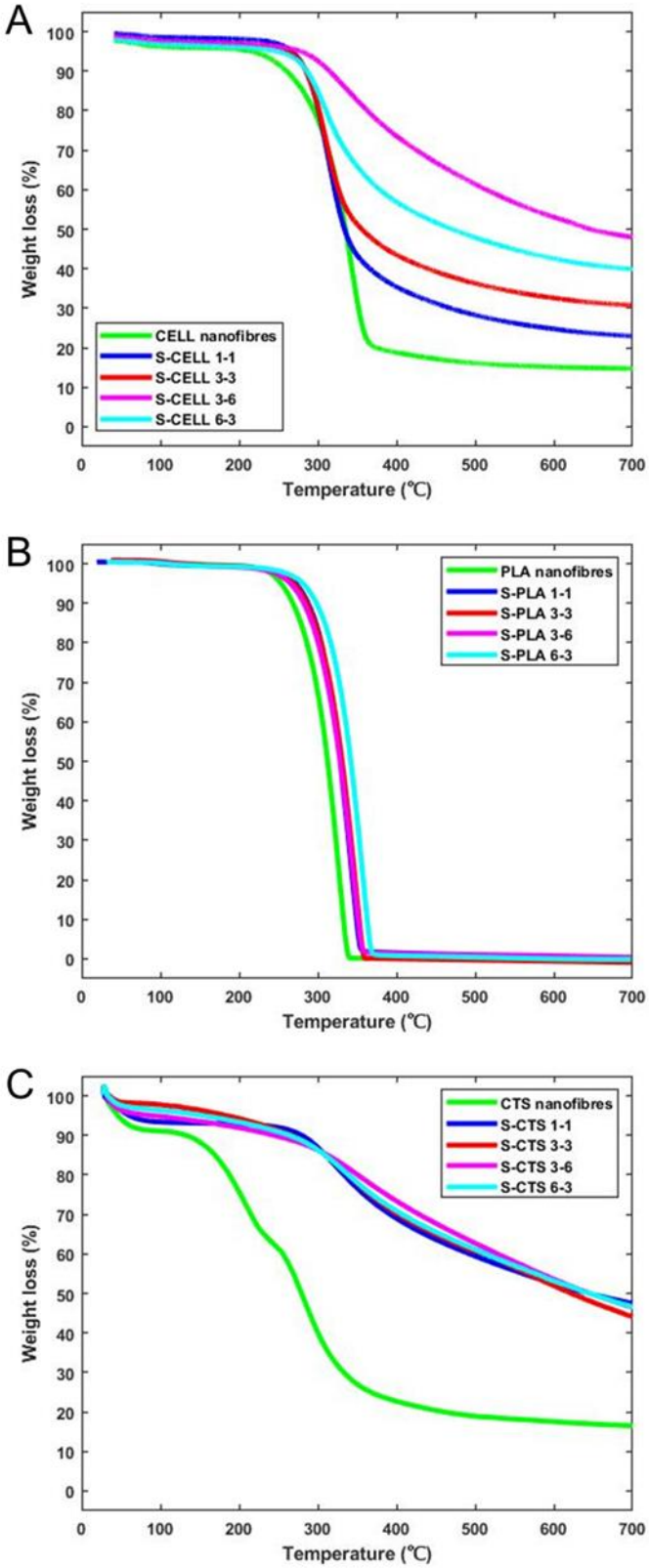

Figure 5.3 TGA curve of (A) CELL nanofibres, (B) PLA nanofibres, and (C) CTS nanofibres at different stabilisation conditions in nitrogen atmosphere from room temperature up to 700 °C at a heating rate of 10 °C /min

The unmodified CELL nanofibres show a lower degradation onset compared to the stabilised samples. They start degrading at approximately 200 °C and the decomposition curve reaches a plateau at 380 °C, and the final residue accounts for approximately 18% of the initial mass. In contrast, the stabilised CELL nanofibres display a higher degradation onset, beginning at around 260 °C, and they also leave a comparatively higher proportion of residual mass than the non-stabilised fibres. Overall, prolonged stabilisation periods promote enhanced thermal stability to the samples under nitrogen conditions.

Regarding the PLA nanofibres, due to their low melting point, it is challenging to achieve effective stabilisation, even with the longest isothermal time (Figure 5.3 (B)). Their thermal properties under nitrogen atmosphere remain unchanged before and after stabilisation, with minimal residual mass. Consequently, PLA does not seem to be a suitable biopolymer for the fabrication of CNFs.

Table 5.1 illustrates that increased heat treatment durations also result in reduced yields of CTS nanofibres, albeit the variance is less pronounced compared to that observed in CELL nanofibres. The stabilisation yields for CTS nanofibres vary between 29.3% and 39.3%, suggesting that these samples achieve full stabilisation even under the minimal stabilisation conditions. This is corroborated by the TGA data presented in Figure 5.3 (C), which shows that all four stabilised samples show markedly similar thermal degradation profiles. They commence thermal decomposition at about 230 °C, retaining roughly 45% of their initial mass. Conversely, the untreated CTS start decomposing at approximately 130 °C, leaving only an 18% of residual mass.

5.3 Chemical transformations during the stabilisation stages

Chemical structural changes of precursor nanofibres during the stabilisation process via cyclisation, oxidation, dehydrogenation, and cross-linking reactions [38], [203] along with chemical transformations can be monitored by means of FT-IR.

Figure 5.4 (A) presents the FT-IR spectra of both the untreated and stabilised CELL nanofibres. In the initial CELL nanofibres, distinct bands characteristic of cellulose are noticeable at around 3400, 2900, and 1050 cm^{-1}, which correspond to the O-H stretching, C-H bending, and C-O-C stretching vibrations, respectively [259]. After the stabilisation treatment, these bands undergo a decrease due to the ongoing dehydration reaction. Furthermore, this diminution in the bands becomes increasingly evident with extended durations of heat treatment. For instance, in the cases of S-CELL 3-6 and S-CELL 6-3, the C-O-C band is no longer present, yet two novel bands emerge, corresponding to C=O stretching at approximately 1710 cm^{-1} and C=C stretching at 1620 cm^{-1} [38], confirming the occurrence of the stabilisation process.

Figure 5.4 (B) displays the spectral bands representative of the functional groups in the CTS nanofibres. The broad absorption peaks at around 3450 cm^{-1} indicate the O-H stretching and amine N-H symmetric vibrations, whereas the absorption peak at approximately 2900 cm^{-1} is indicative of the C-H bond stretching vibration [260]. Near the wavenumber of 1650 cm^{-1}, the N-H bending vibration is observed, and the peak at 1200 cm^{-1} originates from the stretching vibrations of the C-O bond [261]. Furthermore, the notably strong peak at 1100 cm^{-1} is attributable to the stretching vibrations of the C-O-C group, which is characteristic of polysaccharides [262]. The FT-IR analyses reveal that the four stabilised CTS samples present nearly identical chemical structures, a conclusion that is consistent with the TGA data. These results imply that the CTS nanofibres achieve full stabilisation at the minimal isothermal durations. Following stabilisation, there is a noted reduction in the intensity of characteristic CTS bands, such as O-H, N-H, C-H, C-O, and C-O-C. Concurrently, two new peaks emerge at 1710 cm^{-1} and 1620 cm^{-1}, corresponding to C=O stretching and C=C stretching vibrations respectively.

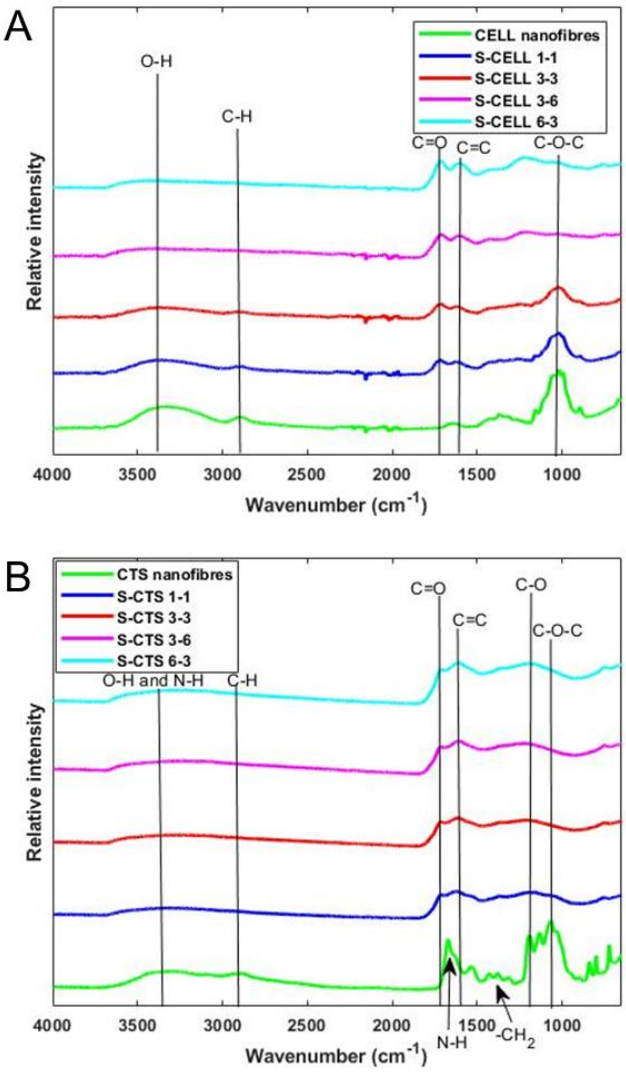

Figure 5.4 FT-IR spectra of (A) CELL nanofibres, and (B) CTS nanofibres at different stabilisation conditions.

5.4 Morphology and diameter of stabilised nanofibres

Figure 5.5 shows images of CELL nanofibres before and after stabilisation, and their diameter and morphology are summarised in Table 5.2. The initial CELL nanofibres exhibit a smooth surface morphology and an average diameter of approximately 368 nm. It is important to note that there is a difference in the diameters of CELL and CA nanofibres. The averaged diameter of CA nanofibres is 332 nm, as indicated in Table A.1. Following the deacetylation process, the CELL nanofibres exhibit a slight increase in diameter.

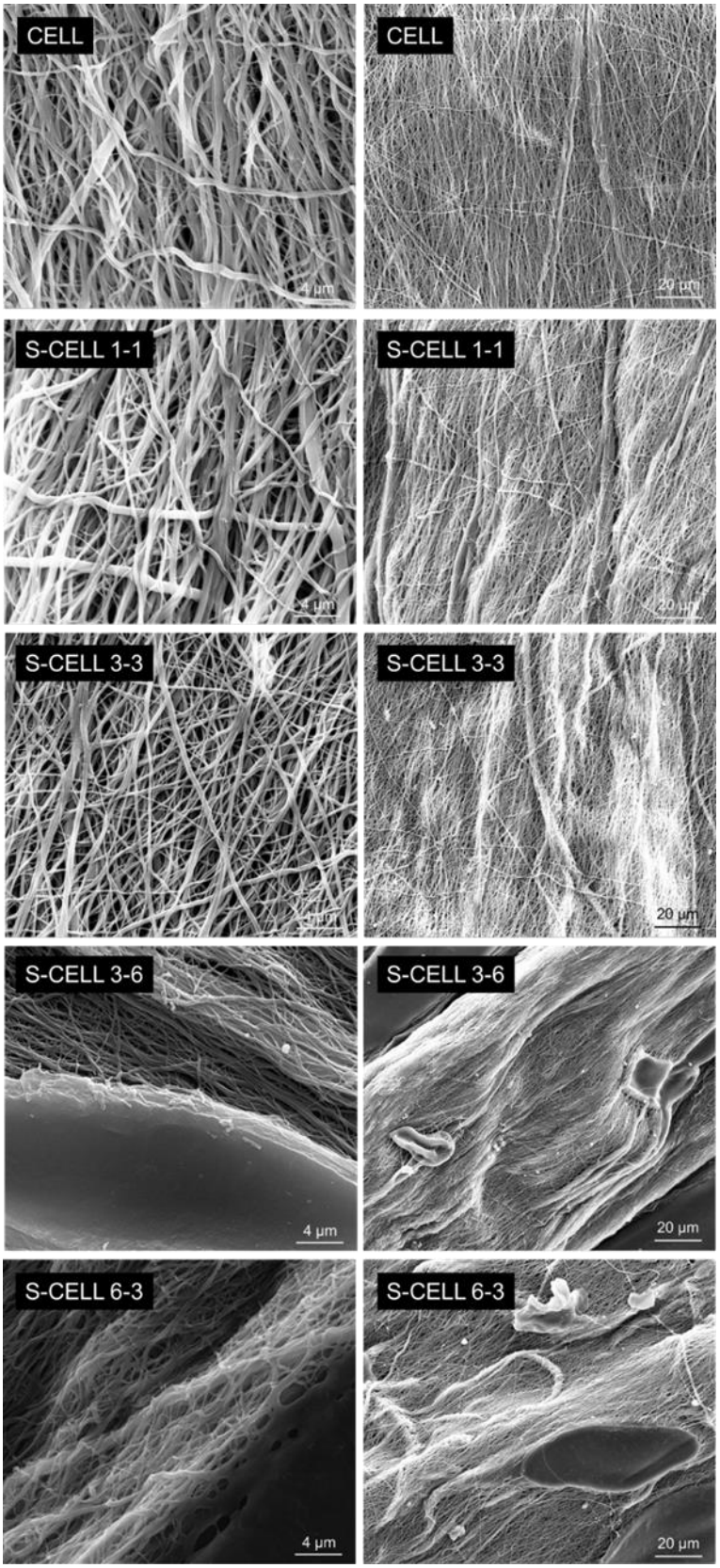
CELL
4 µm
CELL
20 µm
S-CELL 1-1
4 µm
S-CELL 1-1
20 µm
S-CELL 3-3
4 µm
S-CELL 3-3
20 µm
S-CELL 3-6
4 µm
S-CELL 3-6
20 µm
S-CELL 6-3
4 µm
S-CELL 6-3
20 µm

Figure 5.5 FESEM micrographs of CELL nanofibres obtained at different stabilisation conditions. Images at two different magnifications are provided to clearly show the damaged areas.

Table 5.2 Summary of diameter and morphology of stabilised CELL and CTS nanofibres

Sample name	**Mean diameter (nm)**	**Morphology**
CELL nanofibres	368 ± 89	Smooth fibres
S-CELL 1-1	348 ± 82	Smooth fibres
S-CELL 3-3	275 ± 76	Smooth fibres
S-CELL 3-6	196 ± 69	Smooth fibres with “damaged areas”
S-CELL 6-3	216 ± 58	Smooth fibres with “damaged areas”
CTS nanofibres	353 ± 107	Smooth fibres
S-CTS 1-1	305 ±104	Smooth fibres
S-CTS 3-3	301 ±106	Smooth fibres
S-CTS 3-6	316 ±113	Smooth fibres
S-CTS 6-3	300 ±117	Smooth fibres

As the isothermal duration increases, the diameter of CELL nanofibres progressively reduces, which is attributed to the reaction of oxygen with the sample and subsequent gas release. Morphologically, S-CELL 1-1 and S-CELL 3-3 maintain the smooth surface, whereas those subject to longer heat treatment times, such as S-CELL 3-6 and S-CELL 6-3, display non-fibrous morphology. This is more evident in the pictures shown in the right column of Figure 5.5, where it is easily noticeable the increase in 'damaged areas' on the fibre mat with longer isothermal times. These damaged areas may be caused by thermal degradation or structural collapse of the fibres due to prolonged exposure to high temperatures, leading to the breakdown of the polymer chains and loss of the fibrous structure [38]. Consequently, the excessively stabilised CELL nanofibres fail to maintain their structural integrity. As a result, the S-CELL 1-1 and S-CELL 3-3 samples were chosen for the subsequent carbonisation process.

Figure 5.6 presents the SEM images of CTS nanofibres before and after stabilisation, and the mean diameter is provided in Table 5.2. The untreated CTS nanofibres display a smooth surface with an average diameter of 353 ± 107 nm. Following stabilisation, the four samples retain the good morphology, while their diameters slightly decrease to approximately 300 nm. The

duration of isothermal treatment appears to exert minimal impact on either the morphology or diameter. Hence, all the stabilised CTS samples are deemed appropriate for the next carbonisation stage.

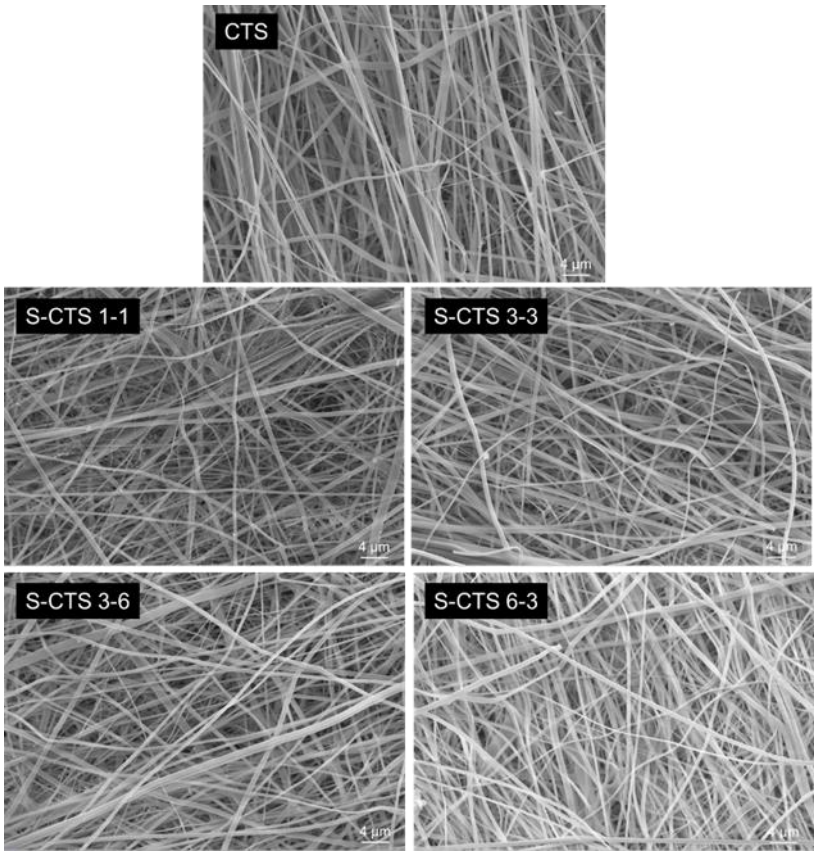

Figure 5.6 FESEM micrographs of CTS nanofibres at different stabilisation conditions

5.5 Chapter 5 summary

In this chapter, the stabilisation of CELL, PLA, and CTS nanofibres was investigated. Through the examination of their thermal properties, optimal temperatures for the two-stage stabilisation process were determined. For CELL nanofibres, the initial stabilisation temperature was set at 200 °C, with a second stage at 240 °C. For CTS nanofibres, the temperatures were 100 °C and 230 °C for the first and second stages, respectively. However, the stabilisation of PLA nanofibres proved to be challenging due to their lower melting point, leading to the decision to discard these samples. Subsequently, the stabilisation times were adjusted to optimise the process. All fibre samples exhibited significant dehydration, dehydrogenation, and cyclisation

after stabilisation, indicating the successful stabilisation was processed. Nonetheless, prolonged stabilisation of CELL nanofibres resulted in structural damage. Therefore, for CELL nanofibres, samples S-CELL 1-1 and S-CELL 3-3, which maintained good morphology, were chosen for carbonisation. In contrast, all stabilised CTS nanofibres maintained suitable morphology and thus selected for subsequent carbonisation.

Chapter 6

Carbonisation of biopolymer-based nanofibres and their activation: Results and discussion

6. Carbonisation of biopolymer-based nanofibres and their activation: Results and discussion

6.1 Carbonisation of stabilised polymeric nanofibers

The selected stabilised nanofibres were subjected to carbonisation to transform them into CNFs. Table 6.1 presents the carbonisation yields of the nanofibres prepared under different stabilisation conditions.

Table 6.1 Carbonisation yields for CELL and CTS nanofibres

Sample	Mass before carbonisation (mg)	Mass after carbonisation (mg)	Carbonisation yield (%)
C-CELL	87.2	12.9	14.8
C-CELL 1-1	90.8	36.8	40.5
C-CELL 3-3	98.6	43.7	44.3
C-CTS	78.3	12.5	15.9
C-CTS 1-1	87.8	37.0	42.1
C-CTS 3-3	86.5	36.8	42.5
C-CTS 3-6	79.7	34.4	43.2
C-CTS 6-3	85.3	36.5	42.8

The carbonisation yield of unstabilised nanofibres is lower for both C-CELL and C-CTS, specifically, the yield for C-CELL is only 14.8%, in contrast to C-CTS, which exhibits a slightly higher yield of 15.9%. Observations indicate a pronounced improvement in yield following stabilisation, highlighting the crucial role of this preparatory step. Notably, CELL nanofibres demonstrate a direct correlation between extended stabilisation time and enhanced yield, whereas CTS nanofibres display no clear link. This observation aligns with the results obtained from the TGA analysis (Figure 5.3).

Table 6.2 Total carbon yield of CELL and CTS nanofibres

Sample	Total carbon yield (%)
C-CELL	14.8
C-CELL 1-1	24.3
C-CELL 3-3	21.8
C-CTS	15.9
C-CTS 1-1	16.6
C-CTS 3-3	14.6
C-CTS 3-6	12.7
C-CTS 6-3	13.0

The total carbon yield refers to the percentage of carbon retained in the final carbonised product relative to the initial mass of the precursor nanofibres. Table 6.2 presents the total carbon yields throughout the process. For CELL nanofibres, the yield of unstabilised samples is only 14.8%. However, after stabilisation, the yield increases significantly; for instance, C-CELL 1-1 shows a carbon yield of 24.3%. When the stabilisation time is prolonged, the yield slightly decreases, as seen with C-CELL 3-3, which has a yield of 21.8%. A similar trend is observed with CTS nanofibres. The unstabilised CTS nanofibres yield 15.9%. After the shortest stabilisation time, the yield of C-CTS 1-1 rises to 16.6%. However, with further increases in stabilisation time, the yield gradually decreases, such as with C-CTS 3-6, which has a yield of 12.7%. This decrease is likely due to excessive oxidation and decomposition during prolonged stabilisation, leading to further carbon loss and reduced yields [263]. Therefore, while stabilisation improves carbon yield, extended durations may have adverse effects.

Figure 6.1 illustrates the morphological characteristics of the carbonised CELL nanofibres. The morphological integrity of the non-stabilised C-CELL and C-CELL 1-1 appears to be compromised. The formation of pores in the carbonised samples is predominantly due to the release of volatile matter and the structural rearrangement of the precursor materials [264]. However, the C-CELL 3-3 sample exhibits a uniform fibre morphology, implying enhanced stability and therefore confirming that the selected stabilisation conditions for CELL nanofibres are 3 hours at 200 °C and 3 hours at 240 °C under an air atmosphere.

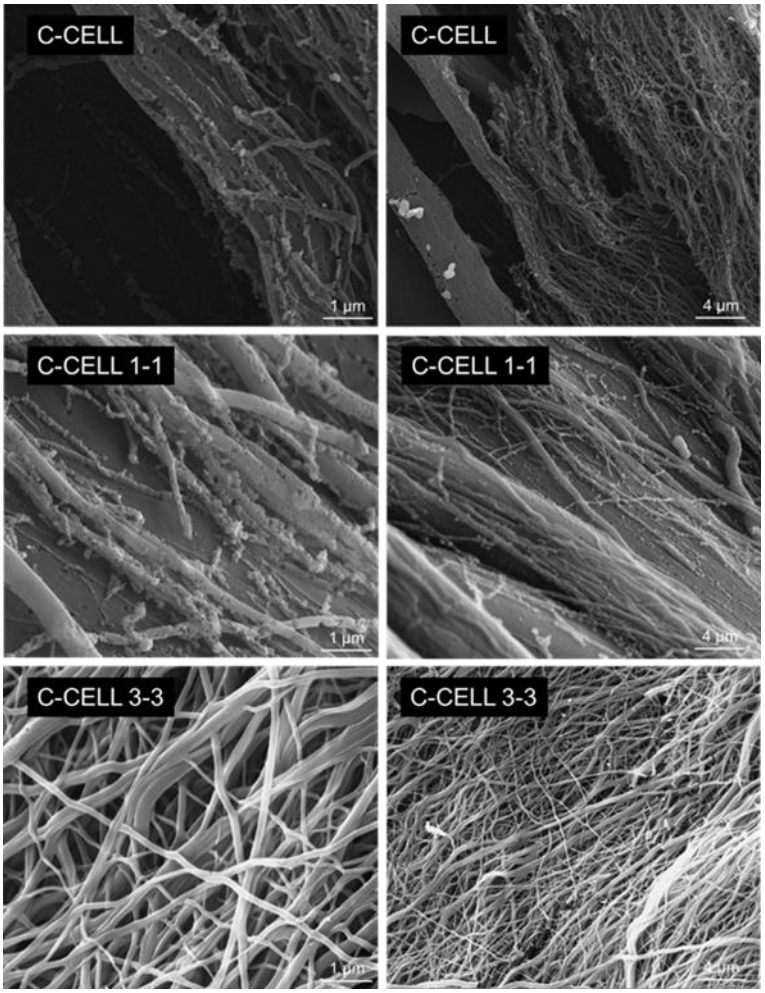

Figure 6.1 FESEM micrographs of carbonised CELL nanofibres at different stabilisation conditions. Images at two different magnifications included to show further detail about the morphology.

Figure 6.2 presents the SEM images of the CTS-series samples after carbonisation. Although the non-stabilised CTS CNFs retained their morphological integrity, the formation of a few pores is observed. By contrast, the stabilised CTS CNFs show a smoother surface. Based on the results outlined above, the stabilisation parameters for C-CTS 1-1—holding the temperature at 100°C and 230°C for one hour each—were selected for subsequent experiments. This choice is justified by the smooth morphology and relatively high carbon yield of C-CTS 1-1, as well as the reduced time and energy costs associated with shorter stabilisation times.

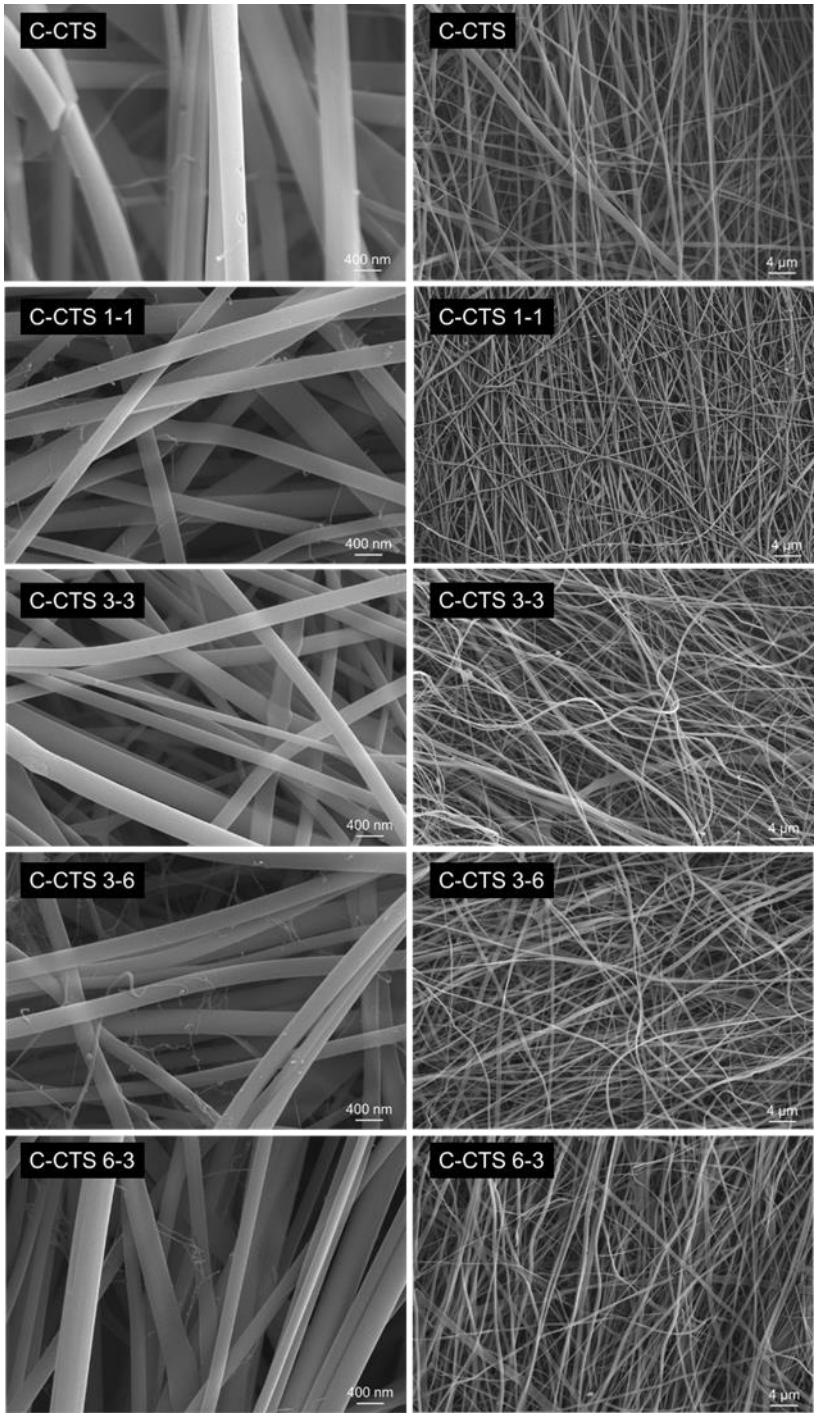

Figure 6.2 FESEM micrographs of carbonised CTS nanofibres at different stabilisation conditions. Images at two different magnifications included to show further detail about the morphology.

The diameter of the carbonised nanofibres is summarised in Table 6.3. Within the CELL series of samples, only the morphology of C-CELL 3-3 is well preserved, with an average diameter

of 126 nm. Conversely, all carbonised CTS nanofibres displayed a similar diameter of approximately 220 nm.

Table 6.3 Summary of diameter and morphology of carbonised CELL and CTS nanofibres at different stabilisation conditions

Sample	Mean diameter (nm)	Morphology
C-CELL	-	Damaged
C-CELL 1-1	-	Damaged
C-CELL 3-3	126 ± 49	Smooth fibres
C-CTS	218 ± 69	Smooth fibres with a few pores
C-CTS 1-1	219 ± 74	Smooth fibres
C-CTS 3-3	218 ± 68	Smooth fibres
C-CTS 3-6	227 ± 70	Smooth fibres
C-CTS 6-3	216 ± 73	Smooth fibres

In addition, it is noteworthy that carbonised fibres exhibit a significantly smaller diameter than stabilised ones. For instance, the diameter of S-CELL 3-3 is 275 nm (Table 5.2), however after carbonisation the diameter of C-CELL 3-3 notably decreases to 126 nm. On the other hand, the diameter of CTS nanofibres experiences a lesser reduction following carbonisation compared to CELL nanofibres. For example, with an identical isothermal duration, the average diameter is reduced from 301 nm (corresponding to S-CTS 3-3, Table 5.2) to 218 nm after carbonisation (C-CTS 3-3, Table 6.3). This disparity may be linked to the robust cross-linked structure of CTS, consisting of N-acetylglucosamine units, along with its strong linear configuration and extensive intermolecular hydrogen bonding [265]. The cross-linked configuration of the CTS nanofibres potentially imparts superior mechanical strength and thermal stability. Conversely, cellulose comprises glucose units interconnected through β-1,4-glycosidic bonds, fostering a more linear and planar molecular structure with limited cross-linking sites. This structural characteristic may contribute to its comparatively reduced thermal stability [266].

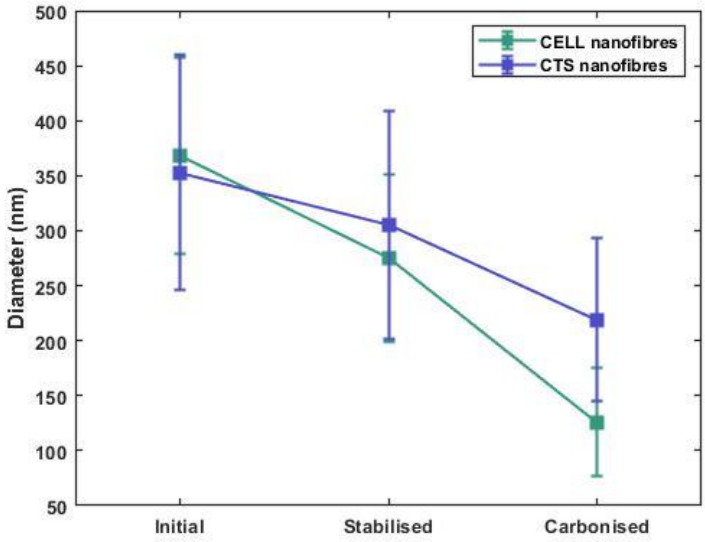

Figure 6.3 Diameter changes of CELL and CTS nanofibres during selected stabilisation and carbonisation processes.

Accordingly, C-CELL 3-3 and CTS 1-1, both prepared under their most suitable stabilisation conditions, were selected for further characterisation. From this point forward, C-CELL and C-CTS denote the corresponding CNFs prepared via the preferred stabilisation. Figure 6.3 illustrates the diameter changes of CELL and CTS nanofibres throughout the entire process. The CELL nanofibres show a significant decrease in diameter from the initial stage (368 nm) to the carbonised stage (126 nm), resulting in an overall reduction of approximately 66%. Meanwhile, the CTS nanofibres exhibit a decrease in diameter from the initial stage (353 nm) to the carbonised stage (219 nm), corresponding to a reduction of approximately 38%. In contrast to the nanofibre diameter, the shrinkage of the fibre mats after heat treatment posed additional challenges for accurate measurement. Due to curling and deformation of the mats during the process, reliable assessment of the overall mat shrinkage was not feasible. These experimental constraints resulted in the absence of specific quantitative data for mat shrinkage at this stage.

To determine the specific surface area and pore volume of C-CELL and C-CTS, N_2 adsorption–desorption isotherms were measured. Both exhibit characteristic type I isotherms (Figure 6.4

(A)), with a pronounced nitrogen uptake at low relative pressures, indicating that the CNFs are predominantly microporous [241]. Figure 6.4 (B) summarises the BET-specific surface areas and pore volumes for C-CELL and C-CTS. The BET specific surface area of C-CELL (627 m^2/g) is higher than that of C-CTS (568 m^2/g), which may be due to their smaller diameter (126 nm vs 219 nm, Table 6.3). Regarding pore volume, C-CELL also exhibits a marginally higher value compared to C-CTS, primarily due to a greater volume of mesopores.

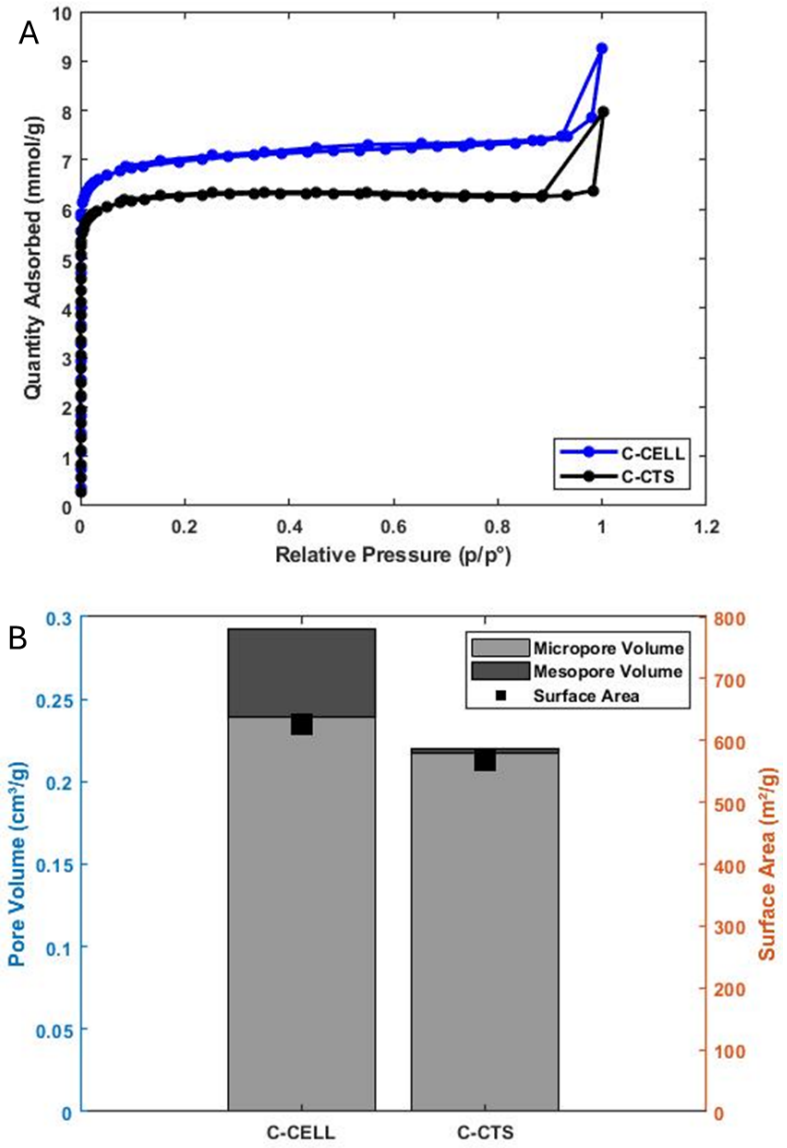

Figure 6.4 (A) N_2 adsorption–desorption isotherms of C-CELL and C-CTS; (B) Summary of pore volume and BET-specific surface area of C-CELL and C-CTS

The XPS survey scan for C-CELL and C-CTS reveals the presence of characteristic carbon and oxygen peaks in both samples, with an additional N1s peak observed in C-CTS. The relative content of the functional groups is presented in Table 6.4.

Notably, C-CELL exhibits a higher oxygen content compared to C-CTS, primarily contributed by carboxylic groups (Table 6.4, Figure 6.5). This difference is attributed to the inherent chemical structure of CELL, which is derived from CA through deacetylation. During deacetylation, acetate groups are removed, potentially restoring some or all the hydroxyl groups [267]. Subsequent oxidation of these hydroxyl groups may lead to the formation of carboxylic groups [268].

Table 6.4 Surface chemistry of C-CELL and C-CTS determined by XPS (at.%)

	C-CELL	**C-CTS**
Atomic concentration		
C1s	90.2	85.5
O1s	8.3	6.1
N1s	-	8.3
C1s curve		
C graphitic	61.2	68.8
C(epoxy)/C-OH/C=N	23.6	13.3
C=O/C-N	3.4	13.2
COOH	11.6	2.9
π-π*	0.2	1.8
N1s curve		
N6	-	23.8
N5	-	32.0
NQ	-	39.5
N-X	-	4.6

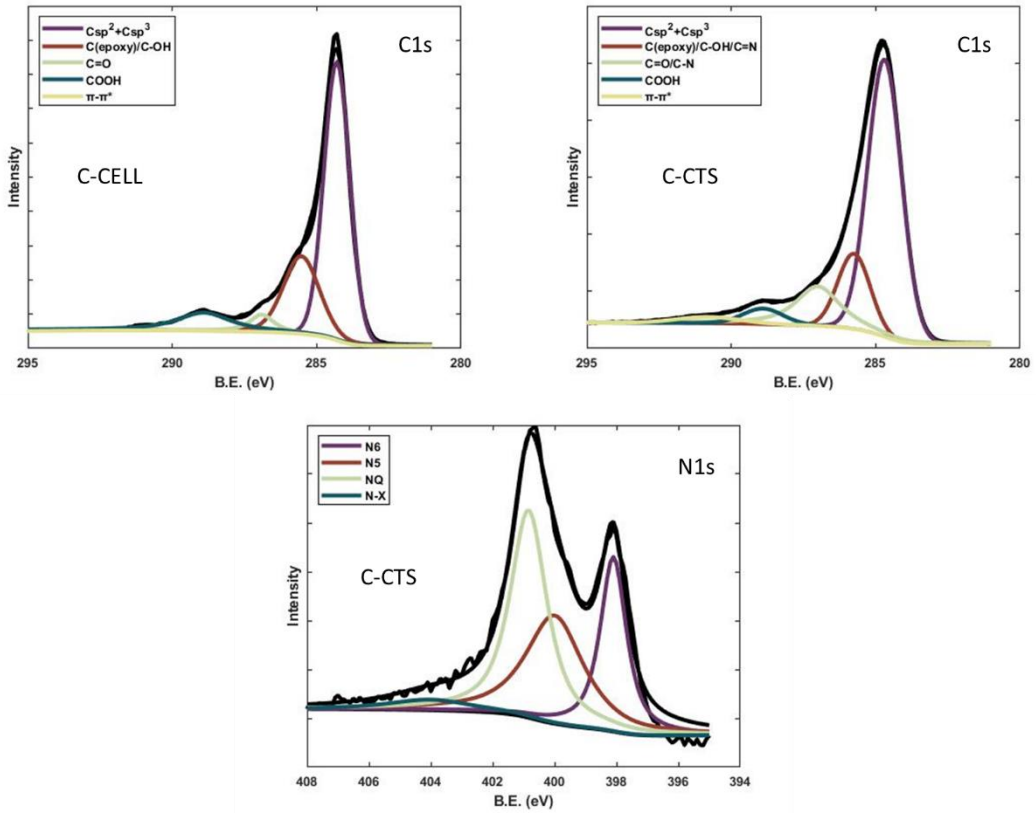

Figure 6.5 XPS spectra of C-CELL and C-CTS in the core level scans of C1s and N1s.

The N1s curve (Figure 6.5) deconvolution for C-CTS reveals that the surface nitrogen functional groups are predominantly contributed by N6, N5, and NQ. Literatures have demonstrated the potential of pyridinic (from N6) and pyrrolic-N (from N5) to enhance the pseudocapacitive effect [269]. Additionally, a minor presence of N-X, typically attributed to oxidised nitrogen forms (such as Pyridine N-oxide) or inorganic nitrogen, has been identified. However, the characteristics of these components remain a subject of debate [270].

The wettability of C-CELL and C-CTS further confirms their differences in surface chemistry. Figure 6.6 displays photographic evidence of water droplet interactions on the surfaces of C-CELL and C-CTS. Due to the presence of many carboxylic and hydroxyl groups on the C-CELL surface, its water contact angle is approximately 19.8°, affirming its hydrophilic nature [271]. In contrast, the water contact angle for C-CTS is about 117°, indicating its hydrophobic characteristics. At high temperatures, such as those experienced during carbonisation, functional groups in CTS, like hydroxyl, amino, and carboxyl groups, which are crucial for

hydrophilicity in its non-carbonised state, may be lost. The XPS results show a relatively low presence of these functional groups in C-CTS (Table 6.4 and Figure 6.5), leading to a significant decrease in surface polarity, thereby rendering the material hydrophobic [272].

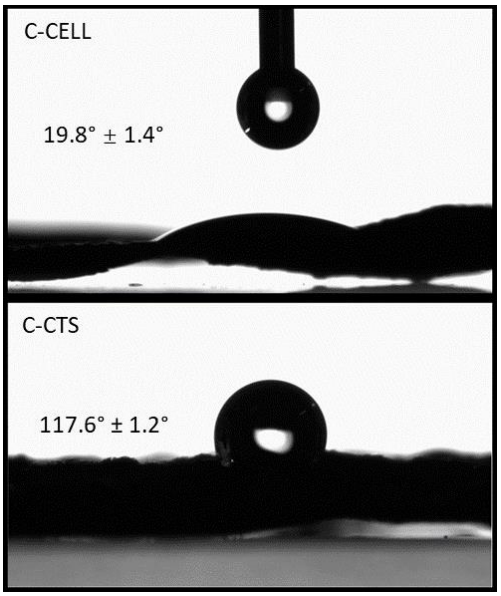

Figure 6.6 Contact angle of water droplet on C-CELL and C-CTS

6.2 Activation of carbon nanofibers

CNFs prepared under the most suitable stabilisation conditions, specifically C-CELL 3-3 and C-CTS 1-1, were selected for further activation experiments. Figure 6.7 displays the SEM images of the nanofibres post-activation, showing that all fibres retain their fibrous morphology. For fibres activated with H_3PO_4, the diameter remains virtually unchanged compared to their non-activated counterparts. However, the fibre diameters undergo a reduction following $ZnCl_2$ activation. For instance, the diameter of A-CTS $ZnCl_2$ 1-3 is 219 nm before activation, while it decreases to 167 nm afterwards (Table 6.5). This decrease is likely due to fibre shrinkage during the dehydration induced by $ZnCl_2$ activation [223].

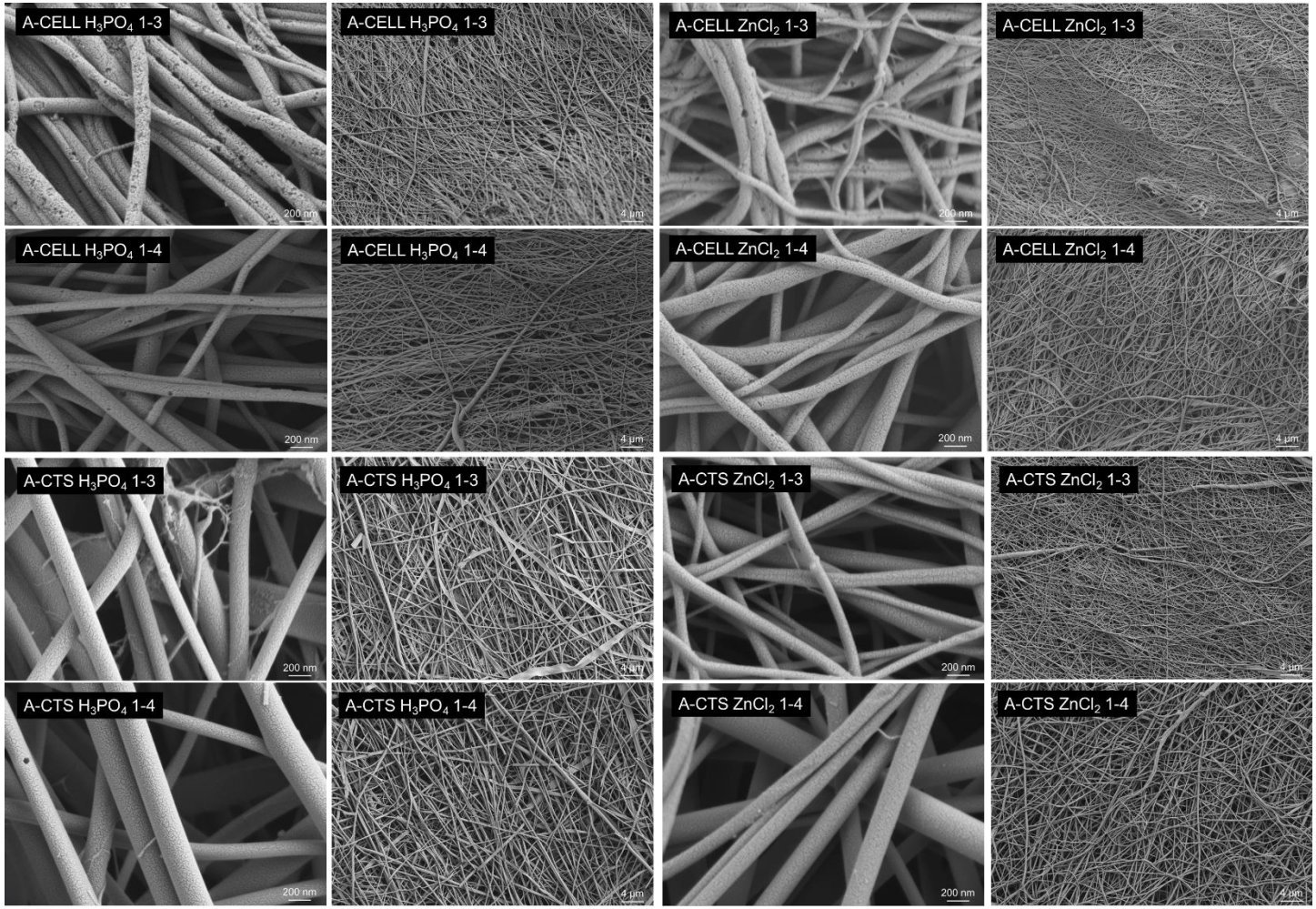

Figure 6.7 FESEM micrographs of the H_3PO_4 and $ZnCl_2$ activated CELL/CTS carbon nanofibres at impregnation ratios 1:3 and 1:4 w/w

Table 6.5 Summary of diameter and morphology of H_3PO_4 and $ZnCl_2$ activated CELL/CTS nanofibres with different impregnation ratios (1:3 and 1:4 w/w)

Sample	Mean diameter (nm)	Morphology
A-CELL H_3PO_4 1-3	129 ± 45	Smooth fibres
A-CELL H_3PO_4 1-4	121 ± 42	Smooth fibres
A-CTS H_3PO_4 1-3	211 ± 72	Smooth fibres
A-CTS H_3PO_4 1-4	214 ± 60	Smooth fibres
A-CELL $ZnCl_2$ 1-3	114 ± 45	Smooth fibres
A-CELL $ZnCl_2$ 1-4	116 ± 54	Smooth fibres
A-CTS $ZnCl_2$ 1-3	167 ± 69	Smooth fibres
A-CTS $ZnCl_2$ 1-4	168 ± 66	Smooth fibres

Although FESEM images reveal that A-CELL samples still retain their fibrous morphology, the reality is that after activation the samples were brittle and therefore unsuitable to fabricate freestanding electrodes due to their inadequate mechanical strength (see Figure 6.8 (A)). Accordingly, the A-CELL samples had to be discarded and not further considered.

In contrast, A-CTS samples exhibit a good mechanical strength and suitable handling, as shown in Figure 6.8 (B) and (C). Hence, A-CTS series was characterised further.

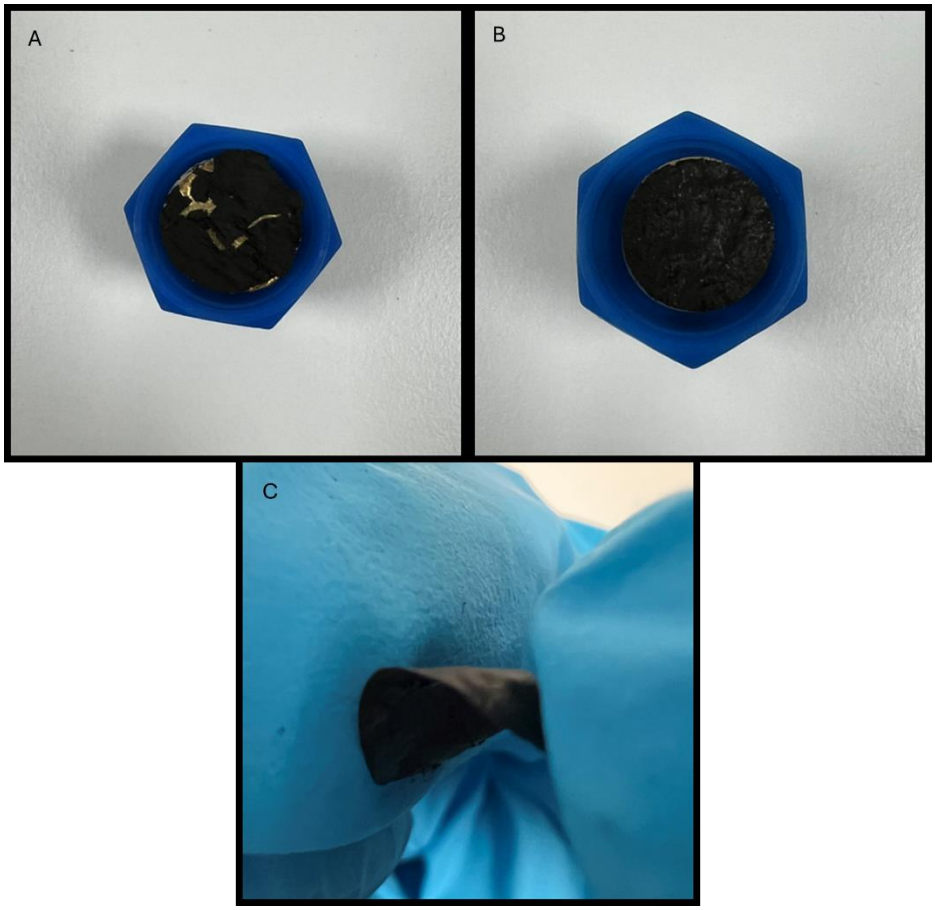

Figure 6.8 Photograph of the electrode prepared by (A) A-CELL, (B) A-CTS; (C) flexibility demonstration of the A-CTS electrode.

After activation, the A-CTS samples exhibit characteristic type I isotherms (Figure 6.9), indicating there are predominantly microporous materials. Compared to C-CTS, A-CTS shows a decrease in adsorption capacity, signifying a reduction in specific surface area. Figure 6.9 (B) illustrates their BET specific surface areas and pore volume. Post-activation, the specific surface area of CNFs decreases, accompanied by a reduction in micropore volume. For instance, C-CTS has a BET-specific surface area of 568 m^2/g and a micropore volume of 0.22 cm^3/g. However, after activation with H_3PO_4 (A-CTS H_3PO_4 1-3), its BET specific surface area reduces to 259 m^2/g, and the micropore volume decreases to 0.10 cm^3/g. Qiu et al. point out that the textural characteristics of carbon materials are influenced by oxygen-containing functional groups. The incorporation of these functional groups leads to the formation of micropores and an initial increase in specific surface area, attributed to carbon loss. As the

concentration of oxygen-containing functional groups rises, a transition of some micropores into mesopores occurs. However, an excessive concentration of these functional groups can block micropores and cause the collapse of pore walls, ultimately decreasing the specific surface area [75]. Hence, the reduction of specific surface area may be attributed to the blockage of micropores by oxygen functional groups introduced during the activation process [273], [274]. The observed decrease in specific surface area and micropore volume, with a concurrent increase in mesopores, suggests that the benefits of increased mesopore volume are offset by the excessive blockage of micropores, ultimately reducing overall specific surface area. CNFs activated with $ZnCl_2$ show a larger specific surface area than those activated with H_3PO_4, likely due to the smaller diameter of $ZnCl_2$ activated CNFs (Table 6.5) and the less obstructive impact of $ZnCl_2$ activation on micropores.

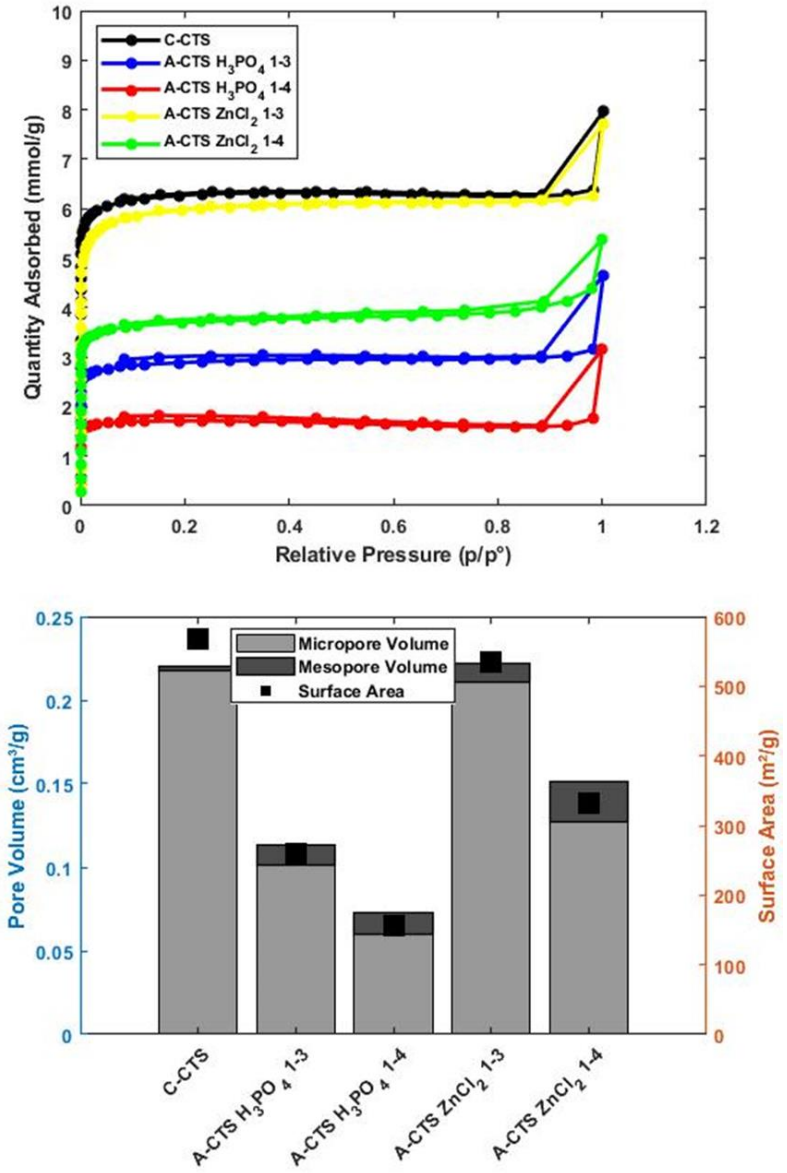

Figure 6.9 (A) N_2 adsorption–desorption isotherms of the CTS-based CNFs and ACNFs; (B) Summary of pore volume and BET specific surface area of CTS-based CNFs and ACNFs.

Therefore, to investigate the changes in functional groups on the surface of CNFs after activation, XPS was employed. The C1s and N1s spectra of the activated CNFs were deconvoluted, and the relative content of the functional groups is presented in Table 6.6. Following H_3PO_4 activation, a significant increase in oxygen content on the fibre surface is observed. As the H_3PO_4 activation ratio increases, the proportion of oxygen also rises. For example, the surface oxygen content for A-CTS H_3PO_4 1-3 is 7.9 at.%, which escalates to 15.2

at.% when the activation ratio is elevated to 1:4. During the H_3PO_4 activation process, phosphorus is incorporated into the fibres. This occurs as phosphoric acid, used in the activation, decomposes at high temperatures, generating phosphate ions. These ions may react with surface hydroxyl groups on the CNFs, forming phosphate groups [233]. Notably, at a higher H_3PO_4 impregnation ratio (1:4), A-CTS shows a substantial phosphorus content of 6.9 at.%, which is significantly higher than that observed at a lower ratio (1:3). This elevated phosphorus content suggests incomplete removal of phosphate compounds, which strongly adsorb onto the carbon surface and resist washing [275]. Consequently, phosphorus residues may remain, reducing specific surface area and altering surface functional groups [276]. Similarly, following the activation of CTS nanofibres with $ZnCl_2$, trace amounts of Zn compounds persist despite washing. This residual presence may be due to molten Zn salt intercalating into the carbon layers during high-temperature treatment, potentially resulting in the formation of ZnO or Zn complexes that are challenging to eliminate [277].

Table 6.6 Surface chemistry of A-CTS series determined by XPS (at.%).

	A-CTS H_3PO_4 1-3	**A-CTS H_3PO_4 1-4**	**A-CTS $ZnCl_2$ 1-3**	**A-CTS $ZnCl_2$ 1-4**
Atomic concentration				
C1s	84.5	72.3	85.7	83.8
O1s	7.9	15.2	7.6	9.1
N1s	5.2	4.1	5.3	4.5
P2p	2.3	6.9	-	-
Zn2p	-	-	0.1	0.5
C1s curve				
C graphitic	65.4	62.9	64.0	63.5
C(epoxy)/C-OH/C=N	18.1	23.9	21.1	21.6
C=O/C-N	11.4	7.5	11.5	9.9
COOH	4.3	5.1	3.1	4.4
π-π*	0.7	0.6	0.2	0.6
N1s curve				
N6	18.8	15.3	19.8	23.9
N5	34.5	36.4	35.0	30.5
NQ	45.4	44.6	41.3	44.7
N-X	1.3	4.1	3.7	0.9

The deconvolution results of the C1s spectra are shown in Figure 6.10. Compared to the non-activated C-CTS (Table 6.4), the CTS nanofibres activated with H_3PO_4 has more carboxylic

and hydroxy groups. The formation of these functional groups is attributed to the oxidising effect of phosphoric acid [233]. Furthermore, CNFs activated with $ZnCl_2$ exhibited a slight increase in oxygen-containing functional groups on their surface, primarily attributed to hydroxyl groups. This finding is consistent with the observations made by Liu et al. [223].

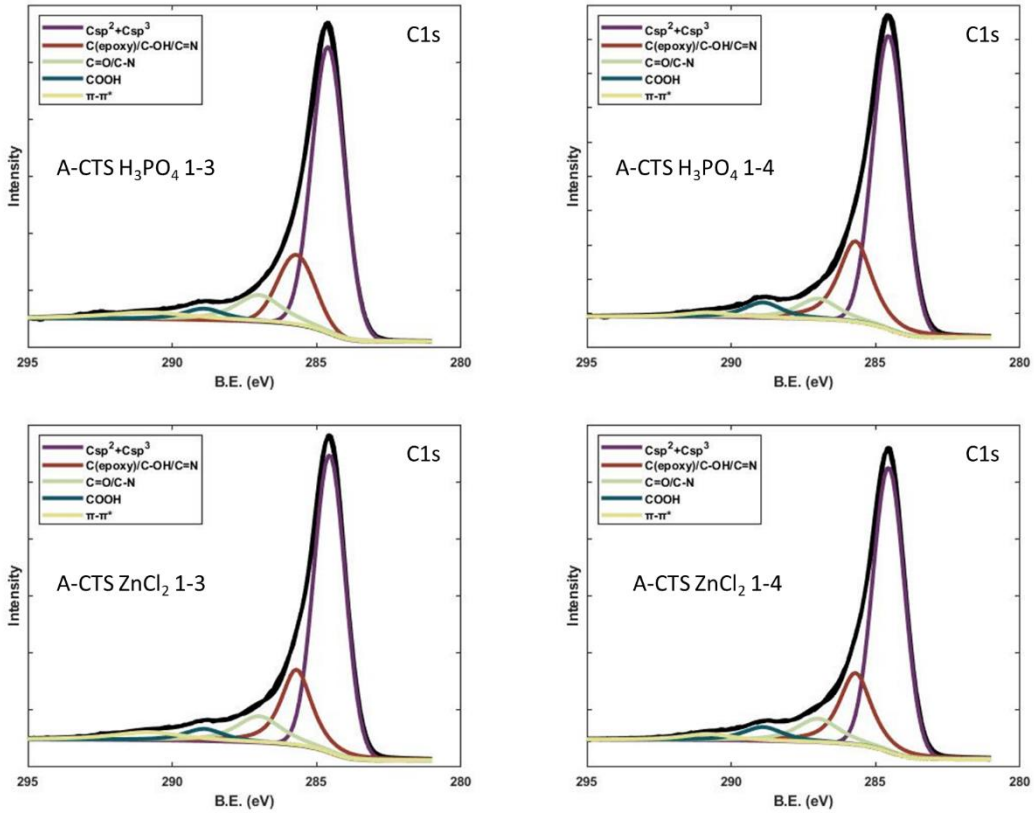

Figure 6.10 XPS C1s profiles of activated CTS nanofibres

The results of fitting the N1s curve are displayed in Figure 6.11. After activation (whether with H_3PO_4 or $ZnCl_2$), the concentration of NQ increases as N6 and N5 decrease. This observation suggests a transformation of N6 and N5 into NQ during the activation process [223].

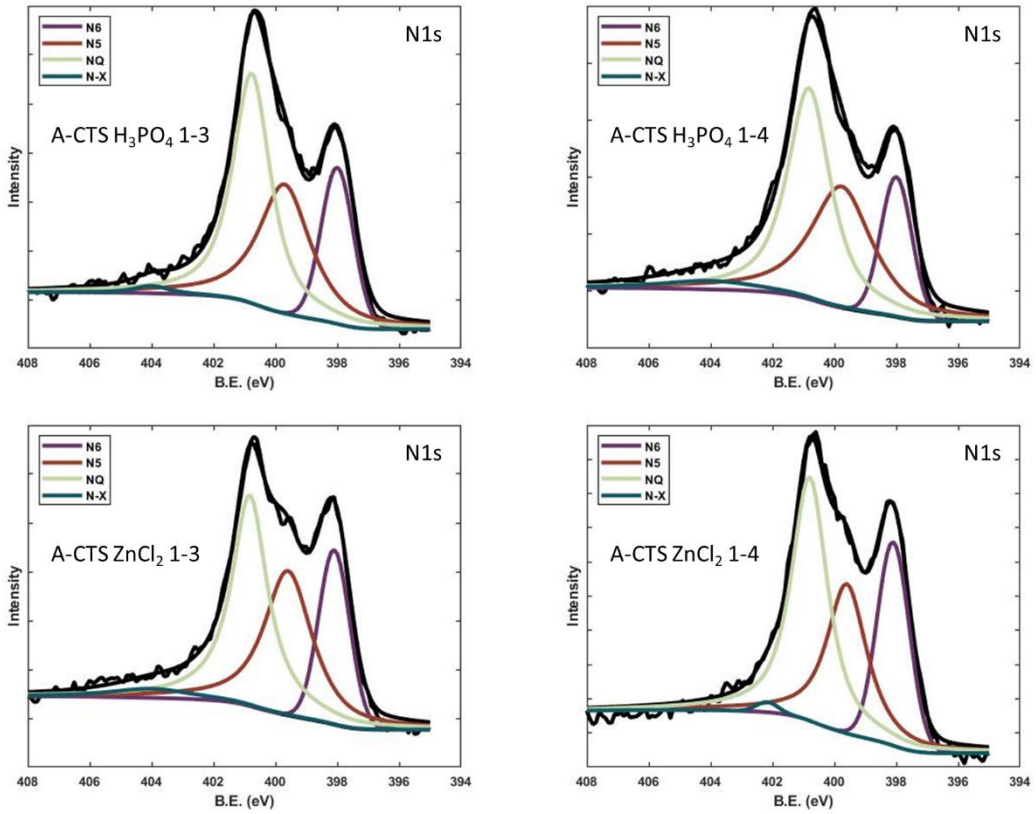

Figure 6.11 XPS N1s profiles of activated CTS nanofibres

The wettability of ACNFs is assessed through water contact angle measurements (as depicted in Figure 6.12). Although the C-CTS exhibits a hydrophobic nature (Figure 6.6), their properties experience a significant transformation after activation with H_3PO_4. For instance, A-CTS H_3PO_4 1-3 has a water contact angle of 26.9°, indicating its hydrophilicity. Moreover, C-CTS activated with $ZnCl_2$ also displays hydrophilic properties, as evidenced by a contact angle of 19.4° for samples A-CTS $ZnCl_2$ 1-4.

This enhancement in wettability after activation can be attributed to changes in the surface functional groups due to chemical activation. For H_3PO_4 activation, the abundance of carboxylic and hydroxy groups lead to increased hydrophilicity in the ACNFs. In $ZnCl_2$ activation, the slight incorporation of Zn elements, along with modifications in oxygen and nitrogen functional groups on the material's surface, plays a crucial role in enhancing hydrophilicity. This observation is corroborated by findings from Rufford et al. [278] and Xiang

et al. [279], who have also demonstrated the significant influence of $ZnCl_2$ activation on the oxygen and nitrogen functional groups on the carbon surface.

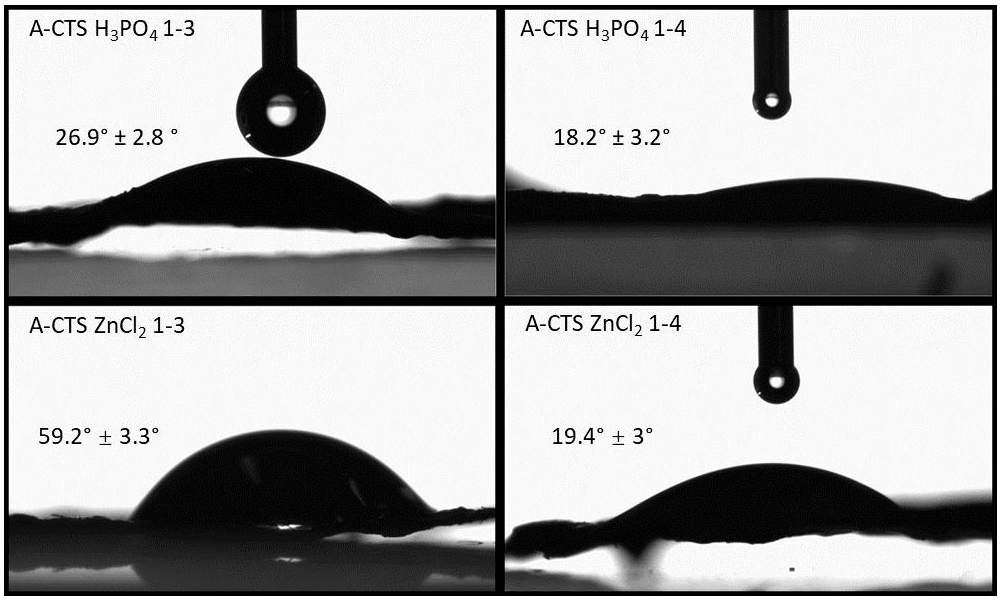

Figure 6.12 Contact angle of water droplet on activated CTS nanofibres

6.3 Chapter 6 Summary

This chapter examined the changes in fibre morphology under different stabilisation conditions during carbonisation, further solidifying the selection of most effective stabilisation conditions. The results indicated that the preparation parameters for C-CELL 3-3 and C-CTS 1-1, respectively, represent the selected procedures for preparing CELL-based CNFs and CTS-based CNFs. Consequently, further investigations were conducted on CNFs prepared using these parameters under different activators (H_3PO_4 and $ZnCl_2$) and activation ratios (1:3, 1:4). However, after activation, CELL-based CNFs had insufficient mechanical strength to be fabricated into freestanding electrodes for final electrochemical performance testing and thus were discarded. In contrast, CTS-based CNFs retained good mechanical strength and flexibility after activation. After H_3PO_4 activation, CTS-based CNFs' surfaces were augmented with many oxygen-containing functional groups. Conversely, $ZnCl_2$ activation altered the oxygen and nitrogen functional groups on the CNFs' surface. These modifications in surface chemistry resulted in the blockage of micropores within the CNFs after activation, thereby leading to a

reduction in BET surface area while the volume of mesopores saw an increase. Moreover, these changes transformed the inherently hydrophobic C-CTS into hydrophilic after activation.

Chapter 7

Electrochemical characterisation of CNFs and ACNFs as electrodes in supercapacitors: Results and discussion

7. Electrochemical characterisation of CNFs and ACNFs as electrodes in supercapacitors: Results and discussion

To explore the impact of the different activation procedures, the electrochemical performance of the A-CTS series of samples, comprising those activated with H_3PO_4 and $ZnCl_2$ at ratios of 1:3 and 1:4 (w/w), was tested as electrode in supercapacitors (SCs). In addition, the electrochemical behaviour of C-CTS was also included for comparative purposes (Figure 7.1).

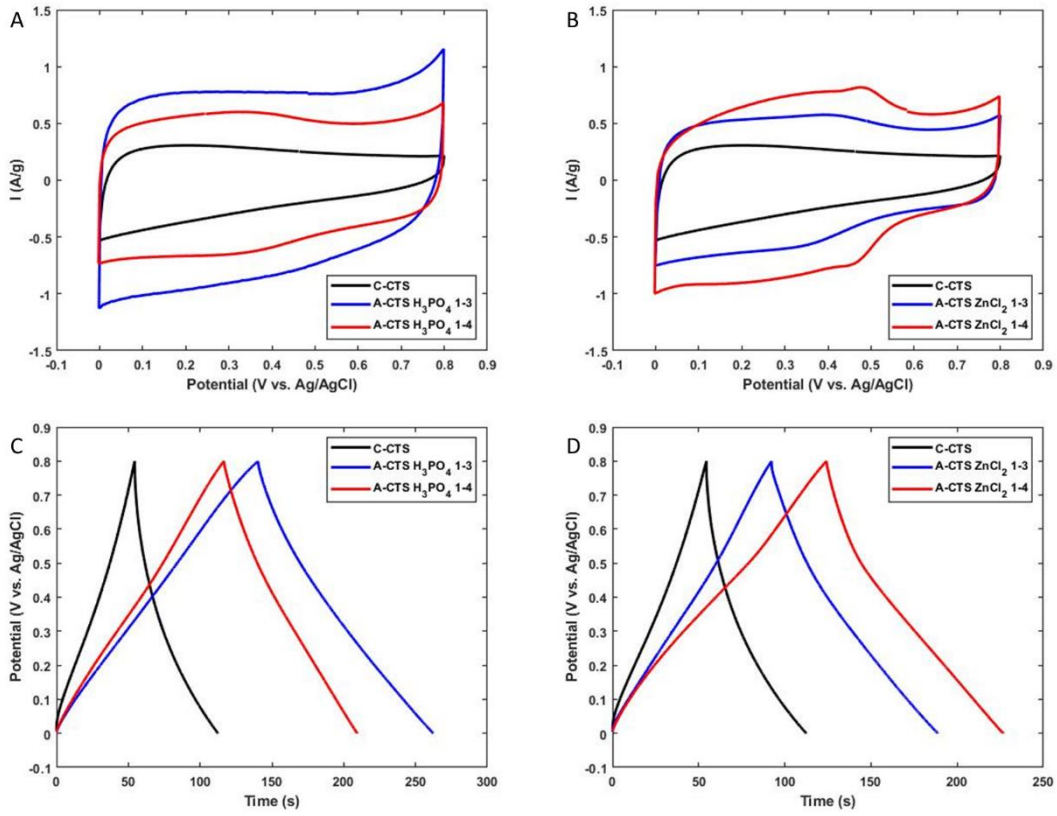

Figure 7.1 CVs recorded on (A) A-CTS H_3PO_4 and (B) A-CTS $ZnCl_2$ electrodes at 5 mV/s, in a H_2SO_4 1.0 M solution as electrolyte. Galvanostatic charge/discharge profiles recorded on (C) A-CTS H_3PO_4 and (D) A-CTS $ZnCl_2$ electrodes at an applied current density of 1 A/g in the same electrolyte. In both cases CV and GCPL measurements), the results recorded on C-CTS are included for comparative purposes.

Figure 7.1 (A) depicts the cyclic voltammograms (CVs) recorded on the C-CTS, A-CTS H_3PO_4 1-3, and A-CTS H_3PO_4 1-4 electrodes at a scan rate of 5 mV/s. As shown, the CVs related to the activated samples exhibit a nearly rectangular shape, characteristic of the formation of the electrical double layer as the main energy storage mechanism on these electrodes. Moreover, the recorded capacitive currents are also higher than those measured on C-CTS as a result of the beneficial impact of the activation process. Similar results are obtained on the A-CTS $ZnCl_2$ 1-3 and A-CTS $ZnCl_2$ 1-4 electrodes (Figure 7.1 (B)). However, both series of samples feature small deviations from strictly capacitive behaviour due to the development of small redox peaks at certain potentials, which can be ascribed to the pseudocapacitive contribution from the different functional groups developed on the surface of the fibres (see XPS characterisation of activated samples in section 6.2). Numerous studies have already highlighted the role of pyrrolic N and pyridinic N on the carbon surface in enhancing pseudocapacitance [74], [280], with these nitrogen-containing functional groups being inherent to CTS itself. Furthermore, oxygen-containing functional groups such as hydroxyl and carboxyl introduced or altered during the activation process also play a part in boosting pseudocapacitance [281]. In addition, residual Zn compounds introduced during $ZnCl_2$ activation may slightly increase pseudocapacitance via redox processes [282]. XPS analysis (section 6.2) confirms the presence of a small amount of Zn-related groups on the fibres surface, which are associated with the small redox peaks or humps observed in Figure 7.1 (B) at 0.3–0.5 V. These peaks indicate the reversible nature of zinc-based redox processes during the charge-discharge cycles.

All these results are corroborated by the galvanostatic cycling with potential limitation (GCPL) measurements (Figures 7.1 (C) and (D)). As expected, the profiles recorded on the A-CTS series of samples exhibit longer charge/discharge times than those recorded on the C-CTS, thus confirming an improved electrochemical performance after the activation process.

Table 7.1 Electrochemical data derived from the GCPL measurements.

Sample	Capacitance (F/g)	ESR (Ω)
C-CTS	50.81	11.00
A-CTS H_3PO_4 1-3	133.67	5.13
A-CTS H_3PO_4 1-4	102.95	5.89
A-CTS $ZnCl_2$ 1-3	100.22	4.42
A-CTS $ZnCl_2$ 1-4	111.86	3.69

In agreement with the BET results presented in the previous chapter, A-CTS samples, although having smaller specific surface areas than C-CTS (A-CTS H_3PO_4 1-3 = 258 m^2/g, A-CTS H_3PO_4 1-4 = 156 m^2/g, A-CTS $ZnCl_2$ 1-3 = 534 m^2/g, and A-CTS $ZnCl_2$ 1-4 = 331 m^2/g vs C-CTS = 568 m^2/g), display better electrochemical behaviours, as is reflected in their higher values of specific capacitances (Table 7.1).

Post-activation enhancement in capacitance can be attributed to several interrelated factors. Firstly, the porosity of the C-CTS predominantly comprises micropores, whereas the activated samples reflect a significant increase in mesopores. Mesopores, due to their larger size, inherently offer advantages over micropores in terms of ion transport and charge storage capability. Thus, a higher amount of mesopores improves ion diffusion to and from the electrode surface, enhancing electrochemical performance by enabling more efficient utilisation of the available surface area for charge storage [283].

Another important parameter indicating the beneficial impact of activation on the subsequent electrochemical performance of A-CTS samples is the equivalent series resistance (ESR). According to Table 7.1 the calculated equivalent series resistance values markedly decreased after activation when compared with C-CTS. These could be related to better electrolyte accessibility to the porous network of activated nanofibers and to enhanced electrode/electrolyte contact as a result of the presence of oxygenated functional groups on the surface of A-CNFs [284].

When comparing A-CTS samples, those activated with $ZnCl_2$ as the activating agent show slightly lower specific capacitances than those activated with H_3PO_4, while also presenting

lower ESR values. For example, A-CTS H_3PO_4 1-3 presents a specific capacitance of 133.67 F/g and an ESR of 5.31 Ω. Conversely, the A-CTS $ZnCl_2$ 1-3 samples, despite having a lower specific capacitance of 100.22 F/g, display a significantly reduced resistance of 4.42 Ω. Although A-CTS H_3PO_4 1-3 has a lower specific surface area than A-CTS $ZnCl_2$ 1-3, they share similar mesopore volumes (refer to Figure 6.9). Additionally, carbon nanofibres (CNFs) activated with H_3PO_4 possess a greater number of oxygen functional groups on their surface. These groups can enhance the affinity of the electrode surface toward the electrolyte for stronger electrostatic interactions and also contribute to pseudocapacitance through redox reactions [280], which may increase the specific capacitance. In contrast, $ZnCl_2$ activation does not significantly increase the number of functional groups. Instead, it modifies the existing oxygen and nitrogen functional groups of the CNFs, thereby potentially optimising its conductivity [223].

When comparing the impact of different activation ratios on electrochemical performance, A-CTS H_3PO_4 1-3 exhibits superior electrochemical properties compared to A-CTS H_3PO_4 1-4; this is attributed to A-CTS H_3PO_4 1-3 having a higher specific surface area. The activation process for A-CTS H_3PO_4 1-4 introduces an excess of oxygen functional groups, leading to over-blocking of pores on the activated carbon nanofibres' (ACNFs) surface, which reduces its specific surface area and adversely affects its final electrochemical performance. Conversely, when activated with $ZnCl_2$, the opposite occurs. Despite A-CTS $ZnCl_2$ 1-4 having a lower specific surface area than A-CTS $ZnCl_2$ 1-3, it possesses a higher mesopore volume, potentially offering advantages in charge storage capability. Furthermore, in terms of surface chemical modification, $ZnCl_2$ mainly alters the existing oxygen and nitrogen functional groups, thereby avoiding excessive blockage of the ACNFs' pore structure.

Due to the better electrochemical performance of A-CTS H_3PO_4 1-3 and A-CTS $ZnCl_2$ 1-4, further analysis of their electrochemical performance was carried out. Figure 7.2 (A) displays the CVs recorded on the A-CTS H_3PO_4 1-3 electrode at increasing scan rates, which maintain the typical rectangular shape related to the double layer formation independently of the selected

v_{scan}, thus corroborating the appropriate capacitive behaviour (rate capability) of this active electrode material. Notably, even at 100 mV/s, the corresponding CV is in agreement with good capacitive retention, including under rapid charge-discharge conditions. The results are similar when assessing the rate capability of the A-CTS $ZnCl_2$ 1-4 electrode (Figure 7.2 (B)), although the pseudocapacitive contribution is more evident.

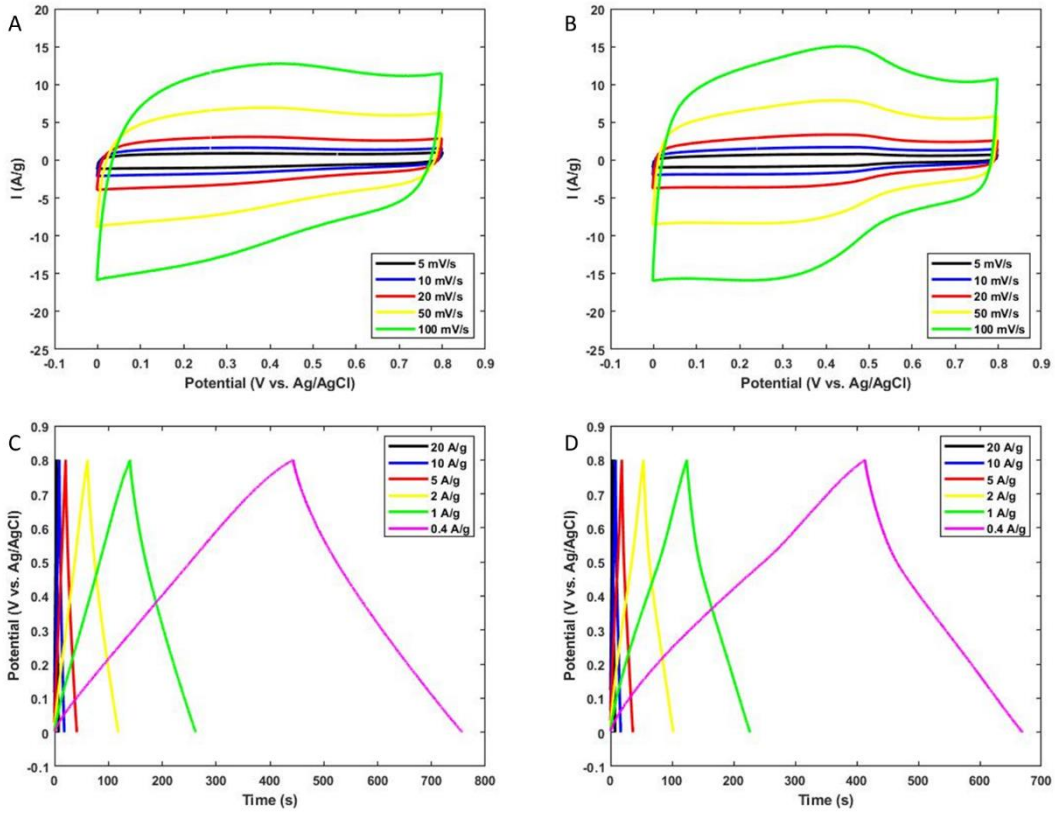

Figure 7.2 CVs recorded at increasing scan rates (ranging between 5–100 mV/s) and using 1.0 M H_2SO_4 solution as electrolyte on (A) A-CTS H_3PO_4 1-3 and (B) A-CTS $ZnCl_2$ 1-4. Galvanostatic charge/discharge profiles recorded on (C) A-CTS H_3PO_4 1-3 and (D) A-CTS $ZnCl_2$ 1-4 electrodes at increasing applied current densities (ranging between 0.4–20 A/g) in the same electrolyte.

The triangular shape and the symmetry of the galvanostatic charge-discharge profiles recorded on the A-CTS H_3PO_4 1-3 at different applied current densities (as shown in Figure 7.2 (C)), corroborate the previously stated good reversibility and fast charge-discharge properties of this electrode. However, in the profiles recorded on A-CTS $ZnCl_2$ 1-4 (Figure 7.2 (D)), there is a

significant difference between the charge and discharge branches regarding longer charging time (410. 3 s vs 258.8 s for the discharge time) when applying 0.4 A/g. The observed decrease in electrode efficiency may be due to the pseudocapacitance generated by redox reactions involving oxygen and Zn-based functional groups [285], [286]. These reactions necessitate prolonged charging times, subsequently leading to reduced electrode efficiency.

As another important parameter to consider when assessing the electrochemical performance of an active electrode material, the long-term performance of the two selected samples was also evaluated. Figure 7.3 illustrates the results of the corresponding cyclability tests performed on both A-CTS H_3PO_4 1-3 and A-CTS $ZnCl_2$ 1-4, applying a constant current of 1 A/g over 2000 cycles (C-CTS is also included for comparison).

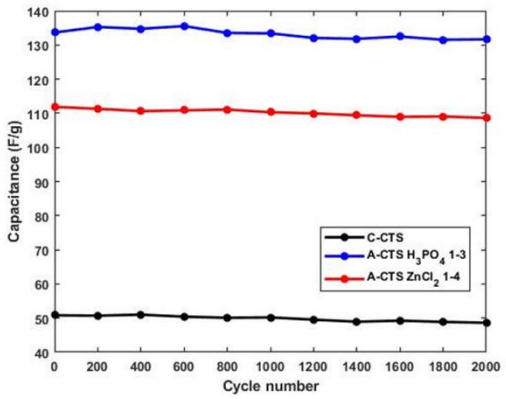

Figure 7.3 Assessment of the long-term performance of the electrodes under evaluation.

According to the results (Figure 7.3), A-CTS H_3PO_4 1-3 demonstrates the best cyclability, maintaining 98.5% of its higher initial capacitance even after 2000 cycles. Although also showing good cyclability with 97.1% capacitance retention, A-CTS ZnCl2 1-4 displays a significantly lower C_{sp} value for the successive charge/discharge cycles, supporting the results in Table 7.1; this can be explained by the physicochemical differences between both active materials, especially in terms of their surface chemistry. As mentioned, CNFs activated with H_3PO_4 are distinguished by a high concentration of oxygen-containing functional groups (e.g., hydroxyl and carboxyl groups) on their surface. These functional groups not only enhance the surface affinity of the CNFs towards the electrolyte, thereby strengthening electrostatic

interactions, they also generate highly reversible pseudocapacitance [273], [287]. However, activation with $ZnCl_2$ does not introduce a significant amount of oxygen-containing functional groups but instead modifies the existing oxygen and nitrogen functional groups on the surface. Furthermore, the pseudocapacitance generated by Zn compounds may lack of stability [70], resulting in slightly inferior cyclic performance of the CNFs activated with $ZnCl_2$. As expected, the C-CTS displays markedly poor capacitive behaviour but also presents appropriate stability as an active electrode material. The high stability of these CNFs' electrodes is primarily associated with their energy storage mechanism. The principal mechanism for energy storage in CNFs is through the formation of the electrical double layer, a type of mechanism where no faradaic processes or phase changes occur during the charging and discharging processes but electrostatic interactions. In consequence, charge storage is mainly related to the development of physical processes involoving the reversible adsorption and desorption of ions at the electrode/electrolyte interface [67]. Consequently, capacitance remains nearly unchanged over extended operational cycles of charge/discharge.

Table 7.2 Specific capacitance values of electrospun carbon nanofibers reported in the literature (these values correspond to carbon electrodes, not to the devices themselves).

Electrode material	**Capacitance (F/g)**	**Electrolyte**	**Applied current density**	**Ref.**
H_3PO_4 activated carbon fibre from PAN	158	1 M H_2SO_4	2 mA	[288]
Hydrothermal activated carbon fibre	28.8	1 M H_2SO_4	1 A/g	[289]
CNTs embedded CNFs (PAN-based)	310	1 M H_2SO_4	100 mA/g	[290]
PAN-based CNFs yarn	145	1 M H_2SO_4	0.2 A/g	[291]
Phosphorus doped CNFs (PAN-based)	228.7	1 M H_2SO_4	0.5 A/g	[292]
Fluorine and nitrogen doped CNFs (PAN-based)	252.6	1 M H_2SO_4	0.5 A/g	[293]
ACNFs from PBI	202.0	1 M H_2SO_4	1 mA/cm^2	[294]
H_3PO_4 activated CTS-based CNFs	133.67	1 M H_2SO_4	1 A/g	This work
$ZnCl_2$ activated CTS-based CNFs	111.86	1 M H_2SO_4	1 A/g	This work

(CNFs = carbon nanofibres; CNTs = carbon nanotubes; ACNFs = activated carbon nanofibres; PAN = polyacrylonitrile; PBI = polybenzimidazole; CTS = chitosan)

Table 7.2 summarizes the specific capacitance values calculated on various electrospun carbon nanofibres acting as electrodes in SCs previously reported in the literature, thus providing a benchmark for comparing the materials developed in this thesis with those from other studies. The materials developed in this work (H_3PO_4 and $ZnCl_2$ activated CTS-based CNFs) show competitive electrochemical performance under similar conditions, comparable to some materials reported in the literature, and are similar to the reported capacitance value of graphene (135 F/g) [295].

7.2 Chapter 7 summary

This chapter primarily discusses the electrochemical performance of CTS-based CNFs activated with H_3PO_4 and $ZnCl_2$ at different impregnation ratios. Post-activation, despite a lower BET surface area, the enhancement of mesoporosity, along with surface chemical modifications, contributed to the development of electrode materials with higher conductivity, displaying pseudocapacitance contribution, and showing and improved hydrophilicity (electrode/electrolyte contact), thereby enhancing the electrochemical performance of the resulting electrodes in SCs. Specifically, for H_3PO_4 activation, the sample impregnated at a 1:3 ratio exhibited superior electrochemical performance, with a capacitance of 133.67 F/g at 1 A/g, and maintained 98.5% of its capacitance after 2000 cycles, indicating an appropriate long-term performance. For $ZnCl_2$ activation, the optimum impregnation ratio is 1:4, which results in a capacitance of 111.86 F/g, with 97.1% capacitance retention after 2000 cycles.

Chapter 8

Summary, conclusions, and future work

8. Summary, conclusions, and future work

8.1 General conclusions

The motivation for this research stems from the urgent demand for sustainable and efficient energy storage solutions. As global energy consumption continues to rise and the adverse impacts of fossil fuels become increasingly evident, the development of environmentally friendly alternatives has become critical. This study addresses this need by focusing on biopolymer-based carbon nanofibres (CNFs) for energy storage devices, particularly supercapacitors. By using sustainable materials such as cellulose, polylactic acid (PLA), and chitosan (CTS), the research aims to create high-performance electrode materials with reduced environmental impact, advancing the transition to green energy technologies.

To achieve this goal, the research systematically investigated the fabrication, stabilisation, and activation processes for biopolymeric nanofibres, leading to several key findings. First, cellulose acetate (CA), PLA, and CTS nanofibres were successfully fabricated via electrospinning with precisely optimised parameters, enabling effective control over nanofibre morphology and diameter. Second, stabilisation processes were refined to ensure the thermal stability and structural integrity of nanofibres during carbonisation, with cellulose and CTS proving to be suitable CNF precursors, while PLA was deemed unsuitable due to its low melting point. Third, chemical activation using H_3PO_4 and $ZnCl_2$ significantly modified the CNFs' surface area, pore structure, and surface chemistry. Finally, CTS-based CNFs demonstrated superior mechanical properties, allowing them to serve as binder-free electrodes in supercapacitors. Notably, the activated CTS CNFs exhibited remarkable electrochemical performance, with a specific capacitance of 133.67 F/g at 1 A/g and excellent cyclability (98.5% retention after 2000 cycles).

This study not only demonstrates the feasibility of biopolymer-based CNFs as sustainable and efficient supercapacitor electrodes but also highlights their potential to transform energy storage

technologies by offering enhanced performance, reduced environmental impact, and a pathway toward greener energy solutions.

8.2 Major findings

The key findings of the thesis are summarised below.

8.2.1 Successful fabrication of diameter and morphology-controlled biopolymeric nanofibres via electrospinning

Biopolymeric nanofibres of cellulose acetate (CA), polylactic acid (PLA), and chitosan (CTS) were successfully fabricated via electrospinning with precise adjustment of process parameters. The study identified suitable concentrations of 17 w/v% for CA, 11 w/v% for PLA, and 8 w/v% for CTS. The most effective spinning flow rate was 1 mL/h, and the needle size was set at 0.933 mm. By fine-tuning these parameters, effective control over the nanofibre diameter and morphology was achieved, enhancing their potential applicability across various fields.

8.2.2 Refinement of the stabilisation process for biopolymeric nanofibres

The stabilisation process for biopolymeric nanofibres was systematically investigated to enhance their thermal stability and maintain structural integrity during carbonisation. The thermal properties of cellulose (from CA deacetylation), PLA, and CTS nanofibres were analysed to determine suitable stabilisation temperatures. However, the low melting point of PLA nanofibres made them challenging to stabilise, deeming them unsuitable as CNF precursors. Once the stabilisation temperatures were identified, the stabilisation conditions for cellulose and CTS nanofibres were refined by adjusting the isothermal times. For cellulose nanofibres, longer isothermal times caused "damaged areas," while shorter times led to inadequate stabilisation. Thus, the stabilisation conditions were set at 200 °C and 240 °C for 3 hours each. For CTS nanofibres, adequate stabilisation was achieved with the shortest isothermal times, chosen as 1 hour at 100 °C and 230 °C, considering the carbon yield and time/energy efficiency. These selected parameters are essential for achieving the structural

integrity of CNFs during carbonisation, a critical step in preparing CNFs for subsequent electrochemical applications.

8.2.3 Effects of H_3PO_4 and $ZnCl_2$ activation on CNFs' physicochemical properties

The specific surface area and surface chemistry of CNFs significantly influence their electrochemical performance. Chemical activation is a method to alter these CNF characteristics. This study explored the effects of H_3PO_4 and $ZnCl_2$ chemical activation on the morphology, specific surface area, and surface chemistry of CNFs before and after activation. After chemical activation, CNF morphology remained largely intact. Nevertheless, CELL-based CNFs exhibited poor mechanical properties post-activation, rendering them unsuitable for final electrochemical performance testing. CTS-based ACNFs, on the other hand, were selected for further characterisation. Regarding specific surface area, CNFs already possessed a high surface area before activation, along with a considerable volume of micropores. However, after activation, there was a decrease in micropore volume and, consequently, a reduction in specific surface area, but an increase in mesopore volume was observed. Moreover, a significant number of oxygen-containing functional groups were introduced onto the CNFs' surface after H_3PO_4 activation. Activation with $ZnCl_2$ also resulted in an increase in oxygen-containing functional groups. The activation improved their wettability, converting them into hydrophilic materials, thereby reinforcing their potential as high-performance electrodes in energy storage applications.

8.2.4 Electrochemical performance of freestanding CTS-Based CNFs as electrodes in supercapacitors

CTS-based CNFs mats, with their suitable mechanical strength and flexibility, can be directly used as electrodes in supercapacitors without binders, offering a sustainable solution for the development of the new generation of electrochemical energy storage devices. Activation notably improves their electrochemical performance due to several factors: the increased

mesopore volume enhances ions transport and facilitates the charge storage through the formation of the electrical double layer, while the development of additional oxygen-containing functional groups promote electrode-electrolyte contact and the appearance of pseudocapacitance contribution. Among the samples, A-CTS H_3PO_4 1-3 showed enhanced electrochemical performance reaching a capacitance of 133.67 F/g at 1 A/g, being retained the 98.5% of this value even after 2000 cycles, indicating excellent cyclability and potential for practical applications in the development of electrochemical energy storage devices.

8.3 Future work recommendations

8.3.1 Exploring the carbonisation process

It is widely recognised that the carbonisation step can significantly influence the specific surface area, pore structure, and surface chemistry of CNFs, which are crucial for their performance in various applications. Future research should focus on examining how different carbonisation parameters, such as temperature, duration, and heating rate, affect the physicochemical properties of CNFs. For example, adjusting the carbonisation temperature may influence the development of micropores and the distribution of surface functional groups, while changes in the heating rate could further impact the overall morphology and surface chemistry. A more comprehensive study incorporating various carbonisation conditions and characterisation techniques, such as BET analysis, Raman spectroscopy, and X-ray photoelectron spectroscopy (XPS), could provide deeper insights into controlling the material properties. Additionally, investigating the effects of different gas atmospheres (e.g., nitrogen, argon, or mixtures with reactive gases) during carbonisation could offer new ways to tailor CNFs for specific electrochemical applications, such as supercapacitors or batteries.

8.3.2 Investigating sodium thiosulfate as an eco-friendly activating agent for ACNFs production

This thesis employed chemical activation for producing ACNF mats, a widely used methodology due to its ability to modify the specific surface area, pore size distribution, and

surface chemistry of the resulting materials. However, a significant drawback of chemical activation is the negative environmental impact and residual presence of commonly used activating agents. Furthermore, preserving the integrity of ACNF mats during the washing step without mechanical/magnetic stirring or boiling water adds further challenges to required post-treatments.

To address these concerns, future work should explore alternative "green" activating agents. For instance, sodium thiosulfate has been suggested as a potential eco-friendly activating agent due to its lower environmental impact and minimal residue generation [296], [297]. Such approach could significantly reduce the need for intensive post-treatments, while also aligning with sustainable and environmentally conscious research practices. However, further studies are needed to evaluate the efficiency of these green activating agents in producing CNF mats with suitable physicochemical properties to be used as appropriate active electrode materials in supercapacitors.

8.3.3 Investigating the effects of GO incorporation in CNFs composites

Incorporating graphene oxide (GO) into carbon nanofibre (CNF) composites can enhance the material's electrical conductivity, as GO can convert into more conductive graphene (rGO, reduced graphene oxide) during the carbonisation process. This addition can also increase the surface area and the number of electrochemically active sites, further improving the electrochemical performance of supercapacitor electrodes by facilitating the double layer formation or by the development of pseudocapacitance. Future research should investigate the effects of varying amounts of GO on the rheological properties of the electrospinning solution, such as viscosity and flow behaviour. To ensure uniform dispersion of GO in the solution, experiments with different ultrasonication durations should be conducted to identify the optimal conditions. Furthermore, it will be necessary to refine electrospinning parameters, such as voltage, flow rate, and collector distance, and examine how these factors influence the fibre diameter, morphology, and structural uniformity. Additionally, studies should focus on the

physicochemical properties of the composites, such as surface chemistry, porosity, and specific surface area, as well as their overall electrochemical performance.

8.3.4 Performance evaluation of the ACNFs mats in two-electrode configuration

To further evaluate the electrochemical performance of the materials developed in this thesis as electrodes in SCs, future work should focus on assessing their characterisation under realistic operational conditions. Specifically, testing in a two-electrode configuration is essential, as it closely replicates the working environment of commercial SC devices. Unlike the commonly used three-electrode setup, which primarily provides preliminary results into the intrinsic material properties, the two-electrode configuration allows for a more comprehensive evaluation of the material's energy storage performance, including specific capacitance, assessment of the long-term performance and energy/power density calculations.

Moreover, carrying out such measurements will enable a reliable comparison of the developed materials with those previously in the literature as SC materials. This approach can highlight the advantages or limitations of the ACNFs produced in this work, providing a clearer perspective on their competitiveness and suitable application in the development of electrochemical energy storage devices. Incorporating these findings will not only validate the applicability of the developed materials but also guide further optimisation efforts towards achieving active electrode materials with superior performance.

Reference

[1] IEA, "World Energy Outlook 2021 - revised version October 2021," 2021. [Online]. Available: www.iea.org/weo.

[2] IEA, "World Energy World Energy," 2017, [Online]. Available: https://www.iea.org/reports/world-energy-outlook-2017.

[3] H. Ibrahim, A. Ilinca, and J. Perron, "Energy storage systems—Characteristics and comparisons," *Renew. Sustain. energy Rev.*, vol. 12, no. 5, pp. 1221–1250, 2008.

[4] H. D. Yoo, E. Markevich, G. Salitra, D. Sharon, and D. Aurbach, "On the challenge of developing advanced technologies for electrochemical energy storage and conversion," *Mater. Today*, vol. 17, no. 3, pp. 110–121, 2014, doi: 10.1016/j.mattod.2014.02.014.

[5] M. Skyllas-Kazacos, M. H. Chakrabarti, S. A. Hajimolana, F. S. Mjalli, and M. Saleem, "Progress in Flow Battery Research and Development," *J. Electrochem. Soc.*, vol. 158, no. 8, p. R55, 2011, doi: 10.1149/1.3599565.

[6] R. Shapira, G. Daniel Nessim, T. Zimrin, and D. Aurbach, "Towards promising electrochemical technology for load leveling applications: extending cycle life of lead acid batteries by the use of carbon nano-tubes (CNTs)," *Energy Environ. Sci.*, vol. 6, pp. 587–594, 2013, doi: 10.1039/c2ee22970f.

[7] B. Dunn, H. Kamath, and J. M. Tarascon, "Electrical energy storage for the grid: A battery of choices," *Science (80-.).*, vol. 334, no. 6058, pp. 928–935, 2011, doi: 10.1126/science.1212741.

[8] H. Zhang *et al.*, "Recent progress in advanced electrode materials, separators and electrolytes for lithium batteries," *J. Mater. Chem. A*, vol. 6, no. 42, pp. 20564–20620, 2018, doi: 10.1039/C8TA05336G.

[9] J. P. Pender *et al.*, "Electrode Degradation in Lithium-Ion Batteries," *ACS Nano*, vol.

14, no. 2, pp. 1243–1295, 2020, doi: 10.1021/acsnano.9b04365.

[10] A. Mishra *et al.*, "Electrode materials for lithium-ion batteries," *Mater. Sci. Energy Technol.*, vol. 1, no. 2, pp. 182–187, 2018.

[11] P. Alotto, M. Guarnieri, F. Moro, and A. Stella, "Redox Flow Batteries for large scale energy storage," *2012 IEEE Int. Energy Conf. Exhib. ENERGYCON 2012*, no. April 2014, pp. 293–298, 2012, doi: 10.1109/EnergyCon.2012.6347770.

[12] K. J. Kim, M. S. Park, Y. J. Kim, J. H. Kim, S. X. Dou, and M. Skyllas-Kazacos, "A technology review of electrodes and reaction mechanisms in vanadium redox flow batteries," *J. Mater. Chem. A*, vol. 3, no. 33, pp. 16913–16933, 2015, doi: 10.1039/c5ta02613j.

[13] A. Kirubakaran, S. Jain, and R. K. Nema, "A review on fuel cell technologies and power electronic interface," *Renew. Sustain. Energy Rev.*, vol. 13, no. 9, pp. 2430–2440, Dec. 2009, doi: 10.1016/J.RSER.2009.04.004.

[14] H. Tsuchiya and O. Kobayashi, "Mass production cost of PEM fuel cell by learning curve," *Int. J. Hydrogen Energy*, vol. 29, no. 10, pp. 985–990, Aug. 2004, doi: 10.1016/J.IJHYDENE.2003.10.011.

[15] S. F. Tie and C. W. Tan, "A review of energy sources and energy management system in electric vehicles," *Renew. Sustain. energy Rev.*, vol. 20, pp. 82–102, 2013.

[16] F. Tsang, J. S. Pedersen, S. Wooding, and D. Potoglou, "Bringing the electric vehicle to the mass market," 2012, [Online]. Available: http://www.rand.org/pubs/working_papers/WR775.html.

[17] Z. P. Cano *et al.*, "Batteries and fuel cells for emerging electric vehicle markets," *Nat. Energy*, vol. 3, no. 4, pp. 279–289, 2018, doi: 10.1038/s41560-018-0108-1.

[18] L. Kouchachvili, W. Yaïci, and E. Entchev, "Hybrid battery/supercapacitor energy storage system for the electric vehicles," *J. Power Sources*, vol. 374, pp. 237–248, 2018.

[19] P. García, J. P. Torreglosa, L. M. Fernández, and F. Jurado, "Control strategies for high-power electric vehicles powered by hydrogen fuel cell, battery and supercapacitor," *Expert Syst. Appl.*, vol. 40, no. 12, pp. 4791–4804, 2013.

[20] K. Maneesut and U. Supatti, "Reviews of supercapacitor cell voltage equalizer topologies for EVs," in *2017 14th International Conference on Electrical Engineering/Electronics, Computer, Telecommunications and Information Technology (ECTI-CON)*, 2017, pp. 608–611.

[21] W. Hu *et al.*, "Review of Printed Electrodes for Flexible Devices," 2019, doi: 10.3389/fmats.2018.00077.

[22] S. Jingjing, G. Xing, C. Renjie, and W. Feng, "Recent progress in flexible battery," *Prog. Chem.*, vol. 28, no. 4, p. 577, 2016.

[23] L. Dong *et al.*, "Flexible electrodes and supercapacitors for wearable energy storage: a review by category," *J. Mater. Chem. A*, vol. 4, no. 13, pp. 4659–4685, 2016.

[24] B. B. McKeon, J. Furukawa, and S. Fenstermacher, "Advanced lead-acid batteries and the development of grid-scale energy storage systems," *Proc. IEEE*, vol. 102, no. 6, pp. 951–963, 2014, doi: 10.1109/JPROC.2014.2316823.

[25] A. Al-Haj Hussein and I. Batarseh, "A review of charging algorithms for nickel and lithium battery chargers," *IEEE Trans. Veh. Technol.*, vol. 60, no. 3, pp. 830–838, 2011, doi: 10.1109/TVT.2011.2106527.

[26] P. Gao *et al.*, "Cadmium hydroxide nanowires-new high capacity Ni-Cd battery anode materials without memory effect," *J. Mater. Chem.*, vol. 22, no. 28, pp. 13922–13924, 2012, doi: 10.1039/c2jm33169a.

[27] M. Wakihara, "Recent developments in lithium ion batteries," *Mater. Sci. Eng. R Reports*, vol. 33, no. 4, pp. 109–134, 2001, doi: 10.1016/S0927-796X(01)00030-4.

[28] Y. Zhao *et al.*, "High-Performance Asymmetric Supercapacitors Based on Multilayer

MnO2/Graphene Oxide Nanoflakes and Hierarchical Porous Carbon with Enhanced Cycling Stability," *Small*, vol. 11, no. 11, pp. 1310–1319, 2015, doi: 10.1002/smll.201401922.

[29] R. Berenguer *et al.*, "Biomass-derived binderless fibrous carbon electrodes for ultrafast energy storage," *Green Chem.*, vol. 18, no. 6, pp. 1506–1515, 2016, doi: 10.1039/c5gc02409a.

[30] H. Lai *et al.*, "Mesostructured NiO/Ni composites for high-performance electrochemical energy storage," *Energy Environ. Sci.*, vol. 9, no. 6, pp. 2053–2060, 2016, doi: 10.1039/c6ee00603e.

[31] D. P. Dubal, O. Ayyad, V. Ruiz, and P. Gomez-Romero, "Hybrid energy storage: the merging of battery and supercapacitor chemistries," *Chem. Soc. Rev.*, vol. 44, no. 7, pp. 1777–1790, 2015, doi: 10.1002/chin.201522308.

[32] P. Ragupathy, S. D. Bhat, and N. Kalaiselvi, "Electrochemical energy storage and conversion: An overview," *Wiley Interdiscip. Rev. Energy Environ.*, vol. 12, no. 2, p. e464, 2023.

[33] A. B. Kaul, "Two-dimensional layered materials: Structure, properties, and prospects for device applications," *J. Mater. Res.*, vol. 29, no. 3, pp. 348–361, 2014, doi: 10.1557/jmr.2014.6.

[34] J. Liang *et al.*, "Recent advances in electrospun nanofibers for supercapacitors," *J. Mater. Chem. A*, vol. 8, no. 33, pp. 16747–16789, 2020, doi: 10.1039/d0ta05100d.

[35] L. Yue *et al.*, "Recent advances in electrospun one-dimensional carbon nanofiber structures/heterostructures as anode materials for sodium ion batteries," *J. Mater. Chem. A*, vol. 8, no. 23, pp. 11493–11510, 2020.

[36] J. N. Tiwari, R. N. Tiwari, and K. S. Kim, "Zero-dimensional, one-dimensional, two-dimensional and three-dimensional nanostructured materials for advanced

electrochemical energy devices," *Prog. Mater. Sci.*, vol. 57, no. 4, pp. 724–803, 2012.

[37] M. Ge *et al.*, "A review of one-dimensional TiO 2 nanostructured materials for environmental and energy applications," *J. Mater. Chem. A*, vol. 4, no. 18, pp. 6772–6801, 2016.

[38] A. G. Dumanlı and A. H. Windle, "Carbon fibres from cellulosic precursors: A review," *Journal of Materials Science*, vol. 47, no. 10. pp. 4236–4250, 2012, doi: 10.1007/s10853-011-6081-8.

[39] W. Xu, B. Xin, and X. Yang, "Carbonization of electrospun polyacrylonitrile (PAN)/cellulose nanofibril (CNF) hybrid membranes and its mechanism," *Cellulose*, vol. 27, no. 7, pp. 3789–3804, 2020, doi: 10.1007/s10570-020-03006-y.

[40] M. C. Paiva, P. Kotasthane, D. D. Edie, and A. A. Ogale, "UV stabilization route for melt-processible PAN-based carbon fibers," *Carbon N. Y.*, vol. 41, no. 7, pp. 1399–1409, 2003, doi: 10.1016/S0008-6223(03)00041-1.

[41] O. P. Bahl, Z. Shen, J. G. Lavin, and R. A. Ross, *Manufacture of carbon fibers*, vol. 3, no. 1. Marcel Dekker: New York, 1998.

[42] J. Cai *et al.*, "High-Performance Supercapacitor Electrode Materials from Cellulose-Derived Carbon Nanofibers," *ACS Appl. Mater. Interfaces*, vol. 7, no. 27, pp. 14946–14953, Jul. 2015, doi: 10.1021/acsami.5b03757.

[43] S. X. Wang, L. Yang, L. P. Stubbs, X. Li, and C. He, "Lignin-derived fused electrospun carbon fibrous mats as high performance anode materials for lithium ion batteries," *ACS Appl. Mater. Interfaces*, vol. 5, no. 23, pp. 12275–12282, 2013, doi: 10.1021/am4043867.

[44] R. Nayak, R. Padhye, I. L. Kyratzis, Y. B. Truong, and L. Arnold, "Recent advances in nanofibre fabrication techniques," *Text. Res. J.*, vol. 82, no. 2, pp. 129–147, 2012, doi: 10.1177/0040517511424524.

[45] P. Samyn, A. Barhoum, and A. Dufresne, "Review: nanoparticles and nanostructured materials in papermaking," *J Mater Sci*, vol. 53, pp. 146–184, 2018, doi: 10.1007/s10853-017-1525-4.

[46] K. Mohamed, "Melt Spinning BT - Encyclopedia of Membranes," E. Drioli and L. Giorno, Eds. Berlin, Heidelberg: Springer Berlin Heidelberg, 2015, pp. 1–3.

[47] N. Bhardwaj and S. C. Kundu, "Electrospinning: A fascinating fiber fabrication technique," *Biotechnol. Adv.*, vol. 28, no. 3, pp. 325–347, 2010, doi: 10.1016/j.biotechadv.2010.01.004.

[48] R. Dersch, T. Liu, A. K. Schaper, A. Greiner, and J. H. Wendorff, "Electrospun nanofibers: Internal structure and intrinsic orientation," *J. Polym. Sci. Part A Polym. Chem.*, vol. 41, no. 4, pp. 545–553, 2003, doi: 10.1002/pola.10609.

[49] H. Yan, L. Liu, and Z. Zhang, "Alignment of electrospun nanofibers using dielectric materials," *Appl. Phys. Lett.*, vol. 95, no. 14, p. 143114, 2009.

[50] D. Li, Y. Wang, and Y. Xia, "Electrospinning of polymeric and ceramic nanofibers as uniaxially aligned arrays," *Nano Lett.*, vol. 3, no. 8, pp. 1167–1171, 2003.

[51] Z. Sun, E. Zussman, A. L. Yarin, J. H. Wendorff, and A. Greiner, "Compound core–shell polymer nanofibers by co-electrospinning," *Adv. Mater.*, vol. 15, no. 22, pp. 1929–1932, 2003.

[52] J. S. Park, "Electrospinning and its applications," *Adv. Nat. Sci. Nanosci. Nanotechnol.*, vol. 1, no. 4, 2010, doi: 10.1088/2043-6262/1/4/043002.

[53] K. Aup-Ngoen and M. Noipitak, "Effect of carbon-rich biochar on mechanical properties of PLA-biochar composites," *Sustain. Chem. Pharm.*, vol. 15, p. 100204, 2020.

[54] N. Angin, M. Ertas, S. Caylak, and M. S. Fidan, "Thermal and electrical behaviors of activated carbon-filled PLA/PP hybrid biocomposites," *Sustain. Mater. Technol.*, vol.

37, p. e00655, 2023.

[55] B. Tar and A. Fayed, "An overview of the fundamentals of battery chargers," *2016 IEEE 59th Int. Midwest Symp. Circuits Syst. (MWSCAS). IEEE,* pp. 1–4, 2016, doi: 10.1109/MWSCAS.2016.7870048.

[56] R. Santhanam, P. Jones, A. Sumana, and B. Rambabu, "Influence of lithium content on high rate cycleability of layered Li1+xNi0.30Co0.30Mn0.40O2 cathodes for high power lithium-ion batteries," *J. Power Sources*, vol. 195, no. 21, pp. 7391–7396, Nov. 2010, doi: 10.1016/J.JPOWSOUR.2010.06.004.

[57] X. H. Rui, N. Ding, J. Liu, C. Li, and C. H. Chen, "Analysis of the chemical diffusion coefficient of lithium ions in Li3V2(PO4)3 cathode material," *Electrochim. Acta*, vol. 55, no. 7, pp. 2384–2390, Feb. 2010, doi: 10.1016/J.ELECTACTA.2009.11.096.

[58] D. K. Kim *et al.*, "Spinel LiMn2O4 nanorods as lithium ion battery cathodes," *Nano Lett.*, vol. 8, no. 11, pp. 3948–3952, 2008.

[59] A. Yamada and M. Tanaka, "Jahn-Teller structural phase transition around 280K in LiMn2O4," *Mater. Res. Bull.*, vol. 30, no. 6, pp. 715–721, 1995.

[60] D. Ouyang, M. Chen, Q. Huang, J. Weng, Z. Wang, and J. Wang, "A Review on the thermal hazards of the lithium-ion battery and the corresponding countermeasures," *Appl. Sci.*, vol. 9, no. 12, 2019, doi: 10.3390/app9122483.

[61] W. Huo, H. He, and F. Sun, "Electrochemical-thermal modeling for a ternary lithium ion battery during discharging and driving cycle testing," *RSC Adv.*, vol. 5, no. 71, pp. 57599–57607, 2015, doi: 10.1039/c5ra09018k.

[62] B. Zhang, F. Kang, J. M. Tarascon, and J. K. Kim, "Recent advances in electrospun carbon nanofibers and their application in electrochemical energy storage," *Prog. Mater. Sci.*, vol. 76, pp. 319–380, 2016, doi: 10.1016/j.pmatsci.2015.08.002.

[63] C. Kim *et al.*, "Fabrication of electrospinning-derived carbon nanofiber webs for the

anode material of lithium-ion secondary batteries," *Adv. Funct. Mater.*, vol. 16, no. 18, pp. 2393–2397, 2006, doi: 10.1002/adfm.200500911.

[64] B. Zhang *et al.*, "Correlation between atomic structure and electrochemical performance of anodes made from electrospun carbon nanofiber films," *Adv. Energy Mater.*, vol. 4, no. 7, pp. 1–9, 2014, doi: 10.1002/aenm.201301448.

[65] O. Haas and E. J. Cairns, *Electrochemical energy storage*, vol. 95, no. 46. 1999.

[66] M. E. Şahin, F. Blaabjerg, and A. Sangwongwanich, "A Comprehensive Review on Supercapacitor Applications and Developments," *Energies*, vol. 15, no. 3, pp. 1–26, 2022, doi: 10.3390/en15030674.

[67] P. Simon and Y. Gogotsi, "Materials for electrochemical capacitors," *Nature Materials*, vol. 7, no. 11. Nature Publishing Group, pp. 845–854, Nov. 16, 2008, doi: 10.1038/nmat2297.

[68] B. Conway, *Electrochemical supercapacitors: scientific fundamentals and technological applications*. 2013.

[69] Y. Jiang and J. Liu, "Definitions of pseudocapacitive materials: a brief review," *Energy Environ. Mater.*, vol. 2, no. 1, pp. 30–37, 2019.

[70] H. W. Park and K. C. Roh, "Recent advances in and perspectives on pseudocapacitive materials for supercapacitors–a review," *J. Power Sources*, vol. 557, p. 232558, 2023.

[71] J. Yan, Q. Wang, T. Wei, and Z. Fan, "Recent advances in design and fabrication of electrochemical supercapacitors with high energy densities," *Adv. Energy Mater.*, vol. 4, no. 4, p. 1300816, 2014.

[72] M. Yu *et al.*, "Three dimensional architectures: design, assembly and application in electrochemical capacitors," *J. Mater. Chem. A*, vol. 3, no. 31, pp. 15792–15823, 2015.

[73] H. Qi *et al.*, "Hierarchical nanocarbon-MnO2 electrodes for enhanced electrochemical

capacitor performance," *Energy Storage Mater.*, vol. 16, pp. 607–618, 2019.

[74] A. Ilnicka *et al.*, "Combined effect of nitrogen-doped functional groups and porosity of porous carbons on electrochemical performance of supercapacitors," *Sci. Rep.*, vol. 11, no. 1, p. 18387, 2021.

[75] C. Qiu, L. Jiang, Y. Gao, and L. Sheng, "Effects of Oxygen-Containing Functional Groups on Carbon Materials in Supercapacitors: A Review," *Mater. Des.*, p. 111952, 2023.

[76] S. Hajiaghasi, A. Salemnia, and M. Hamzeh, "Hybrid energy storage system for microgrids applications: A review," *J. Energy Storage*, vol. 21, no. November 2018, pp. 543–570, 2019, doi: 10.1016/j.est.2018.12.017.

[77] G. G. Amatucci, F. Badway, A. Du Pasquier, and T. Zheng, "An asymmetric hybrid nonaqueous energy storage cell," *J. Electrochem. Soc.*, vol. 148, no. 8, p. A930, 2001.

[78] V. Khomenko, E. Raymundo-Piñero, and F. Béguin, "High-energy density graphite/AC capacitor in organic electrolyte," *J. Power Sources*, vol. 177, no. 2, pp. 643–651, 2008, doi: 10.1016/j.jpowsour.2007.11.101.

[79] T. Brousse, M. Toupin, and D. Belanger, "A hybrid activated carbon-manganese dioxide capacitor using a mild aqueous electrolyte," *J. Electrochem. Soc.*, vol. 151, no. 4, p. A614, 2004.

[80] A. M. Abioye and F. N. Ani, "Recent development in the production of activated carbon electrodes from agricultural waste biomass for supercapacitors: A review," *Renew. Sustain. Energy Rev.*, vol. 52, pp. 1282–1293, 2015, doi: 10.1016/j.rser.2015.07.129.

[81] A. M. Abioye and F. N. Ani, "Recent development in the production of activated carbon electrodes from agricultural waste biomass for supercapacitors: A review," *Renew. Sustain. energy Rev.*, vol. 52, pp. 1282–1293, 2015.

[82] P. Dubey, V. Shrivastav, P. H. Maheshwari, and S. Sundriyal, "Recent advances in

biomass derived activated carbon electrodes for hybrid electrochemical capacitor applications: Challenges and opportunities," *Carbon N. Y.*, vol. 170, pp. 1–29, 2020.

[83] W.-H. Qu, Y.-Y. Xu, A.-H. Lu, X.-Q. Zhang, and W.-C. Li, "Converting biowaste corncob residue into high value added porous carbon for supercapacitor electrodes," *Bioresour. Technol.*, vol. 189, pp. 285–291, 2015.

[84] M. Sevilla and R. Mokaya, "Energy storage applications of activated carbons: supercapacitors and hydrogen storage," *Energy Environ. Sci.*, vol. 7, no. 4, pp. 1250–1280, 2014.

[85] Y. Gong, H. Wang, Z. Wei, L. Xie, and Y. Wang, "An efficient way to introduce hierarchical structure into biomass-based hydrothermal carbonaceous materials," *ACS Sustain. Chem. Eng.*, vol. 2, no. 10, pp. 2435–2441, 2014.

[86] S. C. G.-T. P. and C.-M. H. Kuan-Ching Lee, Mitchell Shyan Wei Lim, Zhong-Yun Hong, "Coconut Shell-Derived Activated Carbon for High-Performance Solid-State Supercapacitors," *Energies*, vol. 14, no. 15, p. 4546, 2021.

[87] D. Saha *et al.*, "Studies on supercapacitor electrode material from activated lignin-derived mesoporous carbon," *Langmuir*, vol. 30, no. 3, pp. 900–910, 2014, doi: 10.1021/la404112m.

[88] Z. Li *et al.*, "Carbonized chicken eggshell membranes with 3D architectures as high-performance electrode materials for supercapacitors," *Adv. Energy Mater.*, vol. 2, no. 4, pp. 431–437, 2012.

[89] S. Gao *et al.*, "Large scale production of biomass-derived N-doped porous carbon spheres for oxygen reduction and supercapacitors," *J. Mater. Chem. A*, vol. 2, no. 10, pp. 3317–3324, 2014.

[90] E. Raymundo-Piñero, M. Cadek, and F. Béguin, "Tuning carbon materials for supercapacitors by direct pyrolysis of seaweeds," *Adv. Funct. Mater.*, vol. 19, no. 7, pp.

1032–1039, 2009.

[91] N. Subramanian and B. Viswanathan, "Nitrogen-and oxygen-containing activated carbons from sucrose for electrochemical supercapacitor applications," *RSC Adv.*, vol. 5, no. 77, pp. 63000–63011, 2015.

[92] Y. Ren *et al.*, "Biomass-derived three-dimensional porous N-doped carbonaceous aerogel for efficient supercapacitor electrodes," *Rsc Adv.*, vol. 4, no. 45, pp. 23412–23419, 2014.

[93] E. Frackowiak, "Carbon materials for supercapacitor application," *Phys. Chem. Chem. Phys.*, vol. 9, no. 15, pp. 1774–1785, 2007, doi: 10.1039/b618139m.

[94] S. Rathinavel, K. Priyadharshini, and D. Panda, "A review on carbon nanotube: An overview of synthesis, properties, functionalization, characterization, and the application," *Mater. Sci. Eng. B*, vol. 268, p. 115095, 2021.

[95] C. Niu, E. K. Sichel, R. Hoch, D. Moy, and H. Tennent, "High power electrochemical capacitors based on carbon nanotube electrodes," *Appl. Phys. Lett.*, vol. 70, no. 11, pp. 1480–1482, 1997.

[96] J. N. Barisci, G. G. Wallace, and R. H. Baughman, "Electrochemical characterization of single-walled carbon nanotube electrodes," *J. Electrochem. Soc.*, vol. 147, no. 12, p. 4580, 2000.

[97] H. Zhang, G. P. Cao, and Y. S. Yang, "Using a cut–paste method to prepare a carbon nanotube fur electrode," *Nanotechnology*, vol. 18, no. 19, p. 195607, 2007.

[98] E. Frackowiak, K. Metenier, V. Bertagna, and F. Beguin, "Supercapacitor electrodes from multiwalled carbon nanotubes," *Appl. Phys. Lett.*, vol. 77, no. 15, pp. 2421–2423, 2000.

[99] H.-J. Ahn, J. I. Sohn, Y.-S. Kim, H.-S. Shim, W. B. Kim, and T.-Y. Seong, "Electrochemical capacitors fabricated with carbon nanotubes grown within the pores

of anodized aluminum oxide templates," *Electrochem. commun.*, vol. 8, no. 4, pp. 513–516, 2006.

[100] H. Pan, J. Li, and Y. Feng, "Carbon nanotubes for supercapacitor," *Nanoscale Res. Lett.*, vol. 5, pp. 654–668, 2010.

[101] E. Frackowiak, S. Delpeux, K. Jurewicz, K. Szostak, D. Cazorla-Amoros, and F. Beguin, "Enhanced capacitance of carbon nanotubes through chemical activation," *Chem. Phys. Lett.*, vol. 361, no. 1–2, pp. 35–41, 2002.

[102] J. Y. Lee, K. H. An, J. K. Heo, and Y. H. Lee, "Fabrication of supercapacitor electrodes using fluorinated single-walled carbon nanotubes," *J. Phys. Chem. B*, vol. 107, no. 34, pp. 8812–8815, 2003.

[103] H. Pan, Y. P. Feng, and J. Y. Lin, "Ab initio study of F-and Cl-functionalized single wall carbon nanotubes," *J. Phys. Condens. Matter*, vol. 18, no. 22, p. 5175, 2006.

[104] C. Zhou, S. Kumar, C. D. Doyle, and J. M. Tour, "Functionalized single wall carbon nanotubes treated with pyrrole for electrochemical supercapacitor membranes," *Chem. Mater.*, vol. 17, no. 8, pp. 1997–2002, 2005.

[105] B.-J. Yoon, S.-H. Jeong, K.-H. Lee, H. S. Kim, C. G. Park, and J. H. Han, "Electrical properties of electrical double layer capacitors with integrated carbon nanotube electrodes," *Chem. Phys. Lett.*, vol. 388, no. 1–3, pp. 170–174, 2004.

[106] A. K. Geim and K. S. Novoselov, "The rise of graphene," *Nat. Mater.*, vol. 6, no. 3, pp. 183–191, 2007.

[107] B. Ekdahl, "Progress in top-down production of graphene," 2021, doi: 10.6069/dt5dbd9r.

[108] X. Li *et al.*, "Large-area synthesis of high-quality and uniform graphene films on copper foils," *Science (80-.).*, vol. 324, no. 5932, pp. 1312–1314, 2009.

[109] W. Gao, "The chemistry of graphene oxide," *Graphene oxide Reduct. recipes, Spectrosc.*

Appl., pp. 61–95, 2015.

[110] S. Tamang, S. Rai, R. Bhujel, N. K. Bhattacharyya, B. P. Swain, and J. Biswas, "A concise review on GO, rGO and metal oxide/rGO composites: Fabrication and their supercapacitor and catalytic applications," *J. Alloys Compd.*, p. 169588, 2023.

[111] K. Erickson, R. Erni, Z. Lee, N. Alem, W. Gannett, and A. Zettl, "Determination of the local chemical structure of graphene oxide and reduced graphene oxide," *Adv. Mater.*, vol. 22, no. 40, pp. 4467–4472, 2010.

[112] J. C. Meyer, A. K. Geim, M. I. Katsnelson, K. S. Novoselov, T. J. Booth, and S. Roth, "The structure of suspended graphene sheets," *Nature*, vol. 446, no. 7131, pp. 60–63, 2007.

[113] B. Rajagopalan and J. S. Chung, "Reduced chemically modified graphene oxide for supercapacitor electrode," *Nanoscale Res. Lett.*, vol. 9, no. 1, pp. 1–10, 2014, doi: 10.1186/1556-276X-9-535.

[114] D. Sun, X. Yan, J. Lang, and Q. Xue, "High performance supercapacitor electrode based on graphene paper via flame-induced reduction of graphene oxide paper," *J. Power Sources*, vol. 222, pp. 52–58, 2013.

[115] C. Kim and K. S. Yang, "Electrochemical properties of carbon nanofiber web as an electrode for supercapacitor prepared by electrospinning," *Appl. Phys. Lett.*, vol. 83, no. 6, pp. 1216–1218, 2003.

[116] C. Kim *et al.*, "Self-sustained thin Webs consisting of porous carbon nanofibers for supercapacitors via the electrospinning of polyacrylonitrile solutions containing zinc chloride," *Adv. Mater.*, vol. 19, no. 17, pp. 2341–2346, 2007, doi: 10.1002/adma.200602184.

[117] C. Tran and V. Kalra, "Fabrication of porous carbon nanofibers with adjustable pore sizes as electrodes for supercapacitors," *J. Power Sources*, vol. 235, pp. 289–296, 2013,

doi: 10.1016/j.jpowsour.2013.01.080.

[118] B. H. Kim and K. S. Yang, "Enhanced electrical capacitance of tetraethyl orthosilicate-derived porous carbon nanofibers produced via electrospinning," *J. Electroanal. Chem.*, vol. 714–715, pp. 92–96, 2014, doi: 10.1016/j.jelechem.2013.12.019.

[119] B. H. Kim and K. S. Yang, "Enhanced electrical capacitance of porous carbon nanofibers derived from polyacrylonitrile and boron trioxide," *Electrochim. Acta*, vol. 88, pp. 597–603, 2013, doi: 10.1016/j.electacta.2012.10.123.

[120] X. Yan, Y. Liu, X. Fan, X. Jia, Y. Yu, and X. Yang, "Nitrogen/phosphorus co-doped nonporous carbon nanofibers for high-performance supercapacitors," *J. Power Sources*, vol. 248, pp. 745–751, 2014, doi: 10.1016/j.jpowsour.2013.09.129.

[121] Z. Zhou and X.-F. Wu, "Graphene-beaded carbon nanofibers for use in supercapacitor electrodes: Synthesis and electrochemical characterization," *J. Power Sources*, vol. 222, pp. 410–416, 2013.

[122] B.-H. Kim, "MnO2 decorated on electrospun carbon nanofiber/graphene composites as supercapacitor electrode materials," *Synth. Met.*, vol. 219, pp. 115–123, 2016.

[123] L. Zhang, Y. Chen, Q. Liu, W. Deng, Y. Yue, and F. Meng, "Ultrathin flexible electrospun carbon nanofibers reinforced graphene microgasbags films with three-dimensional conductive network toward synergetic enhanced electromagnetic interference shielding," *J. Mater. Sci. Technol.*, vol. 111, pp. 57–65, 2022.

[124] G. M. Jenkins and K. Kawamura, *Polymeric carbons: carbon fibre, glass and char*. Cambridge University Press, 1976.

[125] A. Dér *et al.*, "Modelling and analysis of the energy intensity in polyacrylonitrilie (PAN) precursor and carbon fibre manufacturing," *J. Clean. Prod.*, vol. 303, 2021, doi: 10.1016/j.jclepro.2021.127105.

[126] R. J. Diefendorf and E. Tokarsky, "High-performance carbon fibers," *Polym. Eng. Sci.*,

vol. 15, no. 3, pp. 150–159, 1975.

[127] E. Fitzer and D. J. Müller, “The influence of oxygen on the chemical reactions during stabilization of pan as carbon fiber precursor,” *Carbon N. Y.*, vol. 13, no. 1, pp. 63–69, 1975.

[128] A. Oberlin, “Carbonization and graphitization,” *Carbon N. Y.*, vol. 22, no. 6, pp. 521–541, 1984.

[129] D. D. Edie, “The effect of processing on the structure and properties of carbon fibers,” *Carbon N. Y.*, vol. 36, no. 4, pp. 345–362, 1998.

[130] A. Oberlin, M. Endo, and T. Koyama, “Filamentous growth of carbon through benzene decomposition,” *J. Cryst. Growth*, vol. 32, no. 3, pp. 335–349, Mar. 1976, doi: 10.1016/0022-0248(76)90115-9.

[131] J. Liu, X. Chen, D. Liang, and Q. Xie, “Development of pitch-based carbon fibers: A review,” *Energy Sources, Part A Recover. Util. Environ. Eff.*, pp. 1–21, 2020.

[132] R. A. Yuniar, W. Widiyastuti, H. Setyawan, H. Purwaningsih, S. Machmudah, and D. Anggoro, “Formation of carbon fibres from polymer poly (vinyl alcohol)/acetylene black using electrospinning method,” in *IOP Conference Series: Materials Science and Engineering*, 2019, vol. 543, no. 1, p. 12030.

[133] Y. Kim, T.-H. Le, S. Kim, G. Park, K. S. Yang, and H. Yoon, “Single-walled carbon nanotube-in-binary-polymer nanofiber structures and their use as carbon precursors for electrochemical applications,” *J. Phys. Chem. C*, vol. 122, no. 8, pp. 4189–4198, 2018.

[134] R. A. P. Jayawickramage and J. P. Ferraris, “High performance supercapacitors using lignin based electrospun carbon nanofiber electrodes in ionic liquid electrolytes,” *Nanotechnology*, vol. 30, no. 15, p. 155402, 2019.

[135] J. Y. Seok *et al.*, “Hierarchically porous carbon nanofibers with controllable porosity derived from iodinated polyvinyl alcohol for supercapacitors,” *Adv. Mater. Interfaces*,

vol. 7, no. 16, p. 2000513, 2020.

[136] W. Schutyser, ab T. Renders, S. Van den Bosch, S.-F. Koelewijn, G. T. Beckham, and B. F. Sels, "Chemicals from lignin: an interplay of lignocellulose fractionation, depolymerisation, and upgrading," *Chem. Soc. Rev.*, vol. 47, no. 3, pp. 852–908, 2018.

[137] X. Shi, X. Wang, B. Tang, Z. Dai, K. Chen, and J. Zhou, "Impact of lignin extraction methods on microstructure and mechanical properties of lignin-based carbon fibers," *J. Appl. Polym. Sci.*, vol. 135, no. 10, pp. 1–7, 2018, doi: 10.1002/app.45580.

[138] I. Dallmeyer, L. T. Lin, Y. Li, F. Ko, and J. F. Kadla, "Preparation and Characterization of Interconnected, Kraft Lignin-B ased Carbon Fibrous Materials by Electrospinning," *Macromol. Mater. Eng.*, vol. 299, no. 5, pp. 540–551, 2014.

[139] N.-Y. Teng, I. Dallmeyer, and J. F. Kadla, "Incorporation of multiwalled carbon nanotubes into electrospun softwood kraft lignin-based fibers," *J. Wood Chem. Technol.*, vol. 33, no. 4, pp. 299–316, 2013.

[140] S.-X. Wang, L. Yang, L. P. Stubbs, X. Li, and C. He, "Lignin-derived fused electrospun carbon fibrous mats as high performance anode materials for lithium ion batteries," *ACS Appl. Mater. Interfaces*, vol. 5, no. 23, pp. 12275–12282, 2013.

[141] D. Lei, X.-D. Li, M.-K. Seo, M.-S. Khil, H.-Y. Kim, and B.-S. Kim, "NiCo2O4 nanostructure-decorated PAN/lignin based carbon nanofiber electrodes with excellent cyclability for flexible hybrid supercapacitors," *Polymer (Guildf).*, vol. 132, pp. 31–40, 2017.

[142] L. Deng, R. J. Young, I. A. Kinloch, Y. Zhu, and S. J. Eichhorn, "Carbon nanofibres produced from electrospun cellulose nanofibres," *Carbon N. Y.*, vol. 58, no. 0, pp. 66–75, 2013, doi: 10.1016/j.carbon.2013.02.032.

[143] V. Kuzmenko, O. Naboka, P. Gatenholm, and P. Enoksson, "Ammonium chloride promoted synthesis of carbon nanofibers from electrospun cellulose acetate," *Carbon N.*

Y., vol. 67, pp. 694–703, 2014.

[144] N. Byrne, A. Leblais, and B. Fox, "Preparation of polyacrylonitrile–natural polymer composite precursors for carbon fiber using ionic liquid co solvent solutions," *J. Mater. Chem. A*, vol. 2, no. 10, pp. 3424–3429, 2014.

[145] W. Luo *et al.*, "Carbon nanofibers derived from cellulose nanofibers as a long-life anode material for rechargeable sodium-ion batteries," *J. Mater. Chem. A*, vol. 1, no. 36, pp. 10662–10666, 2013.

[146] J. Cai *et al.*, "High-performance supercapacitor electrode from cellulose-derived, inter-bonded carbon nanofibers," *J. Power Sources*, vol. 324, pp. 302–308, Aug. 2016, doi: 10.1016/j.jpowsour.2016.05.070.

[147] B. K. Roy, I. Tahmid, and T. U. Rashid, "Chitosan-based materials for supercapacitor applications: A review," *J. Mater. Chem. A*, vol. 9, no. 33, pp. 17592–17642, 2021, doi: 10.1039/d1ta02997e.

[148] T. A. M. Valente, D. M. Silva, P. S. Gomes, M. H. Fernandes, J. D. Santos, and V. Sencadas, "Effect of sterilization methods on electrospun poly(lactic acid) (PLA) fiber alignment for biomedical applications," *ACS Appl. Mater. Interfaces*, vol. 8, no. 5, pp. 3241–3249, 2016, doi: 10.1021/acsami.5b10869.

[149] M. P. Arrieta, J. López, D. López, J. M. Kenny, and L. Peponi, "Development of flexible materials based on plasticized electrospun PLA-PHB blends: Structural, thermal, mechanical and disintegration properties," *Eur. Polym. J.*, vol. 73, pp. 433–446, 2015, doi: 10.1016/j.eurpolymj.2015.10.036.

[150] C. Gonçalves, I. C. Gonçalves, F. D. Magalhães, and A. M. Pinto, "Poly(lactic acid) composites containing carbon-based nanomaterials: A review," *Polymers (Basel).*, vol. 9, no. 7, pp. 1–37, 2017, doi: 10.3390/polym9070269.

[151] M. Jamshidian, E. A. Tehrany, M. Imran, M. Jacquot, and S. Desobry, "Poly-lactic acid:

production, applications, nanocomposites, and release studies," *Compr. Rev. food Sci. food Saf.*, vol. 9, no. 5, pp. 552–571, 2010.

[152] L. Ji and X. Zhang, "Fabrication of porous carbon nanofibers and their application as anode materials for rechargeable lithium-ion batteries," *Nanotechnology*, vol. 20, no. 15, p. 155705, 2009.

[153] F. Carrasco, P. Pagès, J. Gámez-Pérez, O. O. Santana, and M. L. Maspoch, "Processing of poly (lactic acid): Characterization of chemical structure, thermal stability and mechanical properties," *Polym. Degrad. Stab.*, vol. 95, no. 2, pp. 116–125, 2010.

[154] R. Jayakumar, M. Prabaharan, P. T. S. Kumar, S. V Nair, and H. Tamura, "Biomaterials based on chitin and chitosan in wound dressing applications," *Biotechnol. Adv.*, vol. 29, no. 3, pp. 322–337, 2011.

[155] I.-Y. Kim *et al.*, "Chitosan and its derivatives for tissue engineering applications," *Biotechnol. Adv.*, vol. 26, no. 1, pp. 1–21, 2008.

[156] C. Radhakumary, P. D. Nair, S. Mathew, and C. P. R. Nair, "HEMA-grafted chitosan for dialysis membrane applications," *J. Appl. Polym. Sci.*, vol. 101, no. 5, pp. 2960–2966, 2006.

[157] C. A. Pinto, K. K. Saripella, N. C. Loka, and S. H. Neau, "Development and characterization of chitosan cross-linked with tripolyphosphate as a sustained release agent in tablets, Part I: design of experiments and optimization," *J. Pharm. Sci.*, vol. 107, no. 4, pp. 1063–1075, 2018.

[158] L. Orzali, B. Corsi, C. Forni, and L. Riccioni, "Chitosan in agriculture: a new challenge for managing plant disease," *Biol. Act. Appl. Mar. polysaccharides*, pp. 87–96, 2017.

[159] K. Y. Lee, L. Jeong, Y. O. Kang, S. J. Lee, and W. H. Park, "Electrospinning of polysaccharides for regenerative medicine," *Adv. Drug Deliv. Rev.*, vol. 61, no. 12, pp. 1020–1032, 2009.

[160] K. Chen, J. Liu, H. Bian, W. Wang, F. Wang, and Z. Shao, "Dexterous and friendly preparation of N/P co-doping hierarchical porous carbon nanofibers via electrospun chitosan for high performance supercapacitors," *J. Electroanal. Chem.*, vol. 878, p. 114473, 2020.

[161] S. Ahmed, A. Ahmed, and M. Rafat, "Performance of chitosan derived activated carbon in supercapacitor," *Adv. Nat. Sci. Nanosci. Nanotechnol.*, vol. 10, no. 2, p. 25003, 2019.

[162] B. K. Roy, I. Tahmid, and T. U. Rashid, "Chitosan-based materials for supercapacitor applications: a review," *J. Mater. Chem. A*, vol. 9, no. 33, pp. 17592–17642, 2021.

[163] Z. Lin, X. Xiang, S. Peng, X. Jiang, and L. Hou, "Facile synthesis of chitosan-based carbon with rich porous structure for supercapacitor with enhanced electrochemical performance," *J. Electroanal. Chem.*, vol. 823, pp. 563–572, 2018.

[164] K. Pandiselvi and S. Thambidurai, "Chitosan-ZnO/polyaniline ternary nanocomposite for high-performance supercapacitor," *Ionics (Kiel).*, vol. 20, pp. 551–561, 2014.

[165] G. Sun, B. Li, J. Ran, X. Shen, and H. Tong, "Three-dimensional hierarchical porous carbon/graphene composites derived from graphene oxide-chitosan hydrogels for high performance supercapacitors," *Electrochim. Acta*, vol. 171, pp. 13–22, 2015.

[166] M. Gao *et al.*, "Sandwich construction of chitosan/reduced graphene oxide composite as additive-free electrode material for high-performance supercapacitors," *Carbohydr. Polym.*, vol. 255, p. 117397, 2021.

[167] M. Karpuraranjith and S. Thambidurai, "Twist fibrous structure of CS–SnO 2–PANI ternary hybrid composite for electrochemical capacitance performance," *RSC Adv.*, vol. 6, no. 46, pp. 40567–40576, 2016.

[168] J. Huang *et al.*, "Ultrahigh-surface-area hierarchical porous carbon from chitosan: acetic acid mediated efficient synthesis and its application in superior supercapacitors," *J. Mater. Chem. A*, vol. 5, no. 47, pp. 24775–24781, 2017.

[169] K. Katayama, K. Nakamura, and T. Amano, "Structural formation during melt spinning process," *Kolloid-Zeitschrift und Zeitschrift für Polym.*, vol. 226, no. 2, pp. 125–134, 1968.

[170] D. M. Phillips *et al.*, "Regenerated silk fiber wet spinning from an ionic liquid solution," *J. Mater. Chem.*, vol. 15, no. 39, pp. 4206–4208, 2005.

[171] T. Nakajima, K. Kajiwara, and J. E. McIntyre, *Advanced fiber spinning technology*. Woodhead Publishing, 1994.

[172] V. B. Gupta and V. K. Kothari, *Manufactured fibre technology*. Springer Science & Business Media, 2012.

[173] W. S. Mohamed, "Applications of nanotechnology in the polymer and textile fields," 2009.

[174] H. Khayyam *et al.*, "PAN precursor fabrication, applications and thermal stabilization process in carbon fiber production: Experimental and mathematical modelling," *Prog. Mater. Sci.*, vol. 107, p. 100575, 2020.

[175] A. Formhals, "Process and apparatus for preparing artificial threads US Patent Specification, 1975504," 1934.

[176] D. H. Reneker and I. Chun, "Nanometre diameter fibres of polymer, produced by electrospinning," *Nanotechnology*, vol. 7, no. 3, p. 216, 1996.

[177] S. Agarwal, J. H. Wendorff, and A. Greiner, "Use of electrospinning technique for biomedical applications," *Polymer (Guildf).*, vol. 49, no. 26, pp. 5603–5621, 2008.

[178] D. Li and Y. Xia, "Direct fabrication of composite and ceramic hollow nanofibers by electrospinning," *Nano Lett.*, vol. 4, no. 5, pp. 933–938, 2004.

[179] J. Xie and C.-H. Wang, "Electrospun micro-and nanofibers for sustained delivery of paclitaxel to treat C6 glioma in vitro," *Pharm. Res.*, vol. 23, pp. 1817–1826, 2006.

[180] Y. Z. Zhang, Y. Feng, Z. M. Huang, S. Ramakrishna, and C. T. Lim, "Fabrication of porous electrospun nanofibres," *Nanotechnology*, vol. 17, no. 3, p. 901, 2006.

[181] T. J. Sill and H. A. Von Recum, "Electrospinning: applications in drug delivery and tissue engineering," *Biomaterials*, vol. 29, no. 13, pp. 1989–2006, 2008.

[182] L. Persano, A. Camposeo, C. Tekmen, and D. Pisignano, "Industrial upscaling of electrospinning and applications of polymer nanofibers: a review," *Macromol. Mater. Eng.*, vol. 298, no. 5, pp. 504–520, 2013.

[183] Y. Yang *et al.*, "Effect of electric field distribution uniformity on electrospinning," *J. Appl. Phys.*, vol. 103, no. 10, 2008.

[184] B. Zaarour, L. Zhu, and X. Jin, "A review on the secondary surface morphology of electrospun nanofibers: formation mechanisms, characterizations, and applications," *ChemistrySelect*, vol. 5, no. 4, pp. 1335–1348, 2020.

[185] E. R. Kenawy *et al.*, "Electrospinning of poly(ethylene-co-vinyl alcohol) fibers," *Biomaterials*, 2003, doi: 10.1016/S0142-9612(02)00422-2.

[186] H. Fong, I. Chun, and D. H. Reneker, "Beaded nanofibers formed during electrospinning," in *Polymer*, Jul. 1999, vol. 40, no. 16, pp. 4585–4592, doi: 10.1016/S0032-3861(99)00068-3.

[187] B. Veleirinho, M. F. Rei, and J. A. Lopes-DA-Silva, "Solvent and concentration effects on the properties of electrospun poly (ethylene terephthalate) nanofiber mats," *J. Polym. Sci. Part B Polym. Phys.*, vol. 46, no. 5, pp. 460–471, 2008.

[188] M. S. Khil, H. Y. Kim, M. S. Kim, S. Y. Park, and D.-R. Lee, "Nanofibrous mats of poly(trimethylene terephthalate) via electrospinning," *Polymer (Guildf).*, vol. 45, no. 1, pp. 295–301, Jan. 2004, doi: 10.1016/J.POLYMER.2003.09.049.

[189] Z. M. Huang, Y. Z. Zhang, M. Kotaki, and S. Ramakrishna, "A review on polymer nanofibers by electrospinning and their applications in nanocomposites," *Compos. Sci.*

Technol., vol. 63, no. 15, pp. 2223–2253, 2003, doi: 10.1016/S0266-3538(03)00178-7.

[190] J. Kameoka *et al.*, "A scanning tip electrospinning source for deposition of oriented nanofibres," *Nanotechnology*, vol. 14, no. 10, pp. 1124–1129, 2003, doi: 10.1088/0957-4484/14/10/310.

[191] C. Mit-Uppatham, M. Nithitanakul, and P. Supaphol, "Ultrafine electrospun polyamide-6 fibers: Effect of solution conditions on morphology and average fiber diameter," *Macromol. Chem. Phys.*, vol. 205, no. 17, pp. 2327–2338, 2004, doi: 10.1002/macp.200400225.

[192] D. Li, Y. Wang, and Y. Xia, "Electrospinning Nanofibers as Uniaxially Aligned Arrays and Layer-by-Layer Stacked Films," *Adv. Mater.*, vol. 16, no. 4, pp. 361–366, 2004, doi: 10.1002/adma.200306226.

[193] J. Ahne, Q. Li, E. Croiset, and Z. Tan, "Electrospun cellulose acetate nanofibers for airborne nanoparticle filtration," *Text. Res. J.*, vol. 89, no. 15, pp. 3137–3149, Aug. 2019, doi: 10.1177/0040517518807440.

[194] S. Chattopadhyay, T. A. Hatton, and G. C. Rutledge, "Aerosol filtration using electrospun cellulose acetate fibers," *J. Mater. Sci.*, vol. 51, no. 1, pp. 204–217, 2015, doi: 10.1007/s10853-015-9286-4.

[195] S. K. Tiwari and S. S. Venkatraman, "Importance of viscosity parameters in electrospinning: Of monolithic and core-shell fibers," *Mater. Sci. Eng. C*, vol. 32, no. 5, pp. 1037–1042, Jul. 2012, doi: 10.1016/j.msec.2012.02.019.

[196] P. Gupta, C. Elkins, T. E. Long, and G. L. Wilkes, "Electrospinning of linear homopolymers of poly(methyl methacrylate): Exploring relationships between fiber formation, viscosity, molecular weight and concentration in a good solvent," *Polymer (Guildf).*, 2005, doi: 10.1016/j.polymer.2005.04.021.

[197] E. Alginate, N. Response, and S. Analysis, "Effect of Solution Composition Variables

on Electrospun Alginate Nanofibers: Response Surface Analysis," *Polymers (Basel).*, vol. 11, no. 4, p. 692, 2019.

[198] J. H. Yu, S. V. Fridrikh, and G. C. Rutledge, "The role of elasticity in the formation of electrospun fibers," *Polymer (Guildf).*, vol. 47, no. 13, pp. 4789–4797, Jun. 2006, doi: 10.1016/j.polymer.2006.04.050.

[199] R. Rošic, J. Pelipenko, P. Kocbek, S. Baumgartner, M. Bešter-Rogač, and J. Kristl, "The role of rheology of polymer solutions in predicting nanofiber formation by electrospinning," *Eur. Polym. J.*, 2012, doi: 10.1016/j.eurpolymj.2012.05.001.

[200] A. S. M. Wittmar, M. Ropertz, M. Braun, U. Hagemann, C. Andronescu, and M. Ulbricht, "Preparation of N-doped carbon materials from cellulose: chitosan blends and their potential application in electrocatalytic oxygen reduction," *Polym. Bull.*, vol. 80, no. 7, pp. 7827–7845, 2023.

[201] C. Blanco, S. Lu, S. P. Appleyard, and B. Rand, "The stabilisation of carbon fibres studied by micro-thermal analysis," *Carbon N. Y.*, vol. 41, no. 1, pp. 165–171, 2003, doi: 10.1016/S0008-6223(02)00277-4.

[202] K. Miijra, H. Nakagawa, and K. Hashimoto, "Examination of the oxidative stabilization reaction of the pitch-based carbon fiber through continuous measurement of oxygen chemisorption and gas formation rate," *Fuel Energy Abstr.*, vol. 36, no. 6, p. 423, 1995, doi: 10.1016/0140-6701(95)97586-9.

[203] I. Brodin, M. Ernstsson, G. Gellerstedt, and E. Sjöholm, "Oxidative stabilisation of kraft lignin for carbon fibre production," 2012.

[204] S. M. Aldosari, M. Khan, and S. Rahatekar, "Manufacturing carbon fibres from pitch and polyethylene blend precursors: a review," *J. Mater. Res. Technol.*, vol. 9, no. 4, pp. 7786–7806, 2020.

[205] K. Morita, Y. Murata, A. Ishitani, K. Murayama, T. Ono, and A. Nakajima,

"Characterization of commercially available PAN (polyacrylonitri1e)-based carbon fibers," *Pure Appl. Chem.*, vol. 58, no. 3, pp. 455–468, 1986.

[206] T. Takahagi, I. Shimada, M. Fukuhara, K. Morita, and A. Ishitani, "XPS studies on the chemical structure of the stabilized polyacrylonitrile fiber in the carbon fiber production process," *J. Polym. Sci. Part A Polym. Chem.*, vol. 24, no. 11, pp. 3101–3107, 1986.

[207] Z. Bashir, "A critical review of the stabilisation of polyacrylonitrile," *Carbon N. Y.*, vol. 29, no. 8, pp. 1081–1090, 1991.

[208] N. Byrne, R. De Silva, Y. Ma, H. Sixta, and M. Hummel, "Enhanced stabilization of cellulose-lignin hybrid filaments for carbon fiber production," *Cellulose*, vol. 25, no. 1, pp. 723–733, 2018, doi: 10.1007/s10570-017-1579-0.

[209] R. Shokrani Havigh and H. Mahmoudi Chenari, "A comprehensive study on the effect of carbonization temperature on the physical and chemical properties of carbon fibers," *Sci. Rep.*, vol. 12, no. 1, p. 10704, 2022.

[210] R. C. Bansal and J. B. Donnet, "16 - Pyrolytic Formation of High-performance Carbon Fibres," G. Allen and J. C. B. T.-C. P. S. and S. Bevington, Eds. Amsterdam: Pergamon, 1989, pp. 501–520.

[211] L. Tao *et al.*, "Flexible anode materials for lithium-ion batteries derived from waste biomass-based carbon nanofibers: I. Effect of carbonization temperature," *RSC Adv.*, vol. 8, no. 13, pp. 7102–7109, 2018.

[212] H.-M. Lee, K.-H. An, and B.-J. Kim, "Effects of carbonization temperature on pore development in polyacrylonitrile-based activated carbon nanofibers," *Carbon Lett.*, vol. 15, no. 2, pp. 146–150, 2014.

[213] B. M. Thamer, A. Aldalbahi, M. Moydeen A, A. M. Al-Enizi, H. El-Hamshary, and M. H. El-Newehy, "Fabrication of functionalized electrospun carbon nanofibers for enhancing lead-ion adsorption from aqueous solutions," *Sci. Rep.*, vol. 9, no. 1, p. 19467,

2019.

[214] M.-A. Kim *et al.*, "Strengthened PAN-based carbon fibers obtained by slow heating rate carbonization," *Sci. Rep.*, vol. 6, no. 1, p. 22988, 2016.

[215] H. H. Kuo, J. H. C. Lin, and C. P. Ju, "Effect of carbonization rate on the properties of a PAN/phenolic-based carbon/carbon composite," *Carbon N. Y.*, vol. 43, no. 2, pp. 229–239, 2005, doi: 10.1016/j.carbon.2004.08.024.

[216] W. Xie, H.-F. Cheng, Z.-Y. Chu, and Z.-H. Chen, "Effect of carbonization time on the structure and electromagnetic parameters of porous-hollow carbon fibres," *Ceram. Int.*, vol. 35, no. 7, pp. 2705–2710, 2009.

[217] M. K. Jha *et al.*, "Surface modified activated carbons: Sustainable bio-based materials for environmental remediation," *Nanomaterials*, vol. 11, no. 11, p. 3140, 2021.

[218] F. Rodriguez-Reinoso, M. Molina-Sabio, and M. T. González, "The use of steam and CO2 as activating agents in the preparation of activated carbons," *Carbon N. Y.*, vol. 33, no. 1, pp. 15–23, 1995.

[219] J. Alcaniz-Monge, D. Cazorla-Amorós, A. Linares-Solano, S. Yoshida, and A. Oya, "Effect of the activating gas on tensile strength and pore structure of pitch-based carbon fibres," *Carbon N. Y.*, vol. 32, no. 7, pp. 1277–1283, 1994.

[220] J. Alcaniz-Monge, M. Perez-Cadenas, and J. P. Marco-Lozar, "Removal of harmful volatile organic compounds on activated carbon fibres prepared by steam or carbon dioxide activation," *Adsorpt. Sci. Technol.*, vol. 30, no. 6, pp. 473–482, 2012.

[221] S. Mopoung and P. Amornsakchai, "Microporous Activated Carbon Fiber from Pineapple Leaf Fiber by H3PO4 Activation," *Asian J. Sci. Res.*, vol. 9, no. 1, p. 24, 2016.

[222] J. A. Maciá-Agulló, B. C. Moore, D. Cazorla-Amorós, and A. Linares-Solano, "Influence of carbon fibres crystallinities on their chemical activation by KOH and NaOH," *Microporous Mesoporous Mater.*, vol. 101, no. 3, pp. 397–405, 2007.

[223] J. Liu *et al.*, "ZnCl2 activated electrospun carbon nanofiber for capacitive desalination," *Desalination*, vol. 344, pp. 446–453, 2014, doi: 10.1016/j.desal.2014.04.015.

[224] X. Li *et al.*, "Effect of the oxygen functional groups of activated carbon on its electrochemical performance for supercapacitors," *New Carbon Mater.*, vol. 35, no. 3, pp. 232–243, 2020.

[225] E. B. Yutomo, F. A. Noor, and T. Winata, "Effect of the number of nitrogen dopants on the electronic and magnetic properties of graphitic and pyridinic N-doped graphene–a density-functional study," *RSC Adv.*, vol. 11, no. 30, pp. 18371–18380, 2021.

[226] L. Ou *et al.*, "Pseudocapacitance-dominated zinc storage enabled by nitrogen-doped carbon stabilized amorphous vanadyl phosphate," *Chem. Eng. J.*, vol. 426, p. 131868, 2021.

[227] D. Hulicova-Jurcakova *et al.*, "Effect of surface phosphorus functionalities of activated carbons containing oxygen and nitrogen on electrochemical capacitance," *Carbon N. Y.*, vol. 47, no. 6, pp. 1576–1584, 2009.

[228] V. Jiménez, P. Sánchez, J. L. Valverde, and A. Romero, "Influence of the activating agent and the inert gas (type and flow) used in an activation process for the porosity development of carbon nanofibers," *J. Colloid Interface Sci.*, vol. 336, no. 2, pp. 712–722, 2009, doi: 10.1016/j.jcis.2009.04.017.

[229] P. E. Hock, M. A. A. Zaini, and M. Abbas, "Activated carbons by zinc chloride activation for dye removal–a commentary," *Acta Chim. Slovaca*, vol. 11, no. 2, pp. 99–106, 2018.

[230] S. Yorgun, N. Vural, and H. Demiral, "Preparation of high-surface area activated carbons from Paulownia wood by ZnCl2 activation," *Microporous mesoporous Mater.*, vol. 122, no. 1–3, pp. 189–194, 2009.

[231] Y. Guo and D. A. Rockstraw, "Physicochemical properties of carbons prepared from

pecan shell by phosphoric acid activation," *Bioresour. Technol.*, vol. 98, no. 8, pp. 1513–1521, 2007.

[232] M. S. Solum, R. J. Pugmire, M. Jagtoyen, and F. Derbyshire, "Evolution of carbon structure in chemically activated wood," *Carbon N. Y.*, vol. 33, no. 9, pp. 1247–1254, 1995.

[233] Y. Li, X. Zhang, R. Yang, G. Li, and C. Hu, "The role of H3PO4 in the preparation of activated carbon from NaOH-treated rice husk residue," *RSC Adv.*, vol. 5, no. 41, pp. 32626–32636, 2015, doi: 10.1039/c5ra04634c.

[234] M. Zhi, S. Liu, Z. Hong, and N. Wu, "Electrospun activated carbon nanofibers for supercapacitor electrodes," *RSC Adv.*, vol. 4, no. 82, pp. 43619–43623, 2014, doi: 10.1039/c4ra05512h.

[235] N. Mohd, S. F. S. Draman, M. S. N. Salleh, and N. B. Yusof, "Dissolution of cellulose in ionic liquid: A review," in *AIP conference proceedings*, 2017, vol. 1809, no. 1.

[236] Y. Zhang, C. Zhang, and Y. Wang, "Recent progress in cellulose-based electrospun nanofibers as multifunctional materials," *Nanoscale Adv.*, vol. 3, no. 21, pp. 6040–6047, 2021.

[237] S. Tungprapa *et al.*, "Electrospun cellulose acetate fibers: Effect of solvent system on morphology and fiber diameter," *Cellulose*, vol. 14, no. 6, pp. 563–575, Dec. 2007, doi: 10.1007/s10570-007-9113-4.

[238] A. Hadjizadeh, H. Savoji, and A. Ajji, "A facile approach for the mass production of submicro/micro poly (lactic acid) fibrous mats and their cytotoxicity test towards neural stem cells," *Biomed Res. Int.*, vol. 2016, 2016.

[239] Y. Zhang, Z. Cheng, Z. Han, S. Zhao, X. Zhao, and L. Kang, "Stable multi-jet electrospinning with high throughput using the bead structure nozzle," *RSC Adv.*, vol. 8, no. 11, pp. 6069–6074, 2018.

[240] A. Bengtsson, J. Bengtsson, M. Sedin, and E. Sjöholm, "Carbon Fibers from Lignin-Cellulose Precursors: Effect of Stabilization Conditions," *ACS Sustain. Chem. Eng.*, vol. 7, no. 9, pp. 8440–8448, 2019, doi: 10.1021/acssuschemeng.9b00108.

[241] K. S. W. Sing, "Reporting physisorption data for gas/solid systems with special reference to the determination of surface area and porosity (Recommendations 1984)," *Pure Appl. Chem.*, vol. 57, no. 4, pp. 603–619, 1985.

[242] F. Stoeckli, M. V López-Ramón, D. Hugi-Cleary, and A. Guillot, "Micropore sizes in activated carbons determined from the Dubinin-Radushkevich equation," *Carbon N. Y.*, vol. 39, no. 7, pp. 1115–1116, 2001.

[243] K. Raymond, "XPS Peak Fitting Program for WIN95/98 XPSPEAK Ver. 4.1," *http//www. phy. cuhk. edu. hk/~ surface/XPSPEAK/*, 2000.

[244] V. Kandjou, M. Hernaez, B. Acevedo, and S. Melendi-Espina, "Interfacial crosslinked controlled thickness graphene oxide thin-films through dip-assisted layer-by-layer assembly means," *Prog. Org. Coatings*, vol. 137, no. September, p. 105345, 2019, doi: 10.1016/j.porgcoat.2019.105345.

[245] C. Wang, L. Sun, Y. Zhou, P. Wan, X. Zhang, and J. Qiu, "P/N co-doped microporous carbons from H3PO4-doped polyaniline by in situ activation for supercapacitors," *Carbon N. Y.*, vol. 59, pp. 537–546, 2013, doi: 10.1016/j.carbon.2013.03.052.

[246] F. Ganji, M. J. Abdekhodaie, and A. Ramazani SA, "Gelation time and degradation rate of chitosan-based injectable hydrogel," *J. sol-gel Sci. Technol.*, vol. 42, pp. 47–53, 2007.

[247] Z. Jun, H. Hou, A. Schaper, J. H. Wendorff, and A. Greiner, "Poly-L-lactide nanofibers by electrospinning - Influence of solution viscosity and electrical conductivity on fiber diameter and fiber morphology," *E-Polymers*, vol. 3, no. 1, pp. 1–9, 2003, doi: 10.1515/epoly.2003.3.1.102.

[248] X. Zong, K. Kim, D. Fang, S. Ran, B. S. Hsiao, and B. Chu, "Structure and process

relationship of electrospun bioabsorbable nanofiber membranes," *Polymer (Guildf).*, vol. 43, no. 16, pp. 4403–4412, 2002.

[249] X. Chen, Y. Zhang, X. He, H. Li, B. Wei, and W. Yang, "Electrospinning on a plucked string," *J. Mater. Sci.*, vol. 54, no. 1, pp. 901–910, 2019.

[250] K. Desai, K. Kit, J. Li, and S. Zivanovic, "Morphological and surface properties of electrospun chitosan nanofibers," *Biomacromolecules*, vol. 9, no. 3, pp. 1000–1006, 2008.

[251] A. Haider, S. Haider, and I. K. Kang, "A comprehensive review summarizing the effect of electrospinning parameters and potential applications of nanofibers in biomedical and biotechnology," *Arabian Journal of Chemistry*. 2018, doi: 10.1016/j.arabjc.2015.11.015.

[252] Z. Li and C. Wang, *One-dimensional nanostructures: electrospinning technique and unique nanofibers*. Springer, 2013.

[253] X. Y. Yuan, Y. Y. Zhang, C. Dong, and J. Sheng, "Morphology of ultrafine polysulfone fibers prepared by electrospinning," *Polym. Int.*, vol. 53, no. 11, pp. 1704–1710, 2004, doi: 10.1002/pi.1538.

[254] K. Rodríguez, P. Gatenholm, and S. Renneckar, "Electrospinning cellulosic nanofibers for biomedical applications: Structure and in vitro biocompatibility," *Cellulose*, vol. 19, no. 5, pp. 1583–1598, 2012, doi: 10.1007/s10570-012-9734-0.

[255] J. Macossay, A. Marruffo, R. Rincon, T. Eubanks, and A. Kuang, "Effect of needle diameter on nanofiber diameter and thermal properties of electrospun poly (methyl methacrylate)," *Polym. Adv. Technol.*, vol. 18, no. 3, pp. 180–183, 2007.

[256] I. Partheniadis, I. Nikolakakis, I. Laidmäe, and J. Heinämäki, "A mini-review: Needleless electrospinning of nanofibers for pharmaceutical and biomedical applications," *Processes*, vol. 8, no. 6, p. 673, 2020.

[257] N. Abidi, E. Hequet, and D. Ethridge, "Thermogravimetric analysis of cotton fibers:

relationships with maturity and fineness," *J. Appl. Polym. Sci.*, vol. 103, no. 6, pp. 3476–3482, 2007.

[258] J. Singh and P. K. Dutta, "Antibacterial and physiochemical behavior of prepared chitosan/pyridine-3, 5-di-carboxylic acid complex for biomedical applications," *J. Macromol. Sci. Part A*, vol. 48, no. 3, pp. 246–253, 2011.

[259] N. D. Le, M. Trogen, Y. Ma, R. J. Varley, M. Hummel, and N. Byrne, "Understanding the influence of key parameters on the stabilisation of cellulose-lignin composite fibres," *Cellulose*, vol. 28, no. 2, pp. 911–919, 2021, doi: 10.1007/s10570-020-03583-y.

[260] G. Dennis, W. Harrison, K. Agnes, and G. Erastus, "Effect of Biological Control Antagonists Adsorbed on Chitosan Immobilized Silica Nanocomposite on Ralstonia solanacearum and Growth of Tomato Seedlings," *Adv. Res.*, vol. 6, no. 3, pp. 1–23, 2016, doi: 10.9734/air/2016/22742.

[261] C. Lustriane, F. M. Dwivany, V. Suendo, and M. Reza, "Effect of chitosan and chitosan-nanoparticles on post harvest quality of banana fruits," *J. Plant Biotechnol.*, vol. 45, no. 1, pp. 36–44, 2018, doi: 10.5010/JPB.2018.45.1.036.

[262] A. Drabczyk *et al.*, "Physicochemical investigations of chitosan-based hydrogels containing Aloe vera designed for biomedical use," *Materials (Basel).*, vol. 13, no. 14, pp. 1–20, 2020, doi: 10.3390/ma13143073.

[263] M. Yanilmaz, E. Abdolrazzaghian, L. Chen, J. Kim, and J. J. Kim, "Centrifugally spun PVA/PVP based B, N, F doped carbon nanofiber electrodes for sodium ion batteries," *Polymers (Basel).*, vol. 14, no. 24, p. 5541, 2022.

[264] Z. Tang *et al.*, "Revealing the closed pore formation of waste wood-derived hard carbon for advanced sodium-ion battery," *Nat. Commun.*, vol. 14, no. 1, p. 6024, 2023.

[265] W. Wang, C. Xue, and X. Mao, "Chitosan: Structural modification, biological activity and application," *Int. J. Biol. Macromol.*, vol. 164, pp. 4532–4546, 2020.

[266] I. A. Udoetok, L. D. Wilson, and J. V Headley, "'pillaring effects' in cross-linked cellulose biopolymers: A study of structure and properties," *Int. J. Polym. Sci.*, vol. 2018, pp. 1–13, 2018.

[267] W. K. Son, J. H. Youk, T. S. Lee, and W. H. Park, "Electrospinning of ultrafine cellulose acetate fibers: studies of a new solvent system and deacetylation of ultrafine cellulose acetate fibers," *J. Polym. Sci. Part B Polym. Phys.*, vol. 42, no. 1, pp. 5–11, 2004.

[268] D. Prabhaharan, H. Park, O. Choi, A. Abraham, and B.-I. Sang, "Enhancing cellulose acetate biodegradability in cigarette filters: an in-depth analysis of thermal alkaline pretreatment, microbial dynamics, and breakdown pathway prediction," *Microb. Cell Fact.*, vol. 23, no. 1, p. 199, 2024.

[269] S. Yu *et al.*, "Sustainable hierarchical porous biomass carbons enriched with pyridinic and pyrrolic nitrogen for asymmetric supercapacitor," *Mater. Des.*, vol. 149, pp. 184–193, 2018.

[270] J. R. Pels, F. L. Kapteijn, J. A. Moulijn, Q. Zhu, and K. M. Thomas, "Evolution of nitrogen functionalities in carbonaceous materials during pyrolysis," *Carbon N. Y.*, vol. 33, no. 11, pp. 1641–1653, 1995.

[271] M. A. Atieh, O. Y. Bakather, B. Al-Tawbini, A. A. Bukhari, F. A. Abuilaiwi, and M. B. Fettouhi, "Effect of carboxylic functional group functionalized on carbon nanotubes surface on the removal of lead from water," *Bioinorg. Chem. Appl.*, vol. 2010, no. 1, p. 603978, 2010.

[272] Y. Yuan *et al.*, "Recent advances in understanding the effects of lignin structural characteristics on enzymatic hydrolysis," *Biotechnol. Biofuels*, vol. 14, pp. 1–20, 2021.

[273] H. Cao, X. Peng, M. Zhao, P. Liu, B. Xu, and J. Guo, "Oxygen functional groups improve the energy storage performances of graphene electrochemical supercapacitors," *RSC Adv.*, vol. 8, no. 6, pp. 2858–2865, 2018, doi: 10.1039/c7ra12425b.

[274] J. H. Kim *et al.*, "Impact of the oxygen functional group of nitric acid-treated activated carbon on KOH activation reaction," *Carbon Lett.*, vol. 29, no. 3, pp. 281–287, 2019, doi: 10.1007/s42823-019-00024-0.

[275] Y. Luo, D. Li, Y. Chen, X. Sun, Q. Cao, and X. Liu, "The performance of phosphoric acid in the preparation of activated carbon-containing phosphorus species from rice husk residue," *J. Mater. Sci.*, vol. 54, no. 6, pp. 5008–5021, 2019.

[276] W. Xu *et al.*, "Effect of Activation Temperature on Properties of H3PO4-Activated Carbon.," *BioResources*, vol. 16, no. 2, 2021.

[277] A. Ahmadpour and D. D. Do, "The preparation of activated carbon from macadamia nutshell by chemical activation," *Carbon N. Y.*, vol. 35, no. 12, pp. 1723–1732, 1997.

[278] T. E. Rufford, D. Hulicova-Jurcakova, K. Khosla, Z. Zhu, and G. Q. Lu, "Microstructure and electrochemical double-layer capacitance of carbon electrodes prepared by zinc chloride activation of sugar cane bagasse," *J. Power Sources*, vol. 195, no. 3, pp. 912–918, 2010.

[279] X. Xiang *et al.*, "Preparation of activated carbon from polyaniline by zinc chloride activation as supercapacitor electrodes," *J. Solid State Electrochem.*, vol. 15, pp. 2667–2674, 2011.

[280] Z. Zhou *et al.*, "Highly active N, O-doped hierarchical porous carbons for high-energy supercapacitors," *Chinese Chem. Lett.*, vol. 31, no. 5, pp. 1226–1230, 2020.

[281] L. Li and L. I. Feng, "The effect of carbonyl, carboxyl and hydroxyl groups on the capacitance of carbon nanotubes," *New Carbon Mater.*, vol. 26, no. 3, pp. 224–228, 2011.

[282] G. Sun *et al.*, "A capacity recoverable zinc-ion micro-supercapacitor," *Energy Environ. Sci.*, vol. 11, no. 12, pp. 3367–3374, 2018, doi: 10.1039/c8ee02567c.

[283] Y. Fang, Q. Zhang, and L. Cui, "Recent progress of mesoporous materials for high

performance supercapacitors," *Microporous Mesoporous Mater.*, vol. 314, p. 110870, 2021.

[284] Y. He *et al.*, "Capacitive mechanism of oxygen functional groups on carbon surface in supercapacitors," *Electrochim. Acta*, vol. 282, pp. 618–625, 2018, doi: 10.1016/j.electacta.2018.06.103.

[285] L. Wang *et al.*, "Coupling of EDLC and the reversible redox reaction: oxygen functionalized porous carbon nanosheets for zinc-ion hybrid supercapacitors," *J. Mater. Chem. A*, vol. 9, no. 27, pp. 15404–15414, 2021.

[286] Y. Yang, Y. Xiao, X. Nie, M. Yao, H. Liang, and D. Yuan, "Carbon materials in current zinc ion energy storage devices towards sustainability," *Carbon Res.*, vol. 3, no. 1, p. 62, 2024.

[287] X. Fan, Y. Lu, H. Xu, X. Kong, and J. Wang, "Reversible redox reaction on the oxygen-containing functional groups of an electrochemically modified graphite electrode for the pseudo-capacitance," *J. Mater. Chem.*, vol. 21, no. 46, pp. 18753–18760, 2011.

[288] J.-H. Lin, T.-H. Ko, Y.-H. Lin, and C.-K. Pan, "Various treated conditions to prepare porous activated carbon fiber for application in supercapacitor electrodes," *Energy & fuels*, vol. 23, no. 9, pp. 4668–4677, 2009.

[289] Y. Xie, "Electrochemical and hydrothermal activation of carbon fiber supercapacitor electrode," *Fibers Polym.*, vol. 23, no. 1, pp. 10–17, 2022.

[290] Q. Guo *et al.*, "Supercapacitors based on hybrid carbon nanofibers containing multiwalled carbon nanotubes," *J. Mater. Chem.*, vol. 19, no. 18, pp. 2810–2816, 2009.

[291] Y. Altin and A. Celik Bedeloglu, "Flexible carbon nanofiber yarn electrodes for self-standing fiber supercapacitors," *J. Ind. Text.*, vol. 51, no. 3_suppl, pp. 4254S-4267S, 2022.

[292] C. Liu *et al.*, "Preparation and electrochemical studies of electrospun phosphorus doped

porous carbon nanofibers," *RSC Adv.*, vol. 9, no. 12, pp. 6898–6906, 2019.

[293] W. Na, J. Jun, J. W. Park, G. Lee, and J. Jang, "Highly porous carbon nanofibers co-doped with fluorine and nitrogen for outstanding supercapacitor performance," *J. Mater. Chem. A*, vol. 5, no. 33, pp. 17379–17387, 2017.

[294] C. Kim, "Electrochemical characterization of electrospun activated carbon nanofibres as an electrode in supercapacitors," *J. Power Sources*, vol. 142, no. 1–2, pp. 382–388, 2005.

[295] M. D. Stoller, S. Park, Y. Zhu, J. An, and R. S. Ruoff, "Graphene-based ultracapacitors," *Nano Lett.*, vol. 8, no. 10, pp. 3498–3502, 2008.

[296] M. Jafari and G. G. Botte, "Sustainable Green Route for Activated Carbon Synthesis from Biomass Waste for High-Performance Supercapacitors," *ACS omega*, vol. 9, no. 11, pp. 13134–13147, 2024.

[297] A. B. Fuertes, G. A. Ferrero, N. Diez, and M. Sevilla, "A green route to high-surface area carbons by chemical activation of biomass-based products with sodium thiosulfate," *ACS Sustain. Chem. Eng.*, vol. 6, no. 12, pp. 16323–16331, 2018.

Appendix

Table A.1. Summary of diameter and morphology of electrospun nanofibres depending on different experimental parameters

	Concentration (w/v%)	Flow rate (mL/h)	Needle size (mm)	Mean diameter (nm)	Morphology
CA	11	0.5	0.622	-	Beads
			0.933	-	Beads
			1.25	-	Beads
		1	0.622	-	Beads
			0.933	-	Beads
			1.25	-	Beads
		2	0.622	-	Beads
			0.933	-	Beads
			1.25	-	Beads
	14	0.5	0.622	211 ± 33	Beaded fibres
			0.933	217 ± 48	Beaded fibres
			1.25	228 ± 49	Beaded fibres
		1	0.622	247 ± 43	Beaded fibres
			0.933	246 ± 50	Beaded fibres
			1.25	252 ± 52	Beaded fibres
		2	0.622	318 ± 71	Beaded fibres
			0.933	312 ± 79	Beaded fibres
			1.25	309 ± 80	Beaded fibres
	17	0.5	0.622	300 ± 69	Smooth fibres
			0.933	302 ± 75	Smooth fibres
			1.25	342 ± 73	Smooth fibres
		1	0.622	321 ± 74	Smooth fibres
			0.933	332 ± 78	Smooth fibres
			1.25	364 ± 98	Smooth fibres
		2	0.622	373 ± 87	Smooth fibres
			0.933	384 ± 91	Smooth fibres
			1.25	423 ± 100	Smooth fibres
	20	0.5	0.622	618 ± 122	Smooth fibres
			0.933	631 ± 103	Smooth fibres
			1.25	608 ± 115	Smooth fibres
		1	0.622	625 ± 134	Smooth fibres
			0.933	647 ± 133	Smooth fibres
			1.25	646 ± 134	Smooth fibres
		2	0.622	658 ± 146	Smooth fibres
			0.933	676 ± 157	Smooth fibres
			1.25	678 ± 137	Smooth fibres
PLA	6	0.5	0.622	-	Beads
			0.933	-	Beads
			1.25	-	Beads
		1	0.622	-	Beads
			0.933	-	Beads
			1.25	-	Beads
		2	0.622	-	Beads

	Concentration (w/v%)	Flow rate (mL/h)	Needle size (mm)	Mean diameter (nm)	Morphology
			0.933	-	Beads
			1.25	-	Beads
	8	0.5	0.622	-	Beads
			0.933	-	Beads
			1.25	-	Beads
		1	0.622	-	Beads
			0.933	-	Beads
			1.25	-	Beads
		2	0.622	-	Beads
			0.933	-	Beads
			1.25	-	Beads
	11	0.5	0.622	280 ± 33	Smooth fibres
			0.933	267 ± 39	Smooth fibres
			1.25	286 ± 43	Smooth fibres
		1	0.622	312 ± 41	Smooth fibres
			0.933	322 ± 49	Smooth fibres
			1.25	309 ± 53	Smooth fibres
		2	0.622	332 ± 52	Smooth fibres
			0.933	348 ± 68	Smooth fibres
			1.25	367 ± 72	Smooth fibres
	14	0.5	0.622	301 ± 37	Smooth fibres
			0.933	307 ± 43	Smooth fibres
			1.25	357 ± 64	Smooth fibres
		1	0.622	431 ± 46	Smooth fibres
			0.933	478 ± 67	Smooth fibres
			1.25	476 ± 68	Smooth fibres
		2	0.622	598 ± 92	Smooth fibres
			0.933	587 ± 112	Smooth fibres
			1.25	579 ± 102	Smooth fibres
CTS	3	0.5	0.622	-	Droplets
			0.933	-	Droplets
			1.25	-	Droplets
		1	0.622	-	Droplets
			0.933	-	Droplets
			1.25	-	Droplets
		2	0.622	-	Droplets
			0.933	-	Droplets
			1.25	-	Droplets
	4	0.5	0.622	-	Beads
			0.933	-	Beads
			1.25	-	Beads
		1	0.622	-	Beads
			0.933	-	Beads
			1.25	-	Beads
		2	0.622	-	Beads
			0.933	-	Beads
			1.25	-	Beads
	6	0.5	0.622	148 ± 43	Beaded fibres
			0.933	149 ± 50	Beaded fibres
			1.25	142 ± 58	Beaded fibres
		1	0.622	157 ± 47	Beaded fibres

	Concentration (w/v%)	**Flow rate (mL/h)**	**Needle size (mm)**	**Mean diameter (nm)**	**Morphology**
			0.933	162 ± 52	Beaded fibres
			1.25	158 ± 62	Beaded fibres
		2	0.622	164 ± 54	Beaded fibres
			0.933	169 ± 82	Beaded fibres
			1.25	169 ± 66	Beaded fibres
	8	0.5	0.622	302 ± 76	Smooth fibres
			0.933	300 ± 85	Smooth fibres
			1.25	312 ± 101	Smooth fibres
		1	0.622	351 ± 93	Smooth fibres
			0.933	353 ± 107	Smooth fibres
			1.25	360 ± 124	Smooth fibres
		2	0.622	427 ± 98	Smooth fibres
			0.933	414 ± 124	Smooth fibres
			1.25	459 ± 129	Smooth fibres